QSOs and galaxies: lensing, clustering and redshift-space distortions

Mountrichas, Georgios

QSOs and Galaxies: Lensing, Clustering and Redshift-Space Distortions.

Georgios Mountrichas

A thesis submitted to Durham University
in accordance with the regulations for admission to the
Degree of
Doctor of Philosophy.

Department of Physics
University of Durham

January 2008

This thesis is dedicated to my family

QSOs and Galaxies: Lensing, Clustering and Redshift-Space Distortions.

Georgios Mountrichas

Submitted for the degree of Doctor of Philosophy

Abstract

The aim of this thesis is to analyze statistically the available QSO, LRG, galaxy and cluster samples in order to estimate the QSO-galaxy lensing anti-correlation signal and measure the mass of foreground galaxies and clusters and to estimate the QSO-LRG clustering amplitude, the QSO bias and their dependence on QSO luminosity. We also investigate the behaviour of the group-galaxy infall parameter and their rms velocity dispersions for different group memberships. The aim here is to make dynamical estimates of the group masses to check the QSO lensing results.

We first cross-correlate the SDSS photo-z, $g < 21$, $1.0 < z_p < 2.2$ QSOs with $g < 21$ galaxies and clusters in the same areas. The anti-correlation found is somewhat less than the results of Myers et al. based on 2QZ QSOs. But contamination of the QSOs by low redshift NELGs and QSOs can cause underestimation of the anticorrelation lensing signal. Correcting for such low redshift contamination at the levels indicated by our spectroscopic checks suggests that the effect is generally small for QSO cross-correlations with $g < 21$ galaxies but may be an issue for fainter galaxy samples. Thus when this correction is applied to the photo-z QSO sample of Scranton et al. the anti-correlation increases and the agreement with the 2QZ results of Myers et al. is improved. When we also take into account the fainter $r < 21$ galaxy limit of Scranton et al. as opposed to $g < 21$ for Myers et al., the two observational results appear to be in very good agreement.

We then measure the bias of QSOs as a function of QSO luminosity at fixed redshift ($z < 1$) by cross-correlating them with Luminous Red Galaxies (LRGs) in the same spatial volume, hence breaking the degeneracy between QSO luminosity and redshift. We use three QSO samples from 2SLAQ, 2QZ and SDSS covering a

QSO absolute magnitude range $-24.5 < M_{b_j} < -21.5$, and cross-correlate them with 2SLAQ ($z \approx 0.5$) and AAOmega ($z \approx 0.7$) photometric and spectroscopic LRGs in the same redshift ranges. The 2-D and 3-D cross-clustering measurements are generally in good agreement. Our (2SLAQ) QSO-LRG clustering amplitude ($r_0 = 6.8^{+0.1}_{-0.3}\mathrm{h}^{-1}\mathrm{Mpc}$) as measured from the semi-projected cross-correlation function appears similar to the (2SLAQ) LRG-LRG auto-correlation amplitude ($r_0 = 7.45 \pm 0.35\mathrm{h}^{-1}\mathrm{Mpc}$) and both are higher than the (2QZ+2SLAQ) QSO-QSO amplitude ($r_0 \simeq 5.0\mathrm{h}^{-1}\mathrm{Mpc}$). Our measurements show remarkably little QSO-LRG cross-clustering dependence on QSO luminosity. Assuming a standard ΛCDM model and values for b_{LRG} measured from LRG autocorrelation analyses, we find $b_Q = 1.45 \pm 0.11$ at $M_{b_j} \approx -24$ and $b_Q = 1.90 \pm 0.16$ at $M_{b_j} \approx -22$.

We also find consistent results for the QSO bias from a $z-$space distortion analysis of the QSO-LRG cross-clustering at $z \approx 0.55$. The velocity dispersions fitted to QSO-LRG cross-correlation, $\xi(\sigma, \pi)$, at 680 kms^{-1} are intermediate between those for QSO-QSO and LRG-LRG clustering, as expected given the larger QSO redshift errors. The dynamical infall results give $\beta_Q = 0.55 \pm 0.10$, implying $b_Q = 1.4 \pm 0.2$. Thus both the $z-$space distortion and the amplitude analyses yield $b_Q \approx 1.5$ at $M_{bj} \approx -23$. The implied dark matter halo mass inhabited by QSOs at $z \approx 0.55$ is $\sim 10^{13} h^{-1} M_{\odot}$, again approximately independent of QSO luminosity.

Prompted by the indications from QSO lensing that there may be more mass associated with galaxy groups than expected from virial analyses, we make new dynamical infall estimates of the masses associated with 2PIGG groups and clusters. We analyse the redshift distortions in the cluster-galaxy cross-correlation function as a function of cluster membership, cross-correlating $z < 0.12$ 2PIGG clusters and groups with the full 2dF galaxy catalogue. We make estimates of the dynamical infall parameter, β, and new estimates of the group velocity dispersions for group membership classes out to $z < 0.12$. We first find that, out to 30-40$\mathrm{h}^{-1}\mathrm{Mpc}$, the amplitude of the full 3-D redshift space cross-correlation function, ξ_{cg}, rises monotonically with group membership.

We use a simple linear-theory infall model to fit $\xi(\sigma, \pi)$ in the range $5 < s < 40\mathrm{h}^{-1}\mathrm{Mpc}$. We find that the β versus membership relation for the data shows

a minimum at intermediate group membership $n \approx 20$ or $L \approx 2 \times 10^{11} h^{-2} L_{\odot}$, implying that the bias and hence M/L ratios rise by a significant factor ($\approx 5\times$) both for small groups and rich clusters. The minimum for the mocks is at a $2-3\times$ lower luminosity than for the data. However, the mocks also show a systematic shift between the location of the β minimum and the M/L minimum at $L \approx 10^{10} h^{-2} L_{\odot}$ given by direct calculation using the known DM distribution. Our overall conclusion is that bias estimates from dynamical infall appear to support the minimum in star-formation efficiency at intermediate halo masses. Nevertheless, there may still be significant systematic problems arising from measuring $\beta \propto \frac{1}{b} = \delta\rho_{mass}/\delta\rho_{galaxies}$ using large-scale infall rather than M/L using small-scale velocity dispersions.

Preface

The work described in this thesis was undertaken between October 2004 and December 2007 whilst the author was a research student under the supervision of Prof. Tom Shanks in the Department of Physics at the University of Durham. This work has not been submitted for any other degree at this (or any other) university.

Results from this thesis have appeared in the following papers:

Mountrichas, G., Shanks T., 2007, MNRAS, 380, 113M

Mountrichas, G., Shanks T., 2007, submitted to MNRAS, astro-ph/0712.3255

Mountrichas, G., Shanks T., Croom, S.M, Sawangwit, U., Schneider D. P., Myers A. D., Pimbblet K., Drinkwater M., 2008, submitted to MNRAS, astro-ph/0801.1816

Acknowledgements

I'd like to thank my supervisor Professor Tom Shanks for his support, time and continuous guidance without which none of the work presented in this thesis would have been possible.

I'd, also, like to thank my family.

Και λύπη αισθάνεται κανείς όχι για την έλλειψη των αγαθών που δεν δοκίμασε ποτέ στην ζωή του, αλλά για τη στέρηση εκείνων, τα οποία πριν του αφαιρεθούν αποτέλεσαν μέρος της ζωής του.

Απόσπασμα από τον επιτάφιο λόγο του Περικλή, 430 π.Χ.

For grief is felt not so much for the want of what we have never known, as for the loss of that to which we have been long accustomed.

From the Funeral Oration of Pericles, 430 B.C.

Contents

List of Figures

List of Tables

Prologue

As the results and analysis in this thesis have already been written as separate papers, chapters 3, 4 and 5 of this thesis are presented largely in the form that they are published (Mountrichas & Shanks 2007a, b, Mountrichas et al. 2008). Each contains a Section which explores the background and relevance of the work presented in that chapter. As a result, the first chapter is not a self-contained introduction to the whole thesis, but rather a brief overview of the current status of cosmology.

Chapter 1

Introduction

1.1 History and First Cosmological Models

The word cosmology consists of the words cosmos and logos and means the logic of cosmos. Its first use goes back in time tracing the first primitive social groups that humankind developed. Its area of interest changed as the meaning of the word cosmos was progressing. At first cosmos was everything with which humans immediately interacted, anything that was included in their daily experience. As time passed by, cosmos started to have a broader meaning. Pythagoras was the first one to use the word cosmos for the universe and nowadays cosmology deals with the dynamical structure, the physical origins and the nature of the universe on its very largest scales.

In 340 B.C. Aristotle, in his book, 'On the Cosmos' he argued that the Earth is spherical and not flat as previously believed. He based his argument on the fact that the Polar Star seems lower on the sky when is observed from the southern areas of the Earth and higher from the Northern. He also argued that only by assuming a spherical Earth one can explain the phenomenon of the eclipse of the Moon. On the other hand, he believed that the Earth was standing steady at the centre of the universe. In the second century, A.C. Ptolemaios, based on this picture for the universe, he created an astronomical model: The Earth is steady at the centre and is surrounded by eight spherical bodies which carry the planets and the stars. The external sphere is carrying the stars that remain at the same positions relative to

each other. The flaw of his model was that in order to predict the positions of the planets he had to assume that the Moon was following a trajectory which brings it some times at a distance from the Earth that is half the usual. So it should appear twice as big. Nevertheless his model was the most successful one in the years to follow. In 1514 A.D. a polish priest, Nicolaus Copernicus, suggested a much simpler model. He assumed that the Sun stands steady at the centre of the universe and that the Earth and the planets are moving in circular orbits around it. His idea though was not taken seriously. Only after a century later Kepler and Galileo start to support his idea. In 1609, Kepler modified this model, suggesting that the planets are following elliptical orbits and not circular. An explanation of these elliptical orbits was given in 1687, by Newton when he published his book, Philosophiae Naturalis Principia Mathematica. In this book, Newton not only created a physical theory of how masses are moving in space and time but he also gave the mathematics needed to analyse this motions.

At the beginning of the twentieth century Einstein's General Relativity came to change the way that scientists were observing and understanding the universe. The important change that Einstein's ideas brought to cosmology was that the universe was not considered static anymore. Although it is possible to consider cosmology in a Newtonian framework, no one had seriously attempted to do so, as it was generally accepted that the universe was devoid of dynamics. The first arguments against an infinite and static universe are attributed to the German philosopher Heinrich Olbers. His argument stemmed from the observation that the sky is dark at night. He suggested that if we accept that this is not a phenomenon of the current epoch then the only way that this can be explained is to assume that the stars were not always bright but they started to emit light at some time in the past. So the night is dark either because the light from these stars has not reached us yet or the intervening matter has not been heated enough to reach a temperature at which it radiates as much as it receives. According to Olbers the universe is either young or it expands. The former contradicts the ages of the oldest stars and so the right answer is that the universe is not static.

Modern cosmology relies on a basic principle which is a generalization of the

Copernican principle, that the Earth is not the centre of the Solar system. That principle states that the universe is homogeneous and isotropic (except for local irregularities) and is called cosmological principle. The confirmation of this principle came in 1965, with the discovery of the Cosmic Microwave Background (CMB), by Penzias and Wilson.

In the rest of this Chapter we shall describe some basic equations and parameters of modern Cosmology and then we shall give the theoretical background of gravitational lensing and correlation function estimators, which consist the basis of this thesis.

1.2 Redshift and Hubble's Law

In everyday experience a phenomenon is known which in Physics is called Doppler shift or Doppler effect. According to that, the frequency of a sound changes relatively to the motion of the source of the sound. Light behaves in a similar way. If the light source is moving, then the electromagnetic wave reaches the observer at a different frequency, and thus different wavelength, than the one emitted. So if a star is approaching Earth its light will be shifted towards the blue region of the spectrum, whereas if it is moving away from the Earth its light will be shifted towards larger wavelengths, i.e. the red area of the spectrum.

Lets consider a source of light and an observer. The source and the observer are moving relative to each other with velocity v_t. The light emitting from the source has wavelength λ_0, as measured by a stationary frame. The source emits two successive pulses with time difference dt' as measured by the stationary frame. The two pulses arrive at the observer with time difference

$$\Delta t = dt' + \frac{v_t dt'}{c} \Leftrightarrow \tag{1.1}$$

$$\Leftrightarrow \frac{\Delta t}{dt'} = 1 + \frac{v_t}{c} \tag{1.2}$$

but $\Delta t = \frac{\lambda}{c}$ and $dt' = \frac{\lambda_0}{c}$, so

$$\frac{\lambda}{\lambda_0} = 1 + \frac{v_t}{c}. \tag{1.3}$$

This is the Doppler shift formula.

In order to have an observable measurement of the expansion of the universe a new variable, the redshift, was introduced. The redshift is defined as

$$z \equiv \frac{\lambda}{\lambda_0} - 1. \tag{1.4}$$

The above equation gives $z = \frac{v}{c}$ for small velocities. In the 1920's Edwin Hubble compared the redshift and the corresponding distance of the nearby galaxies and found that their recession velocity $\vec{v}$ is directly proportional to their distance $\vec{r}$, ie

$$\vec{v} = H_0 \vec{r}, \tag{1.5}$$

where H_0 is the Hubble constant. It is conventional to parameterize its value in terms of the parameter h,

$$H_0 = 100\text{hkms}^{-1}\text{Mpc}^{-1}. \tag{1.6}$$

The value of the Hubble constant as estimated by the WMAP team is $H_0 = 73 \pm 3\text{kms}^{-1}\text{Mpc}^{-1}$ (Spergel et al, 2006) and is close to the estimate from the HST project, $H_0 = 72 \pm 8\text{kms}^{-1}\text{Mpc}^{-1}$ and Cunha et al. (2006) analysis based on SZE/X-ray data, $H_0 = 72^{+4.0}_{-3.5}\text{kms}^{-1}\text{Mpc}^{-1}$.

1.3 Friedmann Equations

In the same way that we need vectors to work in Newtonian theory, we need tensors to work in general relativity. We are not interested here in the geometrical significance and the strict definition of what tensors actually are. We shall mention only the minimum necessary in order to follow the route in history that lead to what is called Friedmann Equations. Thus, a covariant tensor of order 1 is a set of quantities (X_α) in the $x^\alpha-$coordinate system, associated with a point P, which transforms according to

$$X'_{\alpha} = \frac{\partial x^b}{\partial x'^{\alpha}} X_b. \tag{1.7}$$

The rank of a particular tensor is the number of array indices required to describe the quantity. Any symmetric covariant tensor field of rank 2, $X'_{\alpha,b}$ defines a metric. A metric can be used to define distances and lengths of vectors. Thus the geometrical properties of space-time are described by a metric. The simplest metric for an expanding universe in which the Cosmological Principle is valid is called Robertson-Walker metric and has the form

$$ds^2 = (cdt)^2 - \alpha(t)^2[\frac{dr^2}{1-kr^2} + r^2(d\theta^2 + sin^2\theta d\phi^2)], \tag{1.8}$$

where $k = +1$ for positive curvature, $k = 0$ for zero curvature and $k = -1$ for negative curvature.

Using the Robertson-Walker metric, Einstein's General Relativity Equations and assuming that the universe can be approximated by a perfect fluid (Weyl's postulate) we obtain Friedmann equations

$$\frac{\ddot{a}}{a} = -\frac{4}{3}\pi G(\rho + \frac{3p}{c^2}) + \frac{\Lambda c^2}{3} \tag{1.9}$$

$$(\frac{\dot{a}}{a})^2 = \frac{8}{3}\pi G\rho - \frac{kc^2}{a^2} + \frac{\Lambda c^2}{3}. \tag{1.10}$$

The dot denotes derivative with respect to time t. a is the scale factor of the Universe, ρ is the density of matter and radiation in the universe, p the pressure, G the gravitational constant and Λ the cosmological constant which was added later by Einstein in order to avoid an expanding universe.

Friedmann equations can also take a different form which includes the Hubble constant. The velocity can be written as

$$\vec{v} = \frac{d\vec{r}}{dt} = \frac{|\dot{\vec{r}}|}{|\vec{r}|}\vec{r} = \frac{\dot{a}}{a}\vec{r}. \tag{1.11}$$

Comparing equations (1.5) and (1.11) we find a different way to define H (we drop the subscript 0, as it only denotes the value of the variable for the present epoch), i.e.

$$H \equiv \frac{\dot{a}}{a}. \tag{1.12}$$

So Friedmann equations (1.9 and 1.10) can now be written as follows:

$$\frac{\ddot{a}}{a} = \dot{H} + H^2 \tag{1.13}$$

$$(\frac{\dot{a}}{a})^2 = H^2 \tag{1.14}$$

We can also derive an important relationship between the scale factor, a, and redshift, z, i.e.

$$1 + z = \frac{a_0}{a}. \tag{1.15}$$

The last equation relates the redshift directly to the size of the universe.

1.4 The Density of the Universe

Combining together equations (1.10) and (1.14) for $k = 0$ (flat universe), Λ=0 we get a certain density, known as critical density, $\rho_c(t)$

$$\rho_c(t) \equiv \frac{3H^2}{8\pi G}. \tag{1.16}$$

We can then define a quantity that describes the flatness of the universe

$$\Omega_m = \frac{\rho(t)}{\rho_c(t)} = \frac{8\pi G}{3H^2}\rho. \tag{1.17}$$

In a similar way, if we set $\rho = 0$ (no contribution from the matter) and we assume again a flat universe (k=0), we find

$$\Omega_\Lambda = \frac{\Lambda c^2}{3H^2} \tag{1.18}$$

$$\Omega = \Omega_m + \Omega_\Lambda. \tag{1.19}$$

We can now rewrite Friedmann equation (1.10)

$$\Omega - 1 = \frac{kc^2}{a^2 H^2}. \tag{1.20}$$

The ratio $\frac{k}{a^2}$ has dimensions of [length]$^{-2}$ and it defines the curvature of the universe whereas the cosmological constant defines the destiny of the universe. If $k < 0$ ($\Omega < 1$) we get an open universe. If $k > 0$ ($\Omega > 1$) we get a closed universe. If $k = 0$ ($\Omega = 1$) then it stays fixed at this value for all times and the universe is flat. Moreover, for $\Omega_\Lambda < 0$ the universe will recollapse to a Big Crunch. For $\Omega_\Lambda > 0$ it will expand forever (unless there is sufficient matter to cause collapse before Ω_Λ becomes important). If $\Omega_\Lambda = 0$, then the universe will expand forever if $\Omega_m \leq 1$ and it will recollapse if $\Omega_m > 1$. We note that if $\Omega_\Lambda \neq 0$, then there is no necessary relationship between spatial curvature, k, and the fate of the universe (Carroll, 2001).

Observational measurements give different values for Ω_m. Its accurate measurement is one of the most important areas of research for modern cosmology. Measurements of the angular power spectrum of the CMB (Spergel et al. 2006) give $\Omega_m h^2 = 0.127^{+0.007}_{-0.013}$. Percival et al. (2006) suggest $\Omega_m = 0.256^{+0.029}_{-0.024}$. Tegmark et al. (2006) find $\Omega_m = 0.24 \pm 0.02$. A value of $\Omega_m = 0.3$ and $\Omega_\Lambda = 0.7$ for a flat universe is generally accepted.

Now that basic parameters of modern cosmology have been described, in the next Sections of this Chapter we shall give a description of gravitational lensing and correlation functions.

1.5 Gravitational Lensing

1.5.1 Deflection Angle

One very interesting application of the theory of general relativity to cosmology is the gravitational deflection of light as it passes through great concentrations of mass, such as galaxies and clusters of galaxies. This effect will be one of the subjects mainly studied in this thesis and some of the most important equations of its theory will be presented next.

If ϕ is the gravitational potential of a pointlike mass M at a distance r, where

$$\phi = -GM/r, \tag{1.21}$$

where G is the gravitational constant, then the deflection angle α of a light ray passing through this gravitational potential is given by the general relativity

$$\alpha = \frac{4GM}{\chi c^2}, \tag{1.22}$$

with χ being the smallest distance to the mass M. This turns out to be twice the deflection angle given by the Newtonian theory.

Now we shall estimate this deflection angle in the case that the mass M is not pointlike but distributed spherically which is a very good approximation for an isolated galaxy. The mass, in this case, is a function of the distance r from the core of the spherical distribution, which spherical distribution we assume is isothermal, i.e. the velocity dispersion σ is independent of the radius. Then the gas pressure is

$$p = \rho(r)\sigma^2, \tag{1.23}$$

where σ is the one dimensional line-of-sight velocity dispersion assuming the velocity distribution is isotropic. The equation of the hydrostatic equilibrium states that the pressure force per unit volume (-dp/dr) and the gravitation force (gρ) per unit volume balance each other,

$$-\frac{dp}{dr} = \frac{GM(r)}{r^2}\rho(r). \tag{1.24}$$

Outside the core the density follows the power law form of $\rho \propto 1/r^2$. Thus,

$$M(r) = \frac{2\sigma^2 r}{G}. \tag{1.25}$$

The gravitational potential is then given by

$$\phi(r) = \int_0^r drGM/r^2 = 2\sigma^2 lnr. \tag{1.26}$$

Then the deflection angle worked out in general relativity is

$$\alpha = 4\pi(\sigma/c)^2, \tag{1.27}$$

where c is the speed of light.

1.5.2 Geometry of Gravitational Lensing

Let us assume that d_{ol} is the distance between an observer and the large concentration of mass (lens, e.g. cluster of galaxies), d_{ls} the distance between the lens and the source (e.g. QSO) and d_{os} the distance between the observer and the source. In a flat cosmological model: $d_{os} = d_{ol} + d_{ls}$. A light ray emitted from the source passes through the gravitational potential of the lens and is deflected by an angle α given by the equation 1.22. The angular distance between the image of the source seen because of the effect of lensing and that without the presence of the lens is given by θ' and θ is the angular distance between the image and the lens. Now if θ_q is the angle between the source and the lens, then

$$\eta = \theta_q d_{os}. \tag{1.28}$$

The last equation can be rewritten as

$$\eta = \theta d_{os} - \alpha d_{ls} \tag{1.29}$$

$$\theta_q = \theta - \frac{d_{ls}}{d_{os}}\alpha, \tag{1.30}$$

and substituting α from equation 1.22 we finally get the Lens Equation

$$\theta_q = \theta - \frac{d_{ls}}{d_{os}}\frac{4GM}{\chi c^2}. \tag{1.31}$$

1.5.3 Einstein Ring

Let us assume a specific geometry of the observer, the lens and the source. Let assume $\theta_q = 0$, i.e. the observer, the lens and the source are aligned. Then θ can be written as

$$\theta = \frac{d_{ls}}{d_{os}}\frac{4GM}{\chi c^2}, \tag{1.32}$$

where $\chi = d_{ol}\theta$ and in the case we study $\theta = \theta_E$ the so-called "Einstein Radius". Therefore,

$$\theta_E^2 = \frac{4GM}{c^2}\frac{d_{ls}}{d_{os}d_{ol}}. \tag{1.33}$$

Thus, in this case the images are displaced symmetrically about the lens and for a rotational symmetry about the line-of-sight they sweep a ring, known as Einstein Ring. Now θ_q can be rewritten as

$$\theta_q = \theta - \frac{\theta_E^2}{\theta}, \tag{1.34}$$

with solutions

$$\frac{1}{2}(\theta_q \pm \sqrt{\theta_q^2 + 4\theta_E^2}). \tag{1.35}$$

1.5.4 Magnification Bias

Gravitational lensing has two effects on the image of a source, namely the amplification effect and the solid angle effect. The amplification effect brightens the apparent magnitude of the background sources resulting in an increase of the objects that we observe in a magnitude limited survey. On the other hand, lensing effectively reduces the solid angle behind the lens, resulting in a decrease of the number of background sources. Let A_i and A_s be the area of the image and the source, respectively. If ω_e is the emitted solid angle and ω_o is the observed solid angle then the magnification, μ, is given by

$$\mu = \frac{\omega_e}{\omega_o} = \frac{A_i}{A_s}(\frac{d_{os}}{d_{ol}})^2. \tag{1.36}$$

Since,

$$A_s = d_{os}^2\theta_q d\theta_q \tan\phi \tag{1.37}$$

$$A_i = d_{ol}^2\theta d\theta \tan\phi, \tag{1.38}$$

we get for the magnification μ

$$\mu = |\frac{\theta}{\theta_q}\frac{d\theta}{d\theta_q}|. \tag{1.39}$$

As mentioned before lensing has two competing effects. The first is two increase the flux of an image comparing to the flux of its source, increasing the numbers of objects that we observe in a survey with magnitude limit m, by the factor $\frac{N(<m+2.5log\mu)}{N(<m)}$ and the second is to distort the solid angle behind the lens, reducing the number of objects observed by a factor $1/\mu$. Therefore, the number of objects we observe in the presence of lensing comparing to the number observed in the absence of lensing is given by (Narayan 1989)

$$q = \frac{1}{\mu}\frac{N(< m + 2.5log\mu)}{N(< m)}. \tag{1.40}$$

The application of this effect will be studied in Chapter 3 where we shall see the different lensing results for faint and bright QSO samples.

1.6 The two-point correlation function

A very useful statistical tool for measuring the clustering of the objects is the two-point correlation function. In 2-D space, the most commonly used correlation function, is the so-called angular correlation function $w(\theta)$, which measures the probability of finding a pair of objects within an angle, θ, relative to what would be expected from a uniform distribution (Poisson distribution). This uniform distribution is, usually, given by a number catalogue which is constructed following the real distribution of objects as a prescription and creating random points taking into account the completeness and general conditions of the real catalogue. A generalisation of the two-dimensional correlation function $w(\theta)$, is the three-dimensional correlation function $\xi(r)$, where we are interested in the entire volume of a survey.

The basic idea, on which correlation functions are based, is as follows. The probability to find an object within a volume element dV is

$$dP = ndV, \tag{1.41}$$

where n is the number density of the object. Now the joint probability of finding objects in solid angles $\delta\Omega_1$, $\delta\Omega_2$ separated by an angle θ and with a mean number density N, is given by

$$dP(\theta) = N^2[1 + w(\theta)]\delta\Omega_1\delta\Omega_2, \tag{1.42}$$

where $w(\theta)$ is the angular correlation function. In the same way, the spatial (3-D) correlation function, $\xi(x)$ is defined as

$$dP(x) = n^2(z)[1 + \xi(x)]dV_1dV_2, \tag{1.43}$$

where dV_1 and dV_2 are two volume elements, x is the separation between the two objects and n(z) is the spatial density.

In practice one counts the number of data-data pairs (DD), random-random pairs (RR) and data-random pairs (DR) in the volume of the sky that we are interested in. Different estimators have been developed to evaluate ξ. The most common one and also the one used in this thesis is the following estimator developed by Peebles (1979) which is given by

$$\xi(x) = \frac{< DD(x) >}{< DR(x) >}\frac{n_{ran}}{n_{data}} - 1, \tag{1.44}$$

where n_{ran} is the number of random points used for the cross-correlation and n_{data} is the number of data points, e.g. QSOs. So, the $\frac{n_{ran}}{n_{data}}$ factor normalises the number density of random points to that of the data. Another correlation function, is the Hamilton (1993) estimator given by

$$\xi(x) = \frac{< DD(x) >< RR(x) >}{< DR(x) >^2} - 1. \tag{1.45}$$

Finally, one more correlation estimator is the one developed by Landy and Szalay (1993)

$$\xi(x) = \frac{< DD(x) > -2 < DR(x) > \frac{n_{data}}{n_{ran}} + < RR(x) > (\frac{n_{data}}{n_{ran}})^2}{< RR(x) > (\frac{n_{data}}{n_{ran}})^2}. \tag{1.46}$$

Hamilton and Landy and Szalay estimators give more accurate results when the scale of interest is close to the sample size. As already mentioned the estimator

mostly used in this thesis is the one given by equation 1.44. If a different estimator is used somewhere, it will be mentioned.

1.7 Error Estimators

In this Section we shall present the error estimators used in this work. One very common error estimator is the so-called Poisson estimator given by

$$\sigma_\omega(\theta) = \frac{\sqrt{DD}}{DR}. \tag{1.47}$$

The Poisson estimator assumes that the pairs in each bin are independent. However, this is not the case especially at large separations where the objects are strongly clustered. This causes an underestimation in the Poisson error compared to the true error of the measurements, on large scale. On the other hand, the Poisson errors are an overestimation in very small scales. Throughout this thesis we use the so-called Field-to-Field error estimator (unless otherwise stated).

In order to measure the Field-to-Field errors we need a large enough area with an adequate number of observed objects. Then, we divide this area into sub-areas and cross-correlate each one separately. The variance between the subsamples is measured. Finally, the error is given by the standard error between the subsamples inverse weighted by variance to account for different number of objects in each subsample, i.e.

$$\sigma_\omega^2 = \frac{1}{N-1}\sum_{L=1}^{N}\frac{DR_L(\theta)}{DR(\theta)}[\omega_L(\theta) - \omega(\theta)]^2, \tag{1.48}$$

where N is the number of the sub-areas in which the initial area is divided, $DR_L(\theta)$ and $DR(\theta)$ are the data-random points of the sub-area and the total area, respectively and $\omega_L(\theta)$ and $\omega(\theta)$ are the correlation function measurements for the sub-area and total area, respectively.

A comparison between Poisson and Field-to-Field errors, in the case of galaxies-clusters cross-correlation, will be given later on (Chapter 5).

1.8 From spatial to angular correlation function

A relationship between the angular correlation function and the spatial correlation function can be derived, if we make assumptions about the true distribution in space of the objects we are interested in and the selection criteria of the sample we use. This relationship is given by Limber (Limber's formula, 1953). When the samples used are shallow then Limber's formula yields a simple scaling factor (Peebles, 1973). Things become more complicated when very deep samples are considered, where relativistic and evolutionary effects are not negligible.

These effects introduce four additional factors. First, proper lengths and the angles they subtend become curved. This effect is important regardless of the underlying cosmology. Second, at high redshifts the K-correction factor cannot be neglected (K-correction is due to the fact that astronomical measurements are taken through a single filter or a single bandpass. Therefore, one only sees a fraction of the total spectrum, redshifted into the frame of the observer). The third factor is that a deep sample contains objects at high redshifts, i.e. the depth of the sample depends on the brightness evolution of the objects. Finally, the clustering evolution of the objects should be taken into account.

Following Phillipps et al. (1978) we shall derive a relativistic generalization of Limber's equation. In order to do that we multiple equation 1.43 by the joint selection function $\phi(z_1)$, $\phi(z_2)$, integrate over line-of-sights z_1, z_2 and equate with equation 1.42, i.e.

$$N^2[1+w(\theta)] = \int_0^\infty dz_1 f^2(z_1) g(z_1) n(z_1) \phi(z_1) \int_0^\infty dz_2 f^2(z_2) g(z_2) n(z_2) \phi(z_2) [1+\xi(r)], \tag{1.49}$$

where $f(z)$ is the angular diameter distance of the objects and $g(z)$ is the derivative of the proper distance with respect to z. Assuming that $n(z)$ varies as $(1+z)^3$ and that ϕ varies much more slowly than ξ, the last equation gives,

$$w(\theta) = \frac{\int_0^\infty dz f^4(z) g^2(z) \phi^2(z) (1+z)^6 \int_{-\infty}^\infty dy \xi([f^2(z)\theta^2 + g^2(z) y^2]^{\frac{1}{2}})}{[\int_0^\infty dz f^2(z) g(z) (1+z)^3 \phi(z)]^2}, \tag{1.50}$$

where we have changed (z_1, z_2) to (z, y). This equation will be used in Chapter 4.

1.9 Outline of the thesis

The aim of this thesis is to analyze statistically the available large QSO, LRG, galaxy and cluster samples in order to estimate the QSO-galaxy lensing anti-correlation signal and measure the mass of foreground galaxies and clusters and to estimate the QSO-LRG clustering amplitude, the QSO bias and their dependence on QSO luminosity. We also investigate the behaviour of the group-galaxy infall parameter and their rms velocity dispersions for different group memberships. The aim here is to make dynamical estimates of the group masses to check the QSO lensing results.

In Chapter 2 we describe the main QSO surveys used in this thesis. Given that the accuracy of photometric QSO redshifts is very important for lensing purposes (intrinsic clustering) we test this accuracy by comparing our photometric QSO sample with spectroscopic data sets. In Chapter 3 we investigate the reasons for the discrepancy on the QSO-galaxy anti-correlation signal between Myers et al. 2003 and Scranton et al. 2005 results. In Chapter 4, we estimate the QSO-LRG clustering amplitude and the QSO bias as well as their dependence on QSO luminosity, using both a redshift-space distortion and an amplitude analysis. In Chapter 5, we study the behaviour of the infall parameter, β, for group-galaxies of different membership, as well as their rms velocity dispersion via the redshift distortion of the group-galaxy cross-correlation functions. Finally, in Chapter 6 we summarize the conclusions of this work.

Chapter 2

QSO redshift surveys

2.1 Introduction

In Sections 2.2-2.4 of this Chapter we shall outline the three main QSO surveys used in this thesis, i.e. 2QZ, SDSS and 2SLAQ. In Section 2.5 we shall check for systematic effects in our QSO cross-correlations analysis by using stars as control sample and in Section 2.6 we shall compare our photometric QSO redshifts (SDSS) with spectroscopic catalogues in order to estimate the contamination level in our photo-z QSO sample. The latter will be used in Chapter 3 to correct our lensing signal.

2.2 The 2dF QSO Redshift Survey

The 2QZ covers two areas on the sky, one in the North Galactic Cap (NGC) with $147°.5 \leq \mathrm{ra} \leq 222°.5$ and $-2°.5 \leq \mathrm{dec} \leq 2°.5$ and one in the South Galactic Cap (SGC) with $325°.0 \leq \mathrm{ra} \leq 48°.75$ and $-32°.5 \leq dec \leq -27°.5$. The 2QZ QSO target sample (Smith et al. 1997) was UVX-selected from colour cuts in the $(u - b_j), (b_j - r)$ plane within a magnitude range of $18.25 \leq b_j \leq 20.85$. The final 2QZ catalogue consists of 22,159 QSOs. Out of the 22,159 QSOs, 12,303 are located in the SGC and 9,856 in the NGC in a redshift range of $0.12 \leq z \leq 3.5$ and $0.1 \leq z \leq 3.2$, respectively, although the completeness drops at redshifts higher than $z > 2.2$. Throughout this thesis we use QSOs in the NGP with quality '11' and

$z \leq 2.2$, unless stated otherwise. The quality for each object has been assigned by two different observers and it refers to the quality of the spectrum of the object. '1' means good spectrum quality, '2' means poor and '3' when an identification could not be assigned to the object. A QSO spectrum consists of many absorption lines which trace the intervening gas along our line of sight to any QSO, in addition to strong emission lines intrinsic to the QSO itself.

The spectra were taken with the Two-degree Field (2dF) spectrograph which has one important restriction on the placement of the 2dF fibre, i.e. the smallest angle between two objects in a 2QZ field is 30 arcsec, which in turn means that there may be a paucity of objects at small separations (fibre collisions problem). Nevertheless, this doesn't affect our results, as QSOs were given a higher observational priority and we expect only few to be rejected due to their proximity to galaxies. Moreover, most of the 2QZ fields were observed more than once to avoid these fibre allocation problems (23.6% of the objects have more than one spectroscopic observation).

2.3 The Sloan Sky Digital Survey

The Sloan Sky Digital Survey (SDSS) is an imaging and spectroscopic survey of the sky. It uses a wide-field 2.5-m telescope (Gunn et al. 2006) at Apache Point Observatory, New Mexico. SDSS has the advantage to gather images in five broad bands, (u, g, r, i, z) in a range of 3,200-10,000 $\AA$. The Data Release 6 (DR6) was published in June, 2007. It covers 9,583 square degrees and has spectra for 1,271,680 objects (7,425 sq. degrees) which include 790,860 galaxies, 90,108 QSOs with $z < 2.3$ and 13,539 QSOs with $z \geq 2.3$.

Our SDSS QSO sample consists of DR1 photometric QSOs extracted by Richards et al. (2004). Their catalogue consists of 100,563 QSO candidates to $g = 21$ from $2099 deg^2$ of the SDSS DR1 imaging data. The method used to estimate these photometric redshifts is described in detail by Weinstein et al. (2004). Very briefly, they use two sets of QSOs. For the QSOs in the first set they have spectra and for those in the second set they have photometry, i.e. the five broad bands of SDSS. Then, they sort the spectroscopic QSOs into redshift bins. Next, they plot the

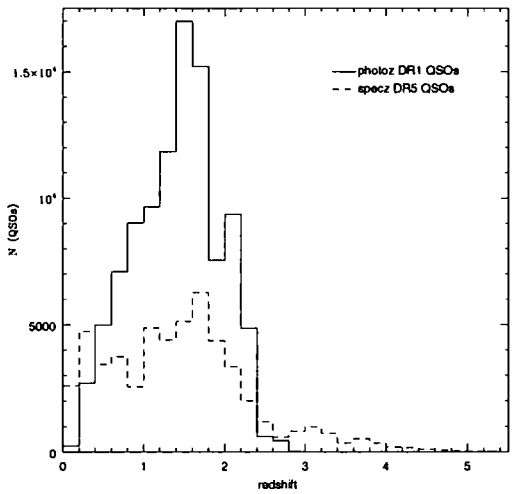

Figure 2.1: Redshift-number counts of our photometric SDSS DR1 QSOs (solid line) and spectroscopic SDSS DR3 QSOs (dashed line).

SDSS colours of their photometric QSOs as functions of redshift. Most QSOs in a particular redshift bin have very similar colours, and it is this colour-redshift relation that they parameterize. Instead of estimating a Gaussian redshift error, they use an upper and lower redshift bound along with the likelihood that the redshift was within those bounds. In this work we use a QSO sample which consists of QSO within the redshift range of $1.0 \leq z \leq 2.2$ as well a second QSO sample in which QSOs have redshifts $z_{low} \geq 1.0$ and $z_{up} \leq 2.2$. In the first case our sample has 37,876 QSOs and in the second case 29,297 QSOs. The redshift-number counts for the former photometric QSO sample are shown in Fig. 2.1 (solid line).

We also use spectroscopic SDSS QSOs. Our sample in this case has been extracted from DR5 ($i_{AB} < 19.1$) and in total it consists of 79,394 QSOs with $z < 2.3$ and 11,217 QSOs with $z > 2.3$ with redshift confidence level more than 0.9 ($zConf > 0.9$). The spectroscopic redshift-number counts are also shown in Fig. 2.1 (dashed line). The redshift distribution is more uniform for spectroscopic QSOs than for photometric QSOs, in the redshift range of our interest ($0.3 \leq z \leq 2.2$). This is mainly because of the brighter magnitude limit for the spectroscopic sample.

2.4 The 2dF-SDSS LRG and QSO Survey

The 2dF-SDSS LRG And QSO (2SLAQ) survey is focused on studying the redshift evolution of Luminous Red Galaxies (LRGs) and faint QSOs. It combines the precision of the SDSS photometric survey with spectroscopic capabilities of the 2dF instrument (Cannon et al. 2006). The survey covers two narrow stripes along the celestial equator. The Northern Stripe runs from $08.^h4$ to $15.^h3$ in RA and it consists of 5 sub-strips (a, b, c, d, e). The Southern Stripe runs from $20.^h6$ to $04.^h0$ (one strip, s, see Cannon et al. 2006, Fig. 2). In this thesis QSOs from the NGP will be used, unless stated otherwise. Their magnitude limit is $18.0 \leq g \leq 21.85$.

As 2SLAQ uses the same instrument as 2QZ (2dF) it also suffers from the fibre collisions problem. This bias is partially overcome (but not to the same degree as for 2QZ) within the overlap regions of adjacent 2dF fields. The bias is also alleviated by the policy of re-allocating some fibres after the first night on a given field (Cannon et al. 2006). The bias is larger for QSOs, as LRGs were given higher priority than QSOs in the allocation process of 2SLAQ (in the 2QZ survey QSOs had a higher priority). So QSOs which lie near LRGs will not be observed. The fibre collision effect will be addressed in Chapter 4.

2.5 Star-galaxy cross-correlation results

In the next Sections of this Chapter we shall perform some check tests which are vital for the accuracy of our lensing measurements, presented in the following Chapter. In this Section we check the consistency between the SDSS DR4 galaxies in the NGP 2QZ area and the random catalogue we use to replace them.

Apart from the QSOs, galaxies and LRGs that are the main objects used in this thesis, all three of the surveys mentioned above include other types of objects, such as stars and NELGs. Stars can be used as control samples as they display no cosmological signature and so their cross-correlation with galaxy samples can be used to reveal gradients in the galaxy samples which are not recreated in the random catalogues and affect QSO-galaxy or QSO-galaxy group cross-correlation results. We do not expect the star-galaxy cross-correlations to be flat on small

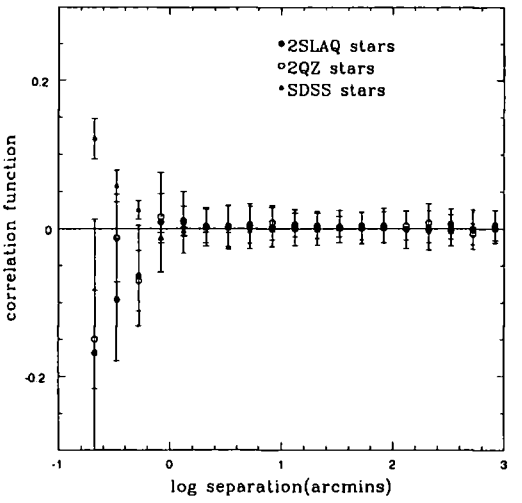

Figure 2.2: Star-galaxy cross correlation results. Filled circles show the results from the 2SLAQ stars, open circles from the 2QZ stars and triangles from the SDSS stars. The average stellar signature is flat.

scales because of the galaxy contamination in the star samples (5%-10%).

Fig. 2.2 shows the star-galaxy cross-correlations for three different star samples, i.e. 1,961 2QZ stars (open circles), 497 2SLAQ stars (filled circles) and 543,281 SDSS stars (triangles). All three cross-correlations have been done in the NGP of the 2QZ area, which is a common area for the three surveys and the galaxy sample (same in all cases) consists of 450,480 SDSS DR4 galaxies ($g < 21$) which is the galaxy sample we use for the QSO-galaxy cross-correlations (Chapter 3) in this area. On small scales ($\theta \leq 1'$) the anti-correlation signal detected using the 2SLAQ and 2QZ star samples, is probably due to statistics. The positive correlation detected using the (larger) SDSS star sample is probably, as already mentioned, due to the galaxy contamination of the star sample. Nevertheless, the average result from the three star samples is, as expected, null on scales larger than $1'$.

2.6 Comparison Between Photometric and Spectroscopic Redshifts

As previously noted our SDSS DR1 QSO sample consists of photometric QSOs that are derived using the method described by Richards et al. (2005) and is similar to the method that has been used by Scranton et al. (2005). In this Section we examine the contamination percentage in our SDSS DR1 photometric sample to assess whether it is high enough to affect the lensing results presented in the next Chapter (see Section 3.5.1).

The contamination that is most important is the fraction of low redshift QSOs and compact narrow emission-line galaxies (NELGs) in the $1.0 < z_p < 2.2$ QSO photo-z sample since they can confuse any lensing signal with intrinsic clustering with the galaxies. Thus, we want our photometric QSO redshifts to be as accurate as possible. We shall also be include stellar contamination which can dilute to a lesser extent the lensing signal. Richards et al. (2004) and also Myers et al. (2007) claim 5% non-QSO contamination over the full magnitude and redshift range. We now wish to check this number and, more importantly, also determine the contamination of the $1 < z_p < 2.2$ QSO photo-z sample by $z_s < 0.6$ ($z_s < 0.3$) QSOs and NELGs that may affect cross-correlation with $r < 21$ ($g < 21$) galaxies. Our analysis studies the contamination level in the DR1 photometric QSO sample we use ($g < 21$) regardless the QSO magnitudes (see Fig. 8 of Richards et al. 2004).

As mentioned, the algorithm developed by the SDSS team uses upper and lower limits for the redshifts assigned. Thus, in what follows we check the contamination level in the $1.0 < z_p < 2.2$ QSO photo-z sample as well as a separate check which uses the lower and upper confidence limits of the DR1 spectroscopic redshifts, i.e $z_{low} \geq 1.0$ and $z_{up} \leq 2.2$. We shall check if there are differences in the two analyses. Although, as we shall see next, the results between the two analyses are very similar we shall base our corrections in Chapter 3 on the $1.0 < z_p < 2.2$ estimations, according to our published paper.

2.6.1 Comparison with the 2QZ catalogue

In order to check the contamination in the photometric DR1 QSO sample we first compare it with the 2QZ catalogue. In the 2QZ there are 23,290 objects and in our DR1 QSO sample 4,535 QSOs in the 2QZ area, with $g < 20.85$, $1.0 < z_p < 2.2$. 3,025 objects are common in the two sets. 2,516 of these objects have been identified as QSOs in the 2QZ and 509 have different or no ID in the 2QZ, i.e. 16 are NELGs, 91 stars and 402 have not been identified by the 2QZ team. Finally, 1,510 ($= 4,535 - 3,025$) DR1 QSOs are not included in the 2QZ. Fig. 2.3 shows the photometric vs. the spectroscopic redshift of the common objects (including stars, NELGS and objects with no ID). The objects that interest us (contaminants) are those that lie within the rectangle. Table 2.1 summarises the contamination statistics as derived from the plot. There are 169 low spectroscopic redshift QSOs and NELGs in a total of 2,024 objects (Table 2.2). According to these numbers we find a contamination of $(8.3 \pm 0.6)\%$ for objects that have photometric redshift between $1.0 < z_p < 2.2$ and 2QZ spectroscopic redshift $z_s < 1.0$. In the same way the contamination of spectroscopic redshift $z_s < 0.6$ objects is $(3.6 \pm 0.4)\%$ (73 low spectroscopic redshift QSOs and NELGs in a total of 2,024 objects). Finally, for $z < 0.3$ the contamination is $(0.6 \pm 0.2)\%$ (12 spectroscopic redshift QSOs and NELGs at low-z in a total of 2,024 objects).

Comparing next the 2QZ catalogue with our $z_{low} \geq 1.0$ and $z_{up} \leq 2.2$ photometric QSOs, we find 1,504 matching (common) objects between the 2 data sets. Among those there are 112 objects that have 2QZ spectroscopic redshift $z_s < 1.0$ (18 of those are NELGs). So the contamination level is $7.5 \pm 0.7\%$. If we repeat the same analysis for spectroscopic redshift $z_s < 0.6$ we find 66 contaminants (17 NELGs and 49 QSOs), i.e. $4.4 \pm 0.5\%$. Finally, for $z_s < 0.3$ the contamination percentage is $0.5 \pm 0.2\%$. The contamination levels are shown in Table 2.3.

DR1 objects that have been identified as stars in the 2QZ also dilute any anti-correlation by the factor $(1 - f_s)^2$ where f_s is the fraction of stars in the DR1 sample. This effect of including uncorrelated stars is usually much smaller than the effect of including low redshift NELGs and QSOs. From Table 2.1 $f_s = 55/2024 = 2.7\%$ giving $(1 - f_s)^2 = 0.95$ which implies that the anti-correlation is also decreased by

$\approx 5\%$ due to star contamination.

2.6.2 Comparison with the 2QZ+SDSS catalogue

The DR1 QSO catalogue we are using has also spectroscopic redshifts for the QSOs wherever available, either from the 2QZ or from spectra obtained by SDSS. Based on this information there are 1,215 NELGs and QSOs with photometric redshift $1.0 < z_p < 2.2$ and spectroscopic redshift $z_s < 1.0$ out of 15,776 objects. So the overall contamination is $(7.7 \pm 0.2)\%$. For spectroscopic redshift $z_s < 0.6$ there are 594 contaminating QSOs and NELGs so the contamination is now $(3.8 \pm 0.2)\%$ and finally for $z_s < 0.3$ there are 134 low spectroscopic QSOs and NELGs and the contamination is $(0.9 \pm 0.1)\%$ (Table 2.2).

For our $z_{low} \geq 1.0$ and $z_{up} \leq 2.2$ QSO sample we find 817 NELGs and QSOs with $z_s < 1.0$ out of 11,359 objects, i.e. $(7.2 \pm 0.3)\%$. For spectroscopic redshift $z_s < 0.6$ there are 466 contaminating QSOs and NELGs so the contamination is now $(4.1 \pm 0.2)\%$ and finally for $z_s < 0.3$ there are 91 low spectroscopic QSOs and NELGs and the contamination is $(0.8 \pm 0.1)\%$ (Table 2.3).

2.6.3 Comparison with QSOs in the COSMOS field

Next we repeated the same procedure using the QSO spectroscopic sample from Prescott et al. (2006). In that paper they identify 95 QSOs in the COSMOS field that are also contained in the SDSS sample. The QSOs lie within $18.3 < g < 22.5$ and a range in redshift $0.2 < z < 2.3$. 42 out of these 95 QSOs are in our DR1 sample at its $g < 21$ limit and 31 have $1.0 < z_p < 2.2$. So in a similar way we plot their spectroscopic redshift (from Prescott et al.) against their photometric redshift (from our DR1 sample) in Fig. 2.4. As we see there are three contaminants (open circles) out of the 31 objects that have photometric redshift between $1 < z_p < 2.2$ (asterisks), so the contamination now is $(9.7 \pm 5.6)\%$ with spectroscopic redshift $z < 1.0$. Only one of these 3 has $z < 0.6$ and this has $z = 0.0375$ which makes the contamination $(3.2 \pm 3.2)\%$ both for spectroscopic redshift ranges $z < 0.6$ and $z < 0.3$ but the sample may be too small to draw any strong conclusion.

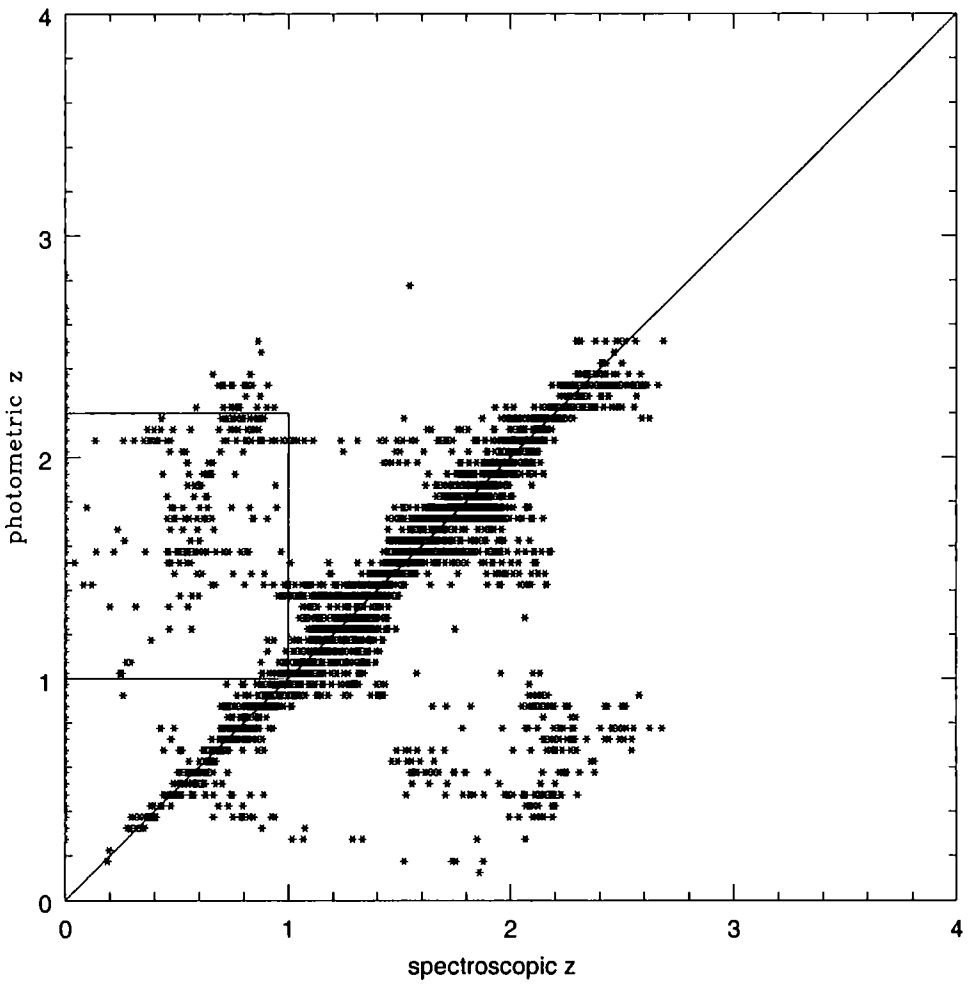

Figure 2.3: Photometric vs. spectroscopic redshift for the common objects between the DR1 and 2QZ catalogues.

Repeating the previous analysis for $z_{low} \geq 1.0$ and $z_{up} \leq 2.2$ we find 22 common QSOs between the 2 data sets. Among those, there are 2 QSOs with $z_s < 1.0$ ($9.1 \pm 6.4\%$), and 1 with $z_s < 0.3$ ($4.5 \pm 4.5\%$). The contamination level percentage is again shown in Table 2.3.

2.6.4 Comparison with spectroscopic QSOs from AAOmega

In order to check the contamination statistics particularly of the $\simeq \frac{1}{3}$ DR1 QSOs that lie outside the 2QZ selection at $g < 21$ we made new AAOmega (Sharp et al. 2006) observations in four fields, on the nights of 3-7 March 2006 inclusive. These fields are the COSMOS field with centre 10 00 28.8 02 12 21, the COMBO17 S11 with 11 42 58.0 -01 42 50, the 2SLAQ d05 with 13 21 36.0 -00 12 35 and the 2SLAQ e04 14 47 36.0 -00 12 35 (see Section 3.1 and Tables 1 and 2 of Ross et al. 2007 for details). Basic QSO spectral reduction was done by S.M. Croom using the 2dfdr package.

For the identification of QSOs and assignment of redshifts we used the AUTOZ and 2DFEMLINES routines written by Lance Miller and Scott Croom for the 2QZ (see Section 3.1 of Croom et al. 2001 and Section 2.3.1 of Croom et al. 2004). We first used AUTOZ which automatically identifies objects and assigns redshifts to them. Then, using the 2DFEMLINES program we checked these redshifts by eye. This program steps through each object in the file created by the AUTOZ in turn, starting with the best IDs though the worst. If the ID and the redshift are ok we moved to the next object. If either the identification or the redshift were not secure a '? quality flag was put next to the ID or redshift. For our calculations we have taken into account spectra that have unambiguous redshifts. That means that whenever we had to add a question mark to the redshift then this object was excluded as a potential contaminant but was still counted as a common object.

There are 123 QSO spectra taken for DR1 QSOs ($1.0 < z_p < 2.2$) that are not previously included in a spectroscopic catalogue. From these 123 objects identified as QSOs in our DR1 QSO photometric sample there were 5 NELGs with $z \leq 0.3$ and 1 QSO with $z < 0.6$. So from the comparison of our photometric sample with this spectroscopic one, the contamination is $(4.1 \pm 1.8)\%$ for $z \leq 0.3$ and $(4.9 \pm 2.0)\%$

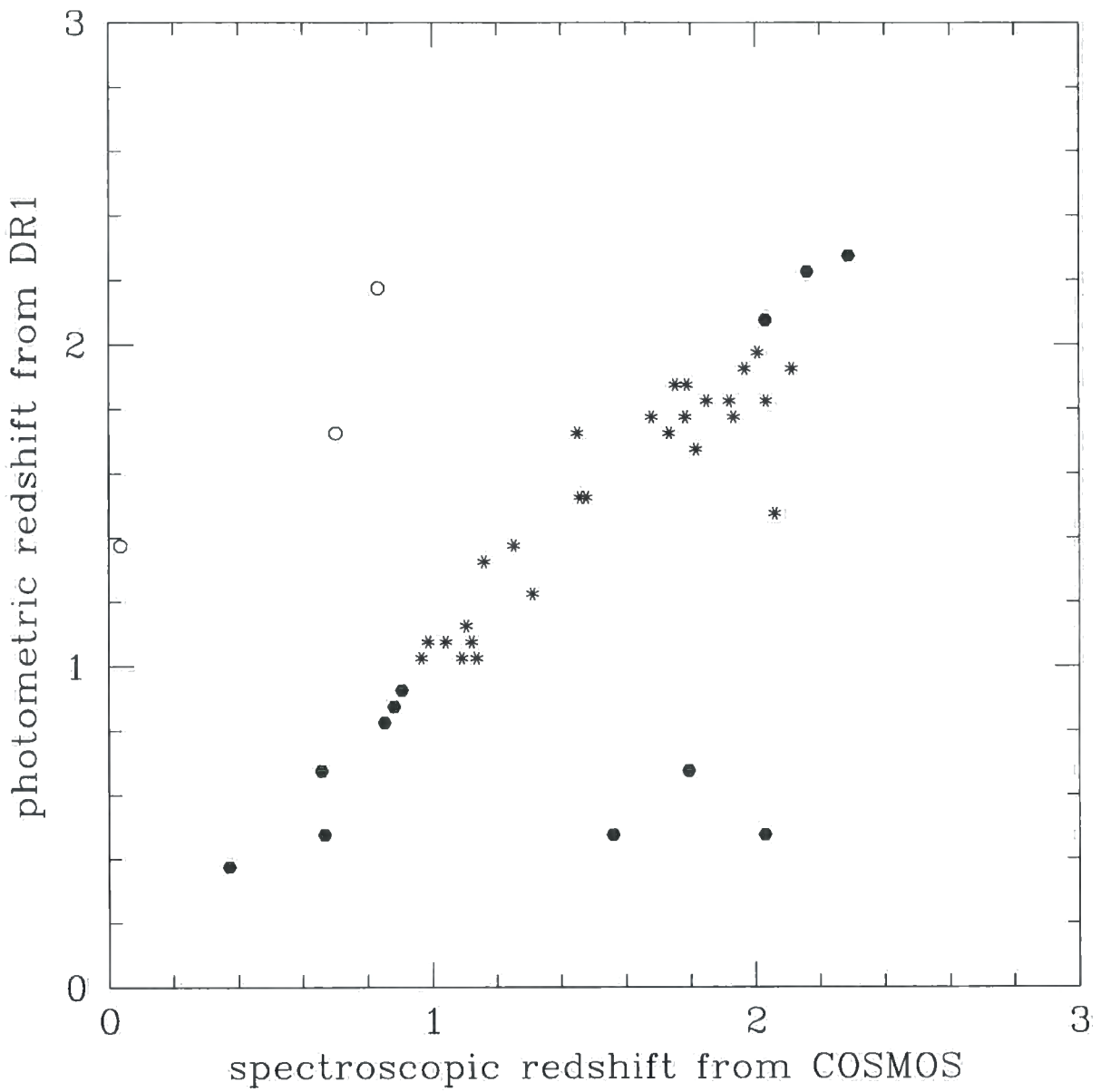

Figure 2.4: Spectroscopic redshifts (from Prescott et al.) against photometric redshifts (from DR1 sample). The open circles are the three contaminants and the asterisks are the objects with photometric redshift $1.0 < z_p < 2.2$.

for $z \leq 0.6$. For these calculations we have only taken into account first-class spectra that have unambiguous redshifts. That means that whenever we had to add a question mark to the redshift then this object was excluded as a potential contaminant but was still counted in the 123 objects. If we exclude these objects as well from the total number of objects, then the total number of good spectra falls to 78 and the contamination goes up to $(6.4 \pm 2.9)\%$ for $z \leq 0.3$ and $(7.7 \pm 3.4)\%$ for $z \leq 0.5$. The former, more conservative, numbers are listed in Table 2.2.

Repeating the analysis now with the upper and lower limits for redshifts, we find 89 common objects between AAOmega and our photometric QSO catalogue with $z_{low} \geq 1.0$ and $z_{up} \leq 2.2$. 9 objects have $z_s < 1.0$ and 6 objects have $z_s < 0.6$ (Table 2.3).

Now we shall present the spectra of these 6 contaminants that are not included in previous spectroscopic catalogues. One of these contaminants is in the e04 field. This object in the SDSS DR1 data set is identified as a quasar with photometric redshift $z_p = 1.575$. As we can see from its spectrum in Fig. 2.5, it is actually a galaxy at redshift $z_s = 0.1386$. A second contaminant is in the d05 field. Its photometric SDSS redshift is $z_p = 1.575$, whereas its spectrum shown in Fig. 2.6 reveals that it is a NELG at redshift $z_s = 0.2007$. One more contaminant is in the S11 field. Its photometric redshift in SDSS is $z_p = 1.525$, whereas it is a NELG at $z_s = 0.1481$. Finally, there are three more contaminants in the COSMOS field. Two of them are NELGs at $z_s = 0.3744$ and $z_s = 0.2194$, instead of QSOs at $z_p = 1.325$ and $z_p = 1.575$. (Figures 2.8 and 2.9). It should be noted that the latter object is also included in the Prescott et al. spectroscopic QSO catalogue, but is identified as a QSO at $z = 1.1616$. The third contaminant in the COSMOS field is indeed a QSO but at $z_s = 0.5194$ and not $z_p = 1.575$, as assigned by the SDSS team. Its spectrum is in Fig. 2.10. We notice that half of the contaminants mentioned above are in the same redshift bin, i.e. have photometric redshift $z_p = 1.575$. This seems to be a coincidence.

2.6.5 Summary of the contamination results

The contamination results summarised in Tables 2.2 and 2.3 allow comparison between the data sets described above as well as between the two analyses. We see that there is no significant differences in the two analyses. There is virtually no change to any of our quoted contaminations at $z_s < 0.3$ or $z_s < 0.6$ and if anything the numbers get slightly higher for the $z_{low} \geq 1.0$ and $z_{up} \leq 2.2$ QSO sample.

We conclude that for spectroscopic redshift $z_s < 0.3$ our DR1 sample has an $\approx 2\%$ contamination, in both cases. This comes from the fact that 1/3 of our sample which is in 2QZ has contamination 0.6% for $1 < z_p < 2.2$ (0.5% for $z_{low} \geq 1.0$ and $z_{up} \leq 2.2$) the rest has $4.1 \pm 1.8\%$ ($4.5 \pm 2.2\%$) as found from the comparison with the four AAOmega fields. Weighting by the relative size of the 2QZ and non-2QZ components of the DR1 QSO sample, this gives an estimate of $1.8 \pm 0.6\%$ for the $z_s < 0.3$ contamination, both for $1 < z_p < 2.2$ and $z_{low} \geq 1.0$ and $z_{up} \leq 2.2$. The error here is dominated by the AAOmega estimate of the non-2QZ DR1 contamination. However, we note that the 2QZ+SDSS contamination is higher ($0.9 \pm 0.1\%$, $0.8 \pm 0.1\%$) than the 2QZ contamination ($0.6 \pm 0.2\%$, $0.5 \pm 0.2\%$) and that the COSMOS estimate of overall contamination is also higher so we believe our estimate of $1.8 \pm 0.6\%$ for $z_s < 0.3$ contamination is reasonable.

The DR1 $z_s < 0.6$ contamination, which is more appropriate for $r < 21$ selected galaxies, is similarly estimated to be $(2/3 \times 3.6 + 1/3 \times 4.9) = 4.0 \pm 0.7\%$ and $5.2 \pm 0.9\%$ for $1 < z_p < 2.2$ and $z_{low} \geq 1.0$ and $z_{up} \leq 2.2$, respectively (see Tables 2.2 and 2.3). The overall contamination for $z_s < 1$ is estimated to be $(2/3 \times 8.3 + 1/3 \times 10.6 =)$ $9.1 \pm 0.6\%$ for $1 < z_p < 2.2$ and $8.4 \pm 0.7\%$ for $z_{low} \geq 1.0$ and $z_{up} \leq 2.2$. This can be compared to the low-redshift contamination rate of 7.3% (A.D. Myers , priv. comm) indicated by Fig. 2 of Myers et al. (2007). These contamination fractions also apply approximately to the QSO-photo-z sample of Scranton et al. since it appears to have similar contamination rates to the DR1 sample used here. In the next Chapter we shall see how this contamination level can change the lensing signal.

Table 2.1: Contamination. DR1 vs. 2QZ

object ID	$1.0 \leq z_p \leq 2.2$, $z_s \leq 1.0$	$1.0 \leq z_p \leq 2.2$
QSOs '11'	144	1999
NELGs	25	25
Stars '11'	55	55
Total number	224	2079
Contamination=	$169/2024 = (8.3 \pm 0.6)\%$	

Table 2.2: Contamination level in the SDSS photometric QSO sample of $1.0 < z_p < 2.2$

$1.0 \leq z_p \leq 2.2$	$z_s < 1.0$	$z_s < 0.6$	$z_s < 0.3$
2QZ set	$8.3 \pm 0.6\%$	$3.6 \pm 0.4\%$	$0.6 \pm 0.2\%$
2QZ+SDSS	$7.7 \pm 0.2\%$	$3.8 \pm 0.2\%$	$0.9 \pm 0.1\%$
COSMOS	$9.7 \pm 5.6\%$	$3.2 \pm 3.2\%$	$3.2 \pm 3.2\%$
AAOmega fields	$10.6 \pm 2.9\%$	$4.9 \pm 2.0\%$	$4.1 \pm 1.8\%$
Total	$\frac{2}{3}8.3\% + \frac{1}{3}10.6\%$	$\frac{2}{3}3.6\% + \frac{1}{3}4.9\%$	$\frac{2}{3}0.6\% + \frac{1}{3}4.1\%$
cont.=	$9.1 \pm 0.6\%$	$4.0 \pm 0.7\%$	$=1.8 \pm 0.6\%$

Table 2.3: Contamination level in the SDSS photometric QSO sample of $z_{low} \geq 1.0$ and $z_{up} \leq 2.2$

$z_{low} \geq 1.0$ and $z_{up} \leq 2.2$	$z_s < 1.0$	$z_s < 0.6$	$z_s < 0.3$
2QZ set	$7.5 \pm 0.7\%$	$4.4 \pm 0.5\%$	$0.5 \pm 0.2\%$
2QZ+SDSS	$7.2 \pm 0.3\%$	$4.1 \pm 0.2\%$	$0.8 \pm 0.1\%$
COSMOS	$9.1 \pm 6.4\%$	$4.5 \pm 4.5\%$	$4.5 \pm 4.5\%$
AAOmega fields	$10.2 \pm 2.5\%$	$6.7 \pm 2.8\%$	$4.5 \pm 2.2\%$
Total	$\frac{2}{3}7.5\% + \frac{1}{3}10.2\%$	$\frac{2}{3}4.4\% + \frac{1}{3}6.7\%$	$\frac{2}{3}0.5\% + \frac{1}{3}4.5\%$
cont.=	$8.4 \pm 0.7\%$	$5.2 \pm 0.9\%$	$=1.8 \pm 0.6\%$

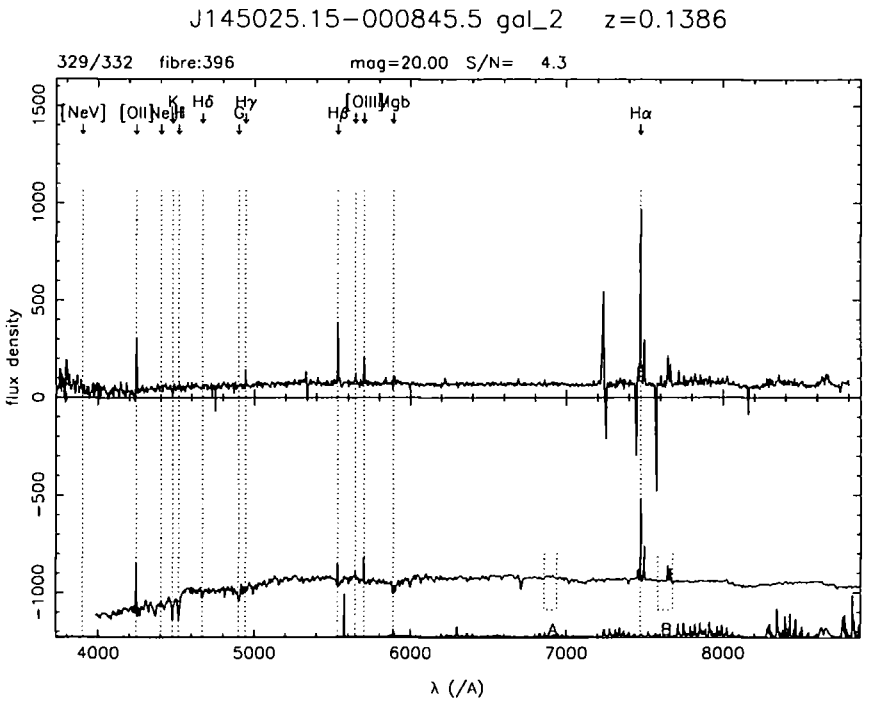

Figure 2.5: The contaminant in the e04 field. This object is a galaxy with $z_s = 0.1386$. Instead in the SDSS data set is a QSO with $z_p = 1.575$.

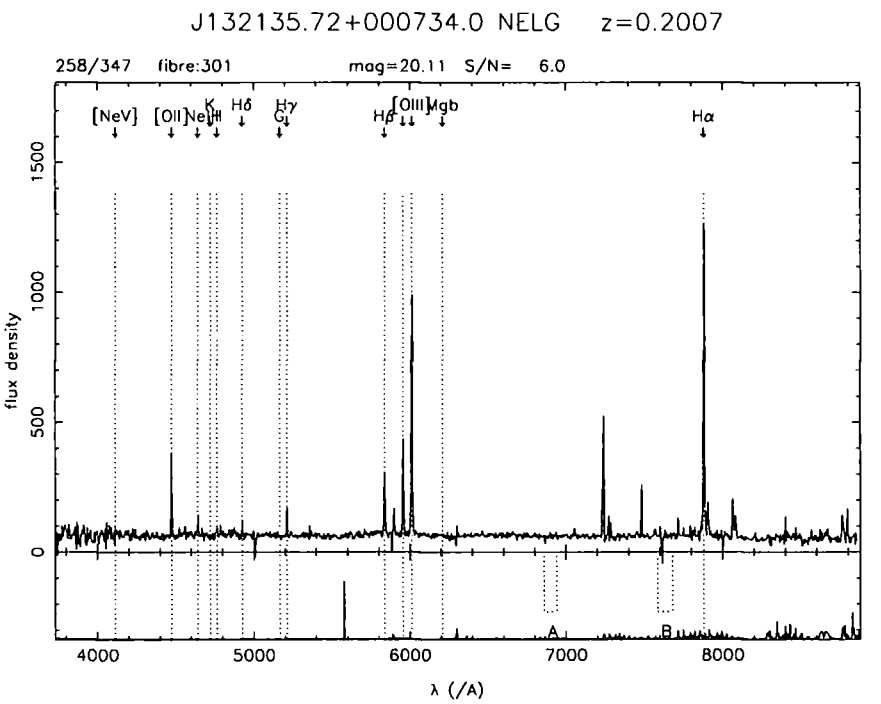

Figure 2.6: The contaminant in the d05 field. This object is an NELG with $z_s = 0.2007$. Instead in the SDSS data set is a QSO with $z_p = 1.175$.

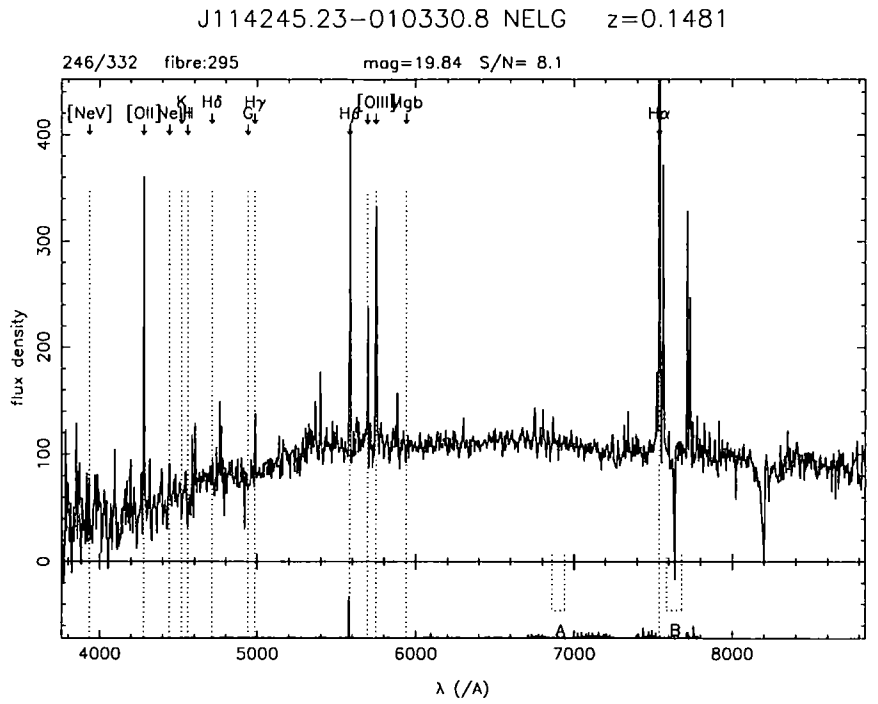

Figure 2.7: The contaminant in the S11 field. This object is an NELG with $z_s = 0.1481$. Instead in the SDSS data set is a QSO with $z_p = 1.525$.

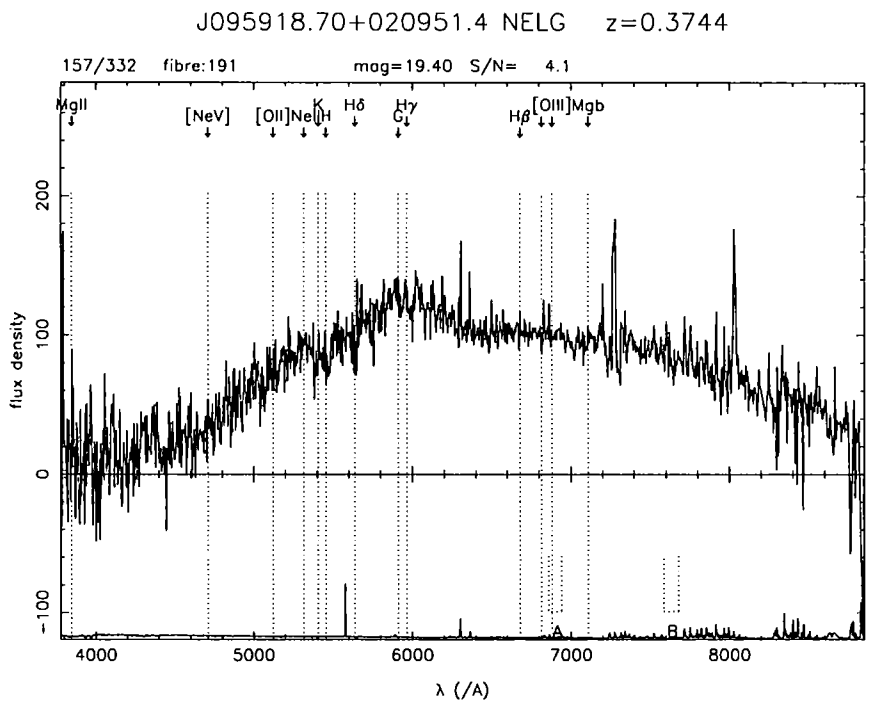

Figure 2.8: A contaminant in the COSMOS field. This object is an NELG with $z_s = 0.3744$. Instead in the SDSS data set is a QSO with $z_p = 1.325$.

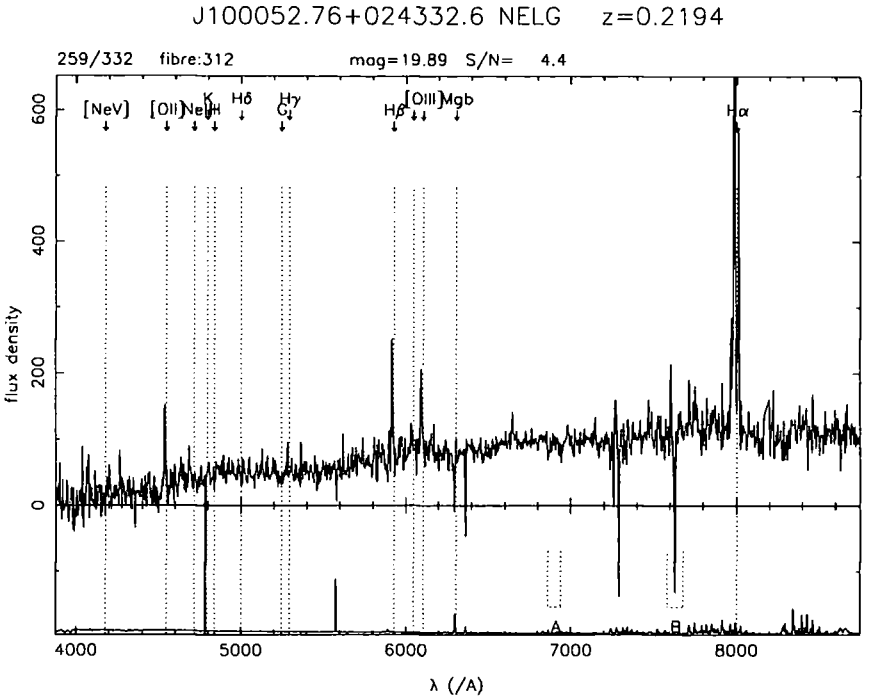

Figure 2.9: A contaminant in the COSMOS field. This object is an NELG with $z_s = 0.2194$. Instead in the SDSS data set is a QSO with $z_p = 1.575$. The specific object is also in Prescott et al. (2006) spectroscopic sample but it is identified as a QSO at redshift $z_c = 1.1616$.

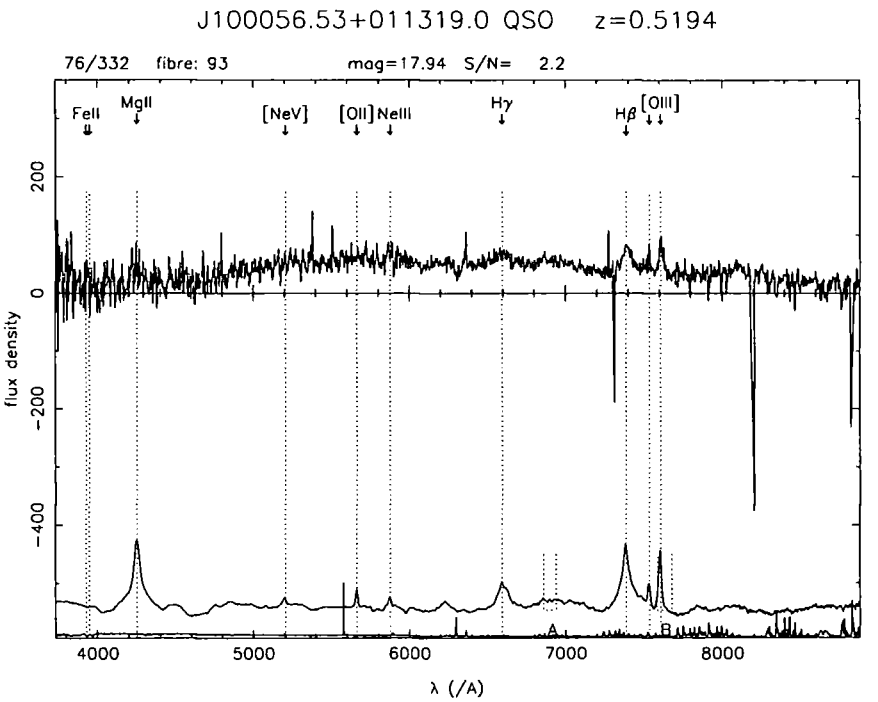

Figure 2.10: A contaminant in the COSMOS field. This object is a QSO with $z_s = 0.5194$. Instead in the SDSS data set is a QSO with $z_p = 1.575$.

Chapter 3

QSO Lensing Magnification: A Comparison of 2QZ and SDSS Results

3.1 Introduction

Large concentrations of mass at low redshift such as galaxies and groups of galaxies can gravitationally lens background objects such as galaxies, QSOs, supernovae and the cosmic microwave background. As discussed in Chapter 1, this phenomenon affects these background sources in two ways. It magnifies and distorts them. This systematic distortion is called cosmic shear (see e.g. Mellier and Meylan 2005 for a review) and the magnification cosmic magnification (Wu 1994, Broadhurst et al. 1995). In turn cosmic magnification has also two effects named the solid angle and amplification effect (Section 1.5.4). These two competing effects are responsible for the different results expected for different magnitude QSO samples. So for bright QSO samples with a steep number count slope the amplification effect dominates and we expect a positive cross-correlation with foreground galaxies whereas for faint samples with a flatter count slope we expect a negative cross-correlation signal. Intermediate QSO samples give a null result. For example, Boyle et al. (1988) found significant anti-correlation on scales of $4'$ around galaxies using faint QSOs ($B < 20.9$). Williams and Irwin (1998) and Nollenberg and Williams (2005) found

significant positive correlation on angular scales of the order of one degree (their QSO samples respectively consisted of QSOs within $16 < m_B < 18.5$ and $13 < B < 17.5$) and Gaztanaga (2003) measured the cross-correlation between photometric galaxies and bright, $i < 18.8$ spectroscopic QSOs using only the SDSS EDR and found a positive cross-correlation of 20% on arcminute scales.

Although the idea seems simple, QSO-galaxy cross-correlations have been a controversial subject over the years as different results and different strength of the signal are detected even when the same or similar QSO magnitude samples have been used. In this Chapter we are looking for a possible explanation of the apparent discrepancy between the results of Scranton et al. (2005) and Myers et al. (2003, 2005) where in the latter paper they seem to find a much stronger anti-correlation signal at the same ($g < 21$) QSO magnitude limit. In particular, we shall look for the effects of low redshift contamination in the photo-z QSO sample and also measure the QSO-galaxy cross-correlation at the same QSO and galaxy limits as used by Myers et al. (2003, 2005). We shall also be looking at the important effect of the $g < 21$ galaxy magnitude limit used by Myers et al. (2003, 2005) as opposed to the $r < 21$ limit used by Scranton et al. (2005).

In Section 3.2 we explain the data that we use and how they differ from Scranton et al. and Myers et al. (2005) data sets. We also provide details of our analysis. In Section 3.3 we present our results from QSO-galaxy cross-correlation and in Section 3.4 the results of cross-correlating the same QSOs with galaxy groups. In Section 3.5 we check the effect of the contamination (see Chapter 2) of the photometric QSO sample that we (and Scranton et al.) use on the results. In Section 3.6 we include the effect of the galaxy samples on our cross-correlation measurements. In Sections 3.7 and 3.8 we use fitting models for the cross-correlations with galaxies and clusters from Myers et al. (2003 and 2005) and Scranton et al. and compare them with our results. Finally, in Section 3.9 we discuss the conclusions that can be drawn as to the reason that causes the difference in the results in the three published papers.

3.2 The Data and Analysis

Our galaxy sample consists of SDSS DR4 galaxies at the magnitude limit of $g \leq 21$ where the sky density is $\simeq 1200 deg^{-2}$. It should be noted at the outset that our galaxy sample and that of Myers et al. (2005) is different from that of Scranton et al., as they use galaxies with $r < 21$ with a sky density of $\simeq 3500 deg^{-2}$. This means that care must be taken in comparing these results because the projected galaxy clustering in the $r < 21$ sample will have $\approx 2\times$ lower correlation function amplitude due to its increased depth. The QSO sample we use is the same sample which is extracted by Richards et al. (2004), by applying their 'Kernel Density Estimation' method on the DR1 dataset. Scranton et al. use a similar method to extract their QSO sample but they apply it to the DR3 set instead. We also use the same redshift range as Scranton et al. which is $1.0 < z_p < 2.2$. So the main difference between the QSO sample we use for our analysis and Scranton et al. use for theirs should be a larger number of QSOs in their sample (DR3 vs. DR1).

In total we have 37,876 QSOs in the above redshift range and 1,599,159 galaxies. The numbers for each area separately as well as the galaxy density ($g < 21$) are shown in Table 1. Our random catalogue consists of 7 times the number of the galaxies. All 'holes' found in SDSS data have been added to our random catalogues so the numbers shown above are our final number of objects. Fig. 3.1 shows the distribution of the QSOs that comprise our sample. The indicated areas 1-5 are those that were used for our cross-correlation analysis. In terms of our analyses of the SDSS photo-z QSO samples, we accept that these may be less sophisticated than those of Scranton et al. For example, we do not mask out poor seeing or high reddening areas and we use the standard SDSS star-galaxy classifier rather than Bayesian star-galaxy separation parameters. We believe that our $g < 21$ QSO limit is conservative enough to make these differences cause negligible effects. More importantly, we ignore the statistical ranges allowed for QSO photo-z, z_p, generally taking a sharp cut with $1 < z_p < 2.2$. Scranton et al. also weight their cross-correlation by the QSO photo-z probability. We shall flag the points where these different approaches may affect our conclusions.

The 2QZ QSOs are taken from the 2QZ catalogue (Croom et al. 2004). The

Table 3.1: Number of $g < 21$ DR1 QSOs, $g < 21$ galaxies and the QSO and galaxy density for each area separately

area	1	2	3	4	5
QSOs	5,373	10,380	5,720	15,225	1,178
Galaxies	203,164	455,541	216,204	679,200	45,050
QSOs $\deg^{-2}$	34.5	31.6	31.8	29.2	30.2
Galaxies $\deg^{-2}$	1302	1386	1202	1303	1155

2QZ comprises two $5deg \times 75deg$ declination strips, one in an equatorial region in the North Galactic Cap (NGC) and one at the South Galactic Cap (SGC). In our analysis when we mention the 2QZ area or 2QZ QSOs we mean only the NGC of the 2dF QSO survey, unless we present results from Myers et al. (2005) in which case the cross-correlation has been done in both the NGC and SGC. We should underline here that the most important difference between the 2QZ and the DR1 QSO dataset that we use or the DR3 that Scranton et al. use is that 2QZ QSOs are spectroscopically confirmed whereas the method used to extract the DR1/DR3 QSOs is based on Bayesian photometric classification and the redshifts assigned to the objects are photometric redshifts.

Throughout our analysis we centre on QSOs and count galaxies or clusters for our cross-correlations so our random catalogues are constructed with the same angular selection function as our galaxy samples. To measure the two-point correlation function $\omega(\theta)$, we use the equation 1.44. Our errors are field-to-field errors. In this case we divide our data sets into 25 subsamples and measure the field-to-field variations of the cross-correlation function. The error is then estimated using the equation 1.48.

Since 2QZ QSOs had higher priority than 2dFGRS galaxies for spectroscopic observations there is no issue for fibre incompleteness to deal with. Of course, this is also true for the photo-z sample. On the smallest scales there is a lower limit for cross-correlation of $10''$ due to confusion caused by galaxy overlaps.

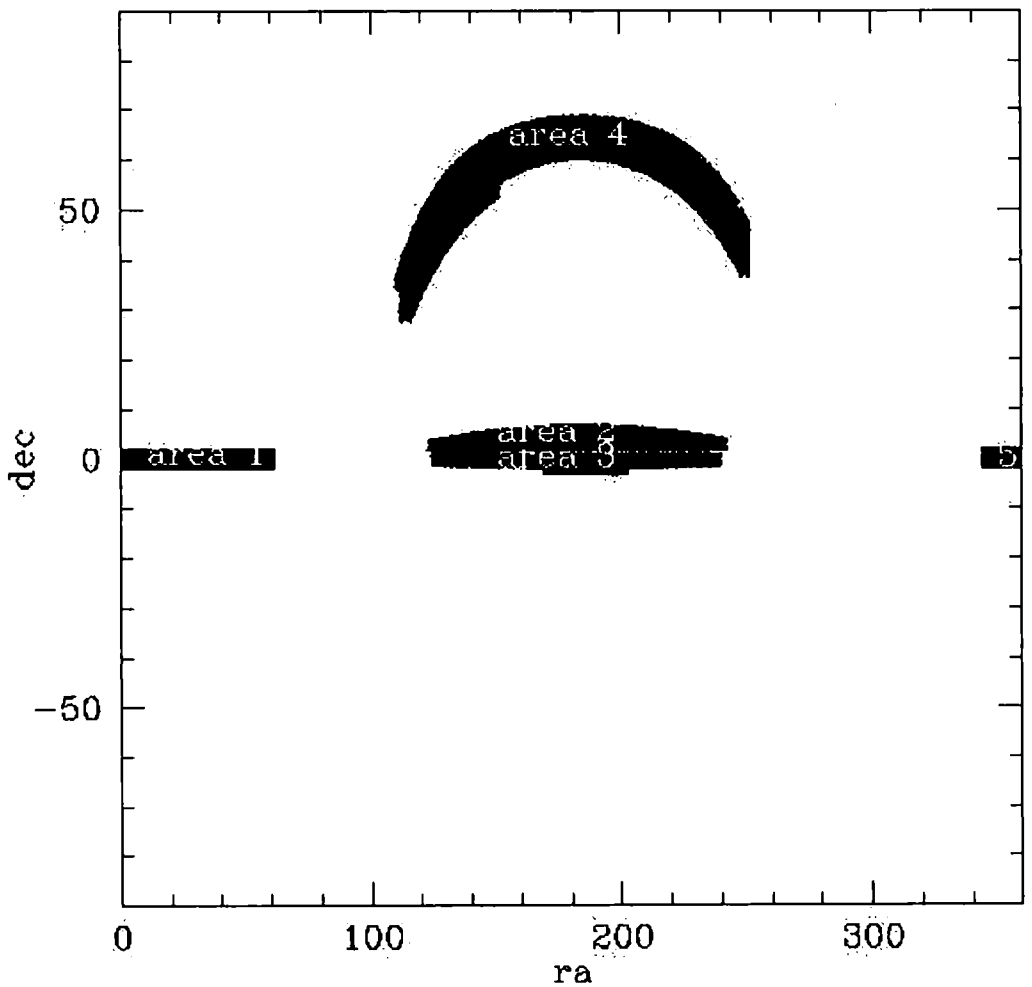

Figure 3.1: The distribution of our DR1 QSO and galaxy samples. The numbers indicate the areas in which the samples were cross-correlated. Area 3 is the 2QZ area.

3.3 QSO-galaxy cross-correlation results

We first cross-correlate our SDSS DR1 photo-z $g < 21$ QSO sample with our SDSS DR4 $g < 21$ galaxy sample. The results are shown in Fig. 3.2 by the black filled circles. For comparison the NGC results from Myers et al. (2005) have also been added (triangles) without their errorbars and for reference the results from Scranton et al. (squares) also without their errorbars. The results from Scranton et al. are taken from their faintest QSO sample $20.5 < g < 21$, cross-correlated with $r < 21$ galaxies. From this plot it seems that our results are slightly higher than those of Myers et al. (2005) throughout most of the range of scales. The Scranton et al. results have a smaller anti-correlation signal as expected due to the different galaxy sample they use (Section 3.6).

We have also included the results when we cross-correlate 2QZ QSOs with the same galaxy sample ($g < 21$) in the 2QZ NGC area. These results are shown by the open circles. This is 1.8 $\times$ bigger area than used by Myers et al. (2003, 2005) due to the smaller SDSS area previously available. Finally, asterisks show the results from cross-correlating our DR1 QSOs with the same galaxy sample in the 2QZ area. The 2QZ QSOs again tend to give more anti-correlation than the DR1 QSOs cross-correlated with the same galaxy sample.

Fig. 3.3 shows the same results as the previous plot but this time our DR1 QSO sample consists of 17,426 QSOs with magnitude $20.5 \leq g \leq 21.0$. The amplitude of the anticorrelation signal is similar to that found in Fig. 3.2 for $g < 21$ QSOs and again is stronger, as expected, than the signal detected by Scranton et al. for $r < 21$ galaxies, but consistent with Myers et al.

Fig. 3.4 shows the QSO-galaxy cross-correlation results for bright QSOs. Here our DR1 sample consists of $1.0 < z_p < 2.2$ QSOs in the magnitude range $17 \leq g \leq 19$, Scranton et al. (squares) where the QSOs have $17 \leq g \leq 19$ and the galaxies have $r < 21$. We have also plotted the results from Gaztanaga (2004) (triangles) where the specific data points are drawn from his QSO sample with $18.3 \leq i \leq 18.8$ and $0.8 \leq z \leq 2.5$ and their galaxy sample with $19 < r < 22$. We then show the results when we cross-correlate the 339 bright ($18.25 \leq g \leq 19.0$) 2QZ QSOs in the 2QZ NGC area (open circles). These results give zero signal and a bump appears on

scales from 4′-16′. This bump is consistent with the statistical noise as we can see from the field-to-field errorbars and moreover it disappears when we cross-correlate the same QSO sample with galaxies in groups (Section 3.4, Fig. 3.10). Our DR1 and 2QZ results seem consistent although the errors are large. Both results also appear lower than the results of Gaztanaga. The results are consistent with those of Scranton et al. although their galaxy sample is fainter. Summarising, our results for bright QSOs, from DR1 and 2QZ give, at least at small scales, a less positive cross-correlation than that seen by Gaztanaga but one consistent with that found by Scranton et al., although the S/N is poor. The interpretation of this latter result requires account to be taken of their fainter limit and the QSO count slope at $g \simeq 19$. We postpone further discussion to Sections 3.5 and 3.6 where the effects of contamination will also be discussed.

3.4 QSO-galaxies in groups cross-correlation results

The next step was to find groups of galaxies in the 5 areas of the DR4 dataset. Although there are no group results from Scranton et al. with which to compare, we can still compare the QSO photo-z and spectroscopic results, in a situation where the S/N of any lensing effect may be expected to be higher than for galaxies. We therefore use the same method that is described in Myers et al. (2003) and references therein to determine these groups. We use a factor δ by which we wish our group density to exceed the mean surface density of the area that is being examined. In our case we use $\delta = 8$. Then we draw a circle with the largest possible radius, such that our group density doesn't fall below δ times the mean surface density. Groups are defined when these circles overlap and the mean surface density does not fall below the critical value (friends-of-friends). From these groups we select for our cross-correlations the ones with at least 7 members in order to reduce the likelihood of chance alignments of galaxies at different redshifts being grouped together. An example of how the galaxies of these groups look is shown in Fig. 3.5. In total there are 14,143 groups with more than 7 members in the 5 areas that we use.

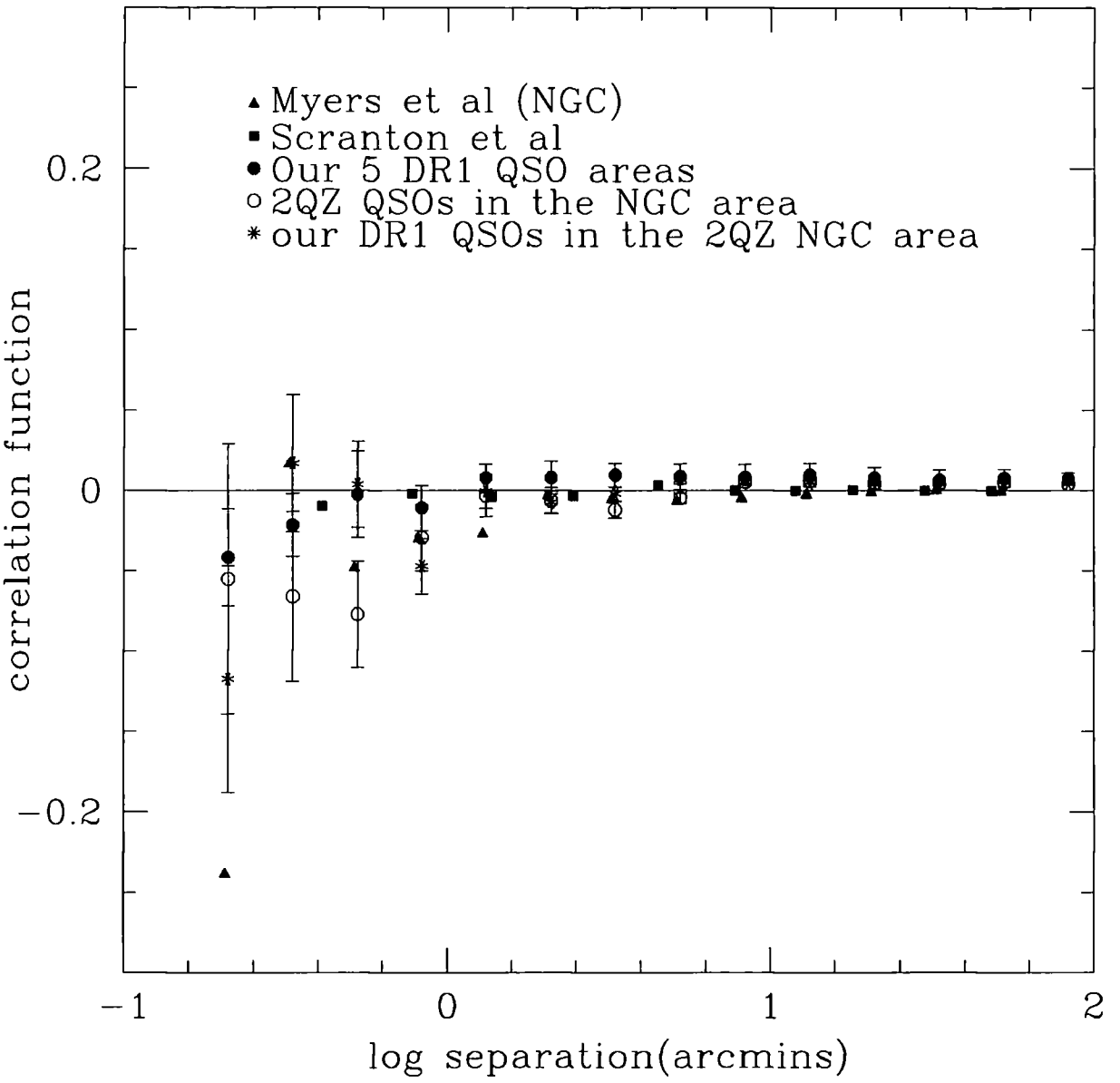

Figure 3.2: QSO-galaxy cross-correlation results. Our DR1 results are shown by the black filled circles and cover the whole magnitude range for the QSO sample ($g < 21$) and $g < 21$ for the galaxies. Triangles are the results from Myers et al. (2005) for the NGC of the 2QZ (centring on QSOs and counting galaxies). Squares show Scranton et al. where the faintest QSO sample has been used, $20.5 < g < 21$, and $r < 21$ for galaxies. We have also included our results by cross-correlating 2QZ QSOs with the same galaxy sample in the 2QZ area. These results are shown by the open circles. Asterisks show the results from cross-correlating our DR1 QSOs with the same galaxy sample in the 2QZ area. The errors are field-to-field errors.

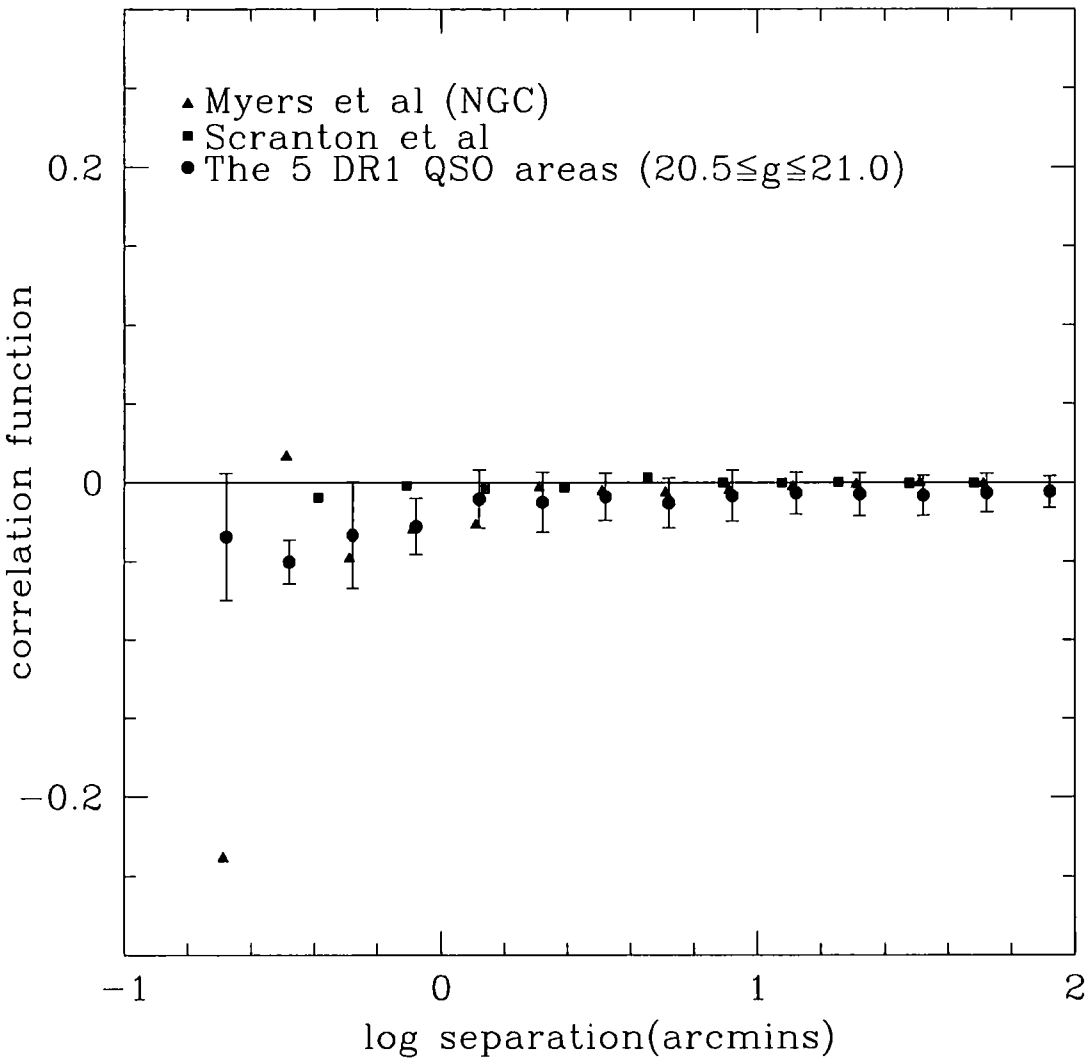

Figure 3.3: QSO-galaxy cross-correlation results. This time our DR1 QSO sample comprises of QSOs with $20.5 \leq g \leq 21.0$. The errors are field-to-field errors. Triangles are the results from Myers et al. (2005) and squares from Scranton et al.

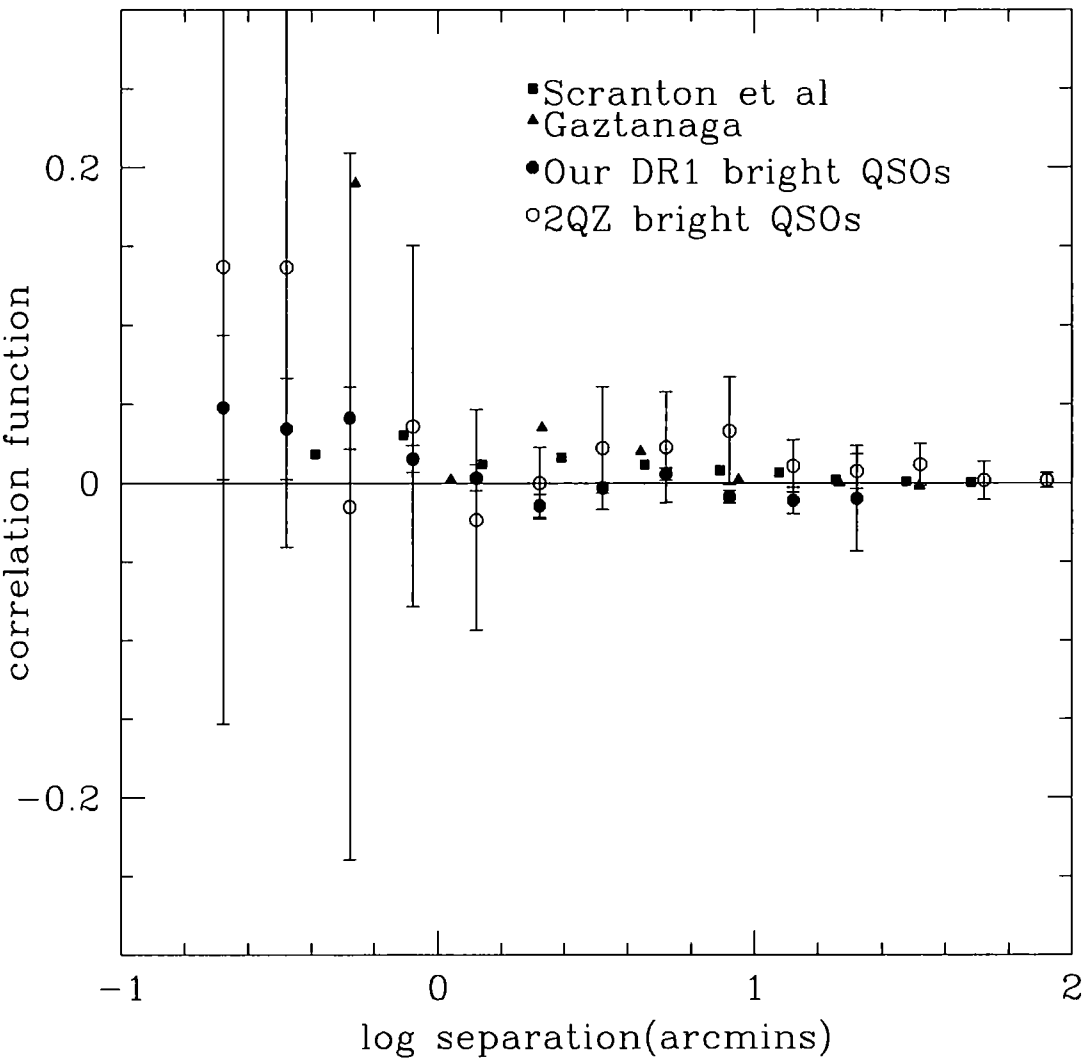

Figure 3.4: QSO-galaxy cross-correlation results for bright QSOs. Our DR1 QSO sample consists of QSOs with $17 \leq g \leq 19$ (black circles). The results of Scranton et al. for QSOs with $17 \leq g \leq 19$ and galaxies with $r < 21$ are also shown (squares). The triangles show the results from Gaztanaga (2004). His sample consists of QSOs with $18.3 \leq i \leq 18.8$ and $0.8 \leq z \leq 2.5$ and galaxies with $19 < r < 22$. Finally, we present the results from the 339 bright ($18.25 \leq b_j \leq 19.0$) 2QZ QSOs in the 2QZ area (open circles).

We next cross-correlated our DR1 QSO sample with galaxies that are in groups with at least 7 members. The signal detected in this case is usually stronger than the one in QSO-galaxy cross-correlations because groups have a bigger mass. In total our galaxy sample consists of 146,490 galaxies in groups. In Fig. 3.6 we show the results for each of the 5 areas separately. The errors are field-field errors. An anti-correlation effect is consistently seen in all 5 areas. The combined results for all the 5 areas are shown in Fig. 3.7. For comparison, the results from Myers et al. (2003) for both the NGC and SGC have been added (triangles). They use 22,417 2QZ QSOs and nearly 300,000 galaxies of limiting magnitude $b = 20.5$ found in groups of at least 7 members. From the comparison we see that their signal is stronger on scales of 0.4-2.5 arcmins, which is expected as the results from the SGC show a slightly stronger anti-correlation signal (Myers et al., 2003) and so they push the overall result down. Again, as for the QSO-galaxy results we show the results of the cross-correlation of 2QZ QSOs with the galaxies in clusters in the NGC of the 2QZ area. The results are shown by the open circles. Finally, asterisks show the results from our DR1 QSO cross-correlation with the same galaxy sample in the 2QZ area. The signal detected is at a lower level. From the plot we see that 2QZ QSOs give a stronger anti-correlation signal than the one detected by using our DR1 QSOs in the 2QZ area but statistically consistent with Myers et al. (2003). Fig. 3.8 shows the results, when we cross-correlate our QSO photo-z sample with galaxies in groups with 15 or more members (open circles). The results from QSO-galaxies in groups with more than 7 members have been added (filled circles) for comparison. We note that when the lens mass is double (15 galaxy members vs 7 galaxy members) the amplitude of the lensing signal doubles as well.

Previously we have cross-correlated individual group galaxies rather than the centre of groups. Fig. 3.9 shows the results from DR1 QSOs with centres of groups of galaxies with more than 7 members (filled circles). Open circles show the results from Myers et al. (2003) combined for both the NGC and the SGC together with a best fit model which will be briefly discussed in Section 3.8. Although these results are generally easier to compare directly with models, the signal-noise is weaker due to non-weighting by cluster membership. Again our DR1 results appear to show

less anti-correlation than the 2QZ results.

Fig. 3.10 also shows the results from cross-correlating our bright DR1 QSOs ($17.0 \leq g \leq 19.0$) with galaxies in clusters with more than 7 members (filled circles). Some positive signal at $1'$ is again seen, increased by about a factor of four from the QSO-galaxy case in Fig. 3.4.

However, the positive signal is still only at a marginally significant level. We shall argue later that the lack of a strong positive signal may be explained by being close to the knee of the QSO count slope where $\beta' \approx 0.4$ and only a small lensing effect might be expected.

Finally, we extracted the bright QSOs from the 2QZ sample ($18.25 \leq b_j \leq 19.0$, $1.0 \leq z \leq 2.2$) and cross-correlate them with galaxies in clusters (with more than 7 members). The results are shown by the open circles in Fig. 3.10 and seem to give a slightly positive signal but this result is again not statistically significant. Also, the bump that appeared in Fig. 3.4 when we cross-correlated the same QSO sample with galaxies has disappeared.

3.5 Effects of the contamination in the QSO sample

In this Section we present two ways to correct our cross-correlation results for the contamination in our photometric QSO sample.

3.5.1 Effects of $\simeq 2\%$ contamination on the DR1 QSO-galaxy results

Based on the contamination level of our SDSS DR1 QSO sample, as estimated in the previous Chapter, we shall see how an $\approx 2\%$ contamination for $z \leq 0.3$ can alter our cross-correlation results in the case of QSO-galaxy and QSO-cluster cross-correlations. We will first base our calculations on the galaxy-galaxy autocorrelation results at $g \leq 21.0$ represented by $w = 0.33\theta^{-0.8}$ with θ in arcmins (see Fig. 8 of Myers et al). We multiplied this $g < 21$ galaxy $w(\theta)$ by the $z < 0.3$ 1.8% contamination

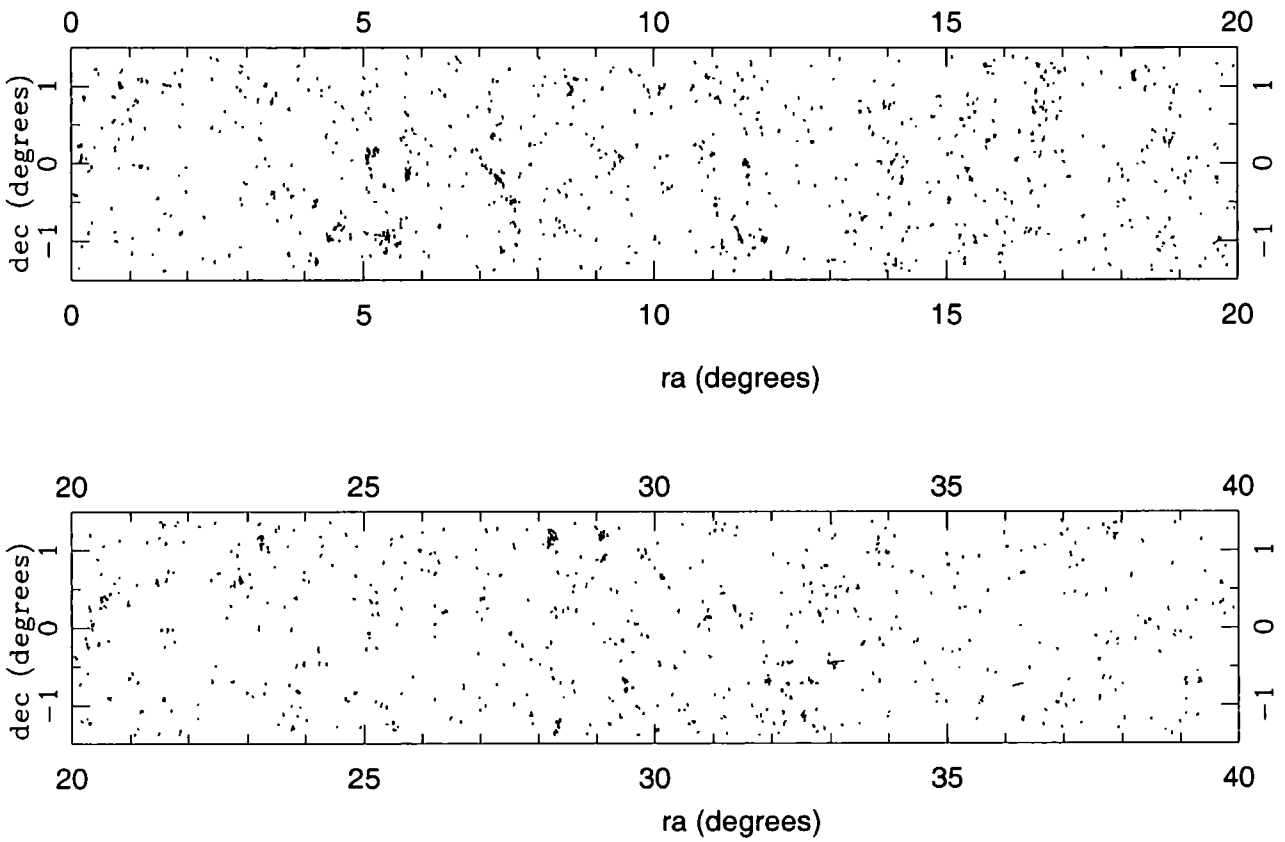

Figure 3.5: Galaxies ($g < 21$) in groups with more than 7 members in the strip between $-1.5 < \delta < +1.5$deg and 0h$< \alpha <$2h40 in Area 1.

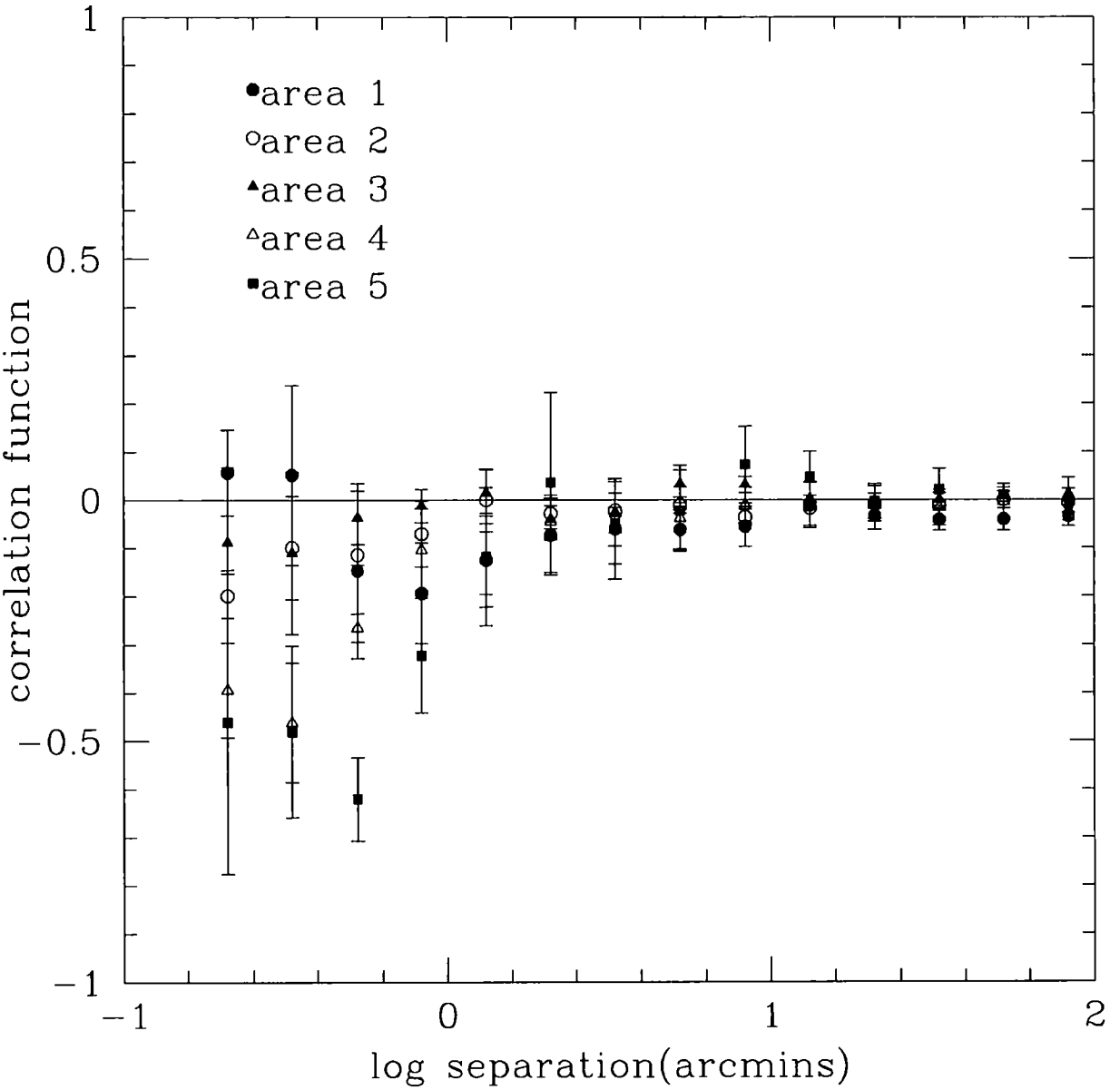

Figure 3.6: The DR1 QSO - DR4 galaxies in groups cross-correlation results for each area separately. The errors are field-field errors.

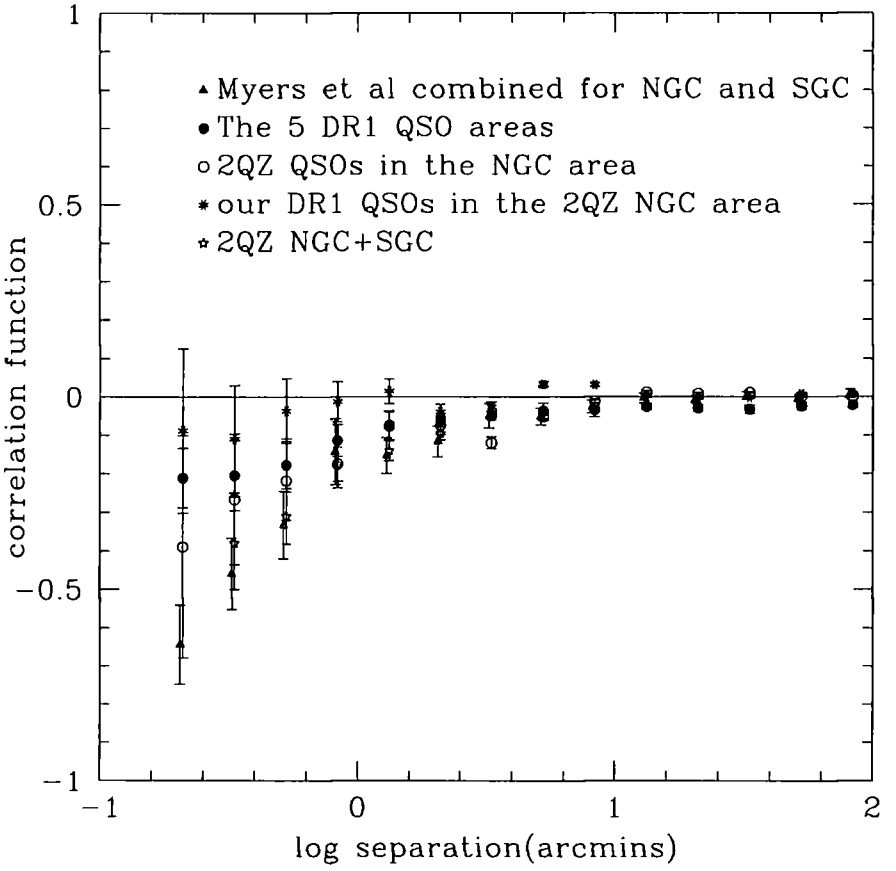

Figure 3.7: Cross-correlation between QSOs and galaxies in groups of galaxies with at least 7 members (filled circles). The errors are field-to-field errors. The triangles show the combined results from Myers et al. (2003) for both the NGC and SGC. They use 22,417 2QZ QSOs and nearly 300,000 galaxies of limiting magnitude $b = 20.5$ found in groups of at least 7 members. Their cross-correlation is done in the SGC and NGC strip of the 2QZ. From the comparison we see that their signal is stronger on scales of 0.4-2.5 arcmins. We also show the results of the cross-correlation of 2QZ QSOs with the galaxies in clusters in the 2QZ area. The results are shown by the open circles and give a weaker anti-correlation signal than found in the results of Myers et al. but still the signal is stronger than the one detected by using our DR1 QSO sample. Asterisks show the results from our DR1 QSOs cross-correlation with the same galaxy sample in the 2QZ area. Stars show the results when we average our open circles from the NGC of 2QZ with Myers et al. results for the SGC.

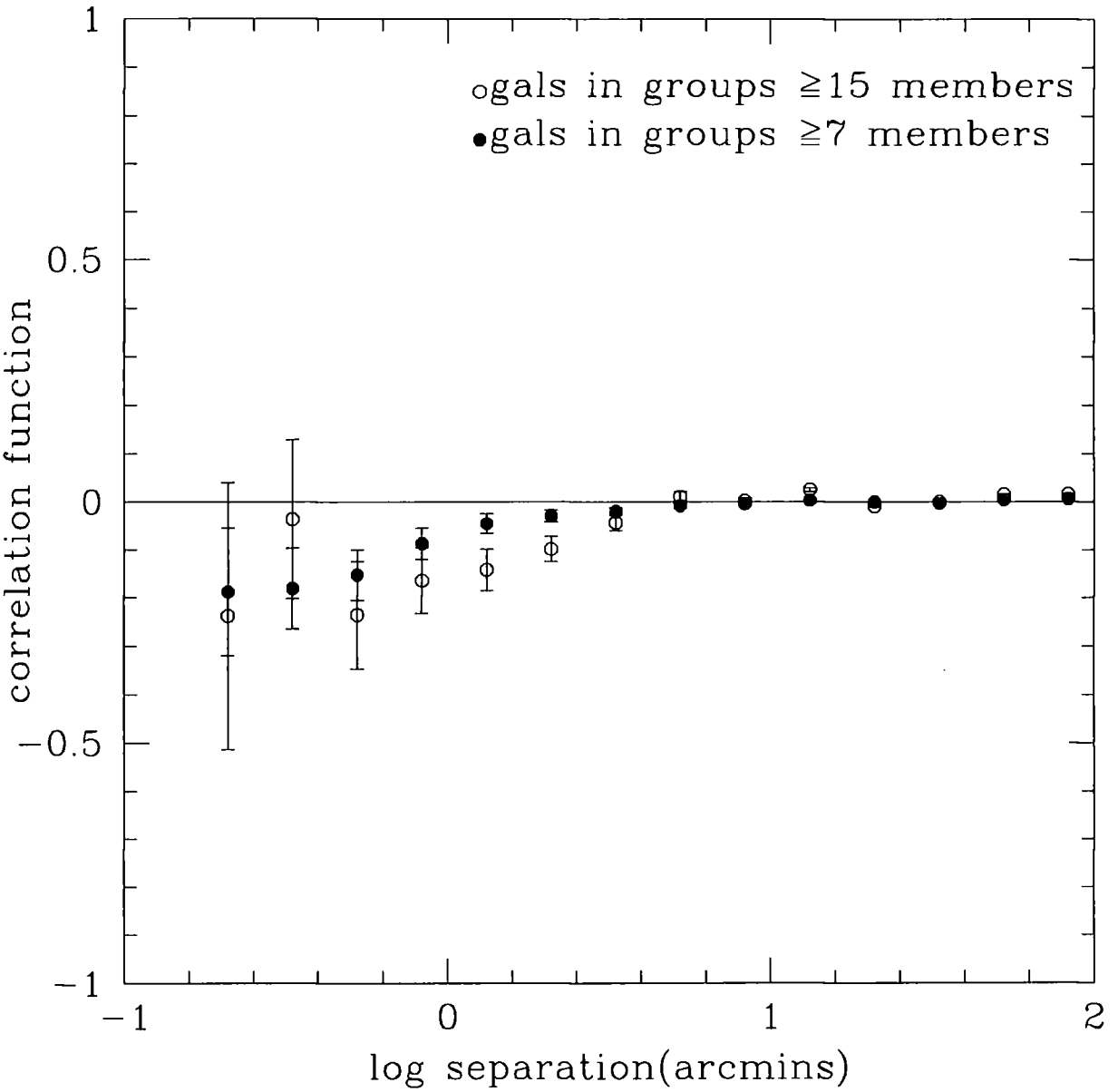

Figure 3.8: Cross-correlation results of QSO-galaxies in groups with more than 15 members (open circles) are compared to cross-correlation results of QSO-galaxies in groups with more than 7 members (filled circles). When the lens mass gets double the lensing signal doubles, as well.

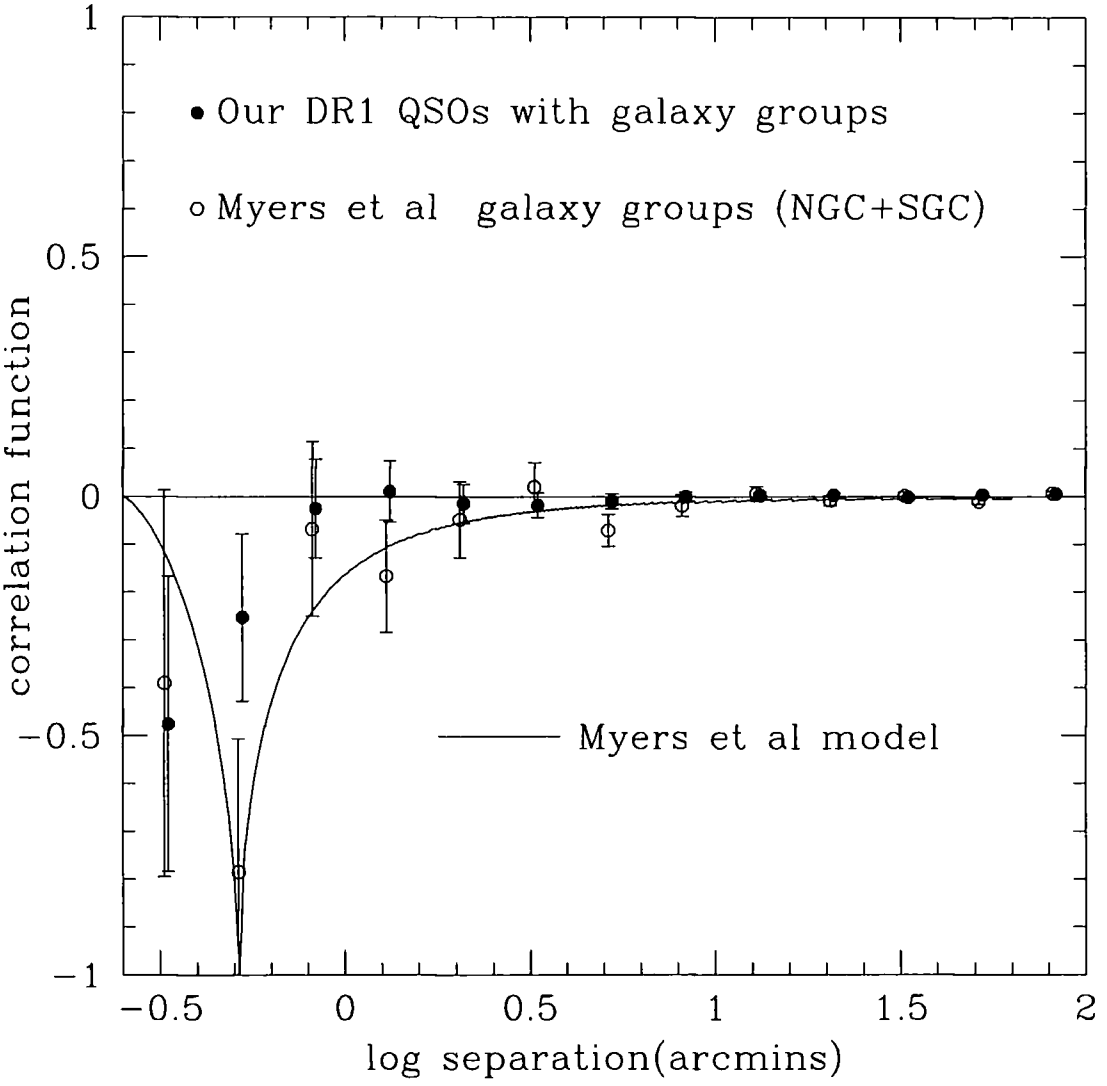

Figure 3.9: Cross-correlation between DR1 QSOs in 5 areas and centres of groups of galaxies with at least 7 members, assuming $\delta = 8$. Open circles show the results from Myers et al. (2003) combined for both the NGC and the SGC together with a best fit model which will be briefly discussed in Section 3.8. Our signal here is less strong due to non-weighting by cluster membership.

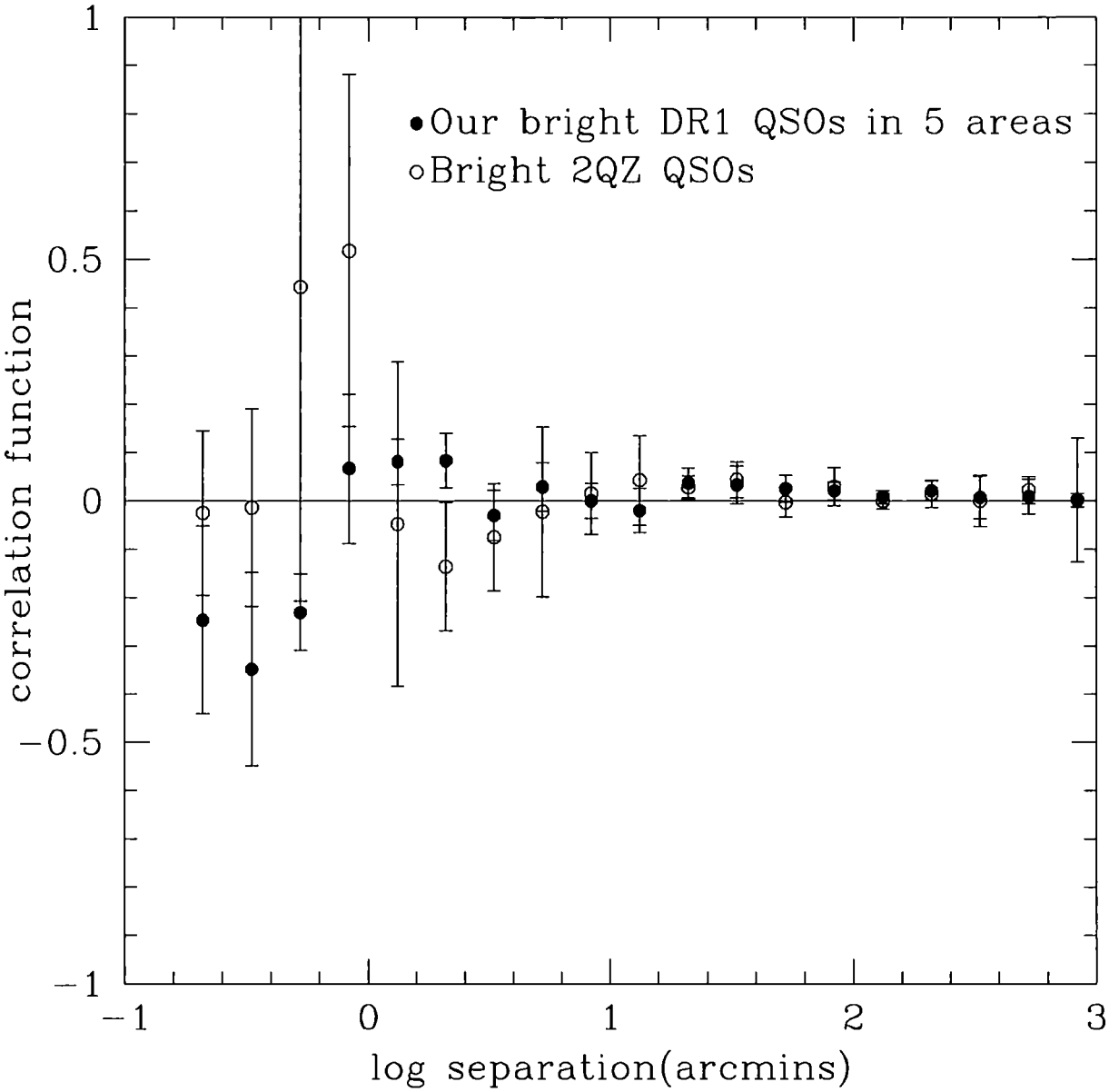

Figure 3.10: Bright 2QZ QSOs ($18.25 \leq b_j \leq 19.0$, $1.0 \leq z \leq 2.2$) cross-correlated with galaxies in clusters with at least 7 members (open circles) give a slightly stronger positive signal but still insignificant. Also, the bump has disappeared which suggests that it was due to statistics. Filled circles show the results for our bright DR1 QSOs ($17.0 \leq g \leq 19.0$) cross-correlated with galaxies in clusters with at least 7 members in the 5 areas. A signal is marginally detected at $1'$.

estimate, and then subtracted this correction from the SDSS photo-z galaxy-QSO cross-correlation results, assuming that the product of the two correlation functions is negligible (see Geller et al. 1984). Thus, at 1′ this correction is -0.007 and at the smallest bin $\theta = 0'.2$ the correction only rises to -0.02.

Assuming this correction, our previous Fig. 3.2 now appears as seen in Fig. 3.11. In this plot our DR1 QSO results in the 5 areas (filled circles) have been changed assuming 1.8% contamination and remain statistically consistent with the 2QZ QSO results (open circles). The agreement improves but only slightly. Also, the results using our DR1 QSO sample in the 2QZ area (asterisks) have been changed using the same corrections and they remain statistically consistent with the 2QZ QSO and our DR1 QSO results.

Finally, we have corrected the Scranton et al. results (squares) assuming contamination of 4% and the fit to the $r < 21$ galaxy autocorrelation function shown in Fig. 3.16. At 1′ this correction is -0.006 and at the smallest bin $\theta = 0'.3$ the correction rises to -0.01. The anti-correlation at $\theta = 0'.3$ increased by a factor of $\simeq 2$.

We have also corrected the results for the bright photo-z QSOs samples that appear in Fig. 3.4. The corrected results are shown in Fig. 3.12 assuming 1.8% contamination. These results show some positive signal but only at marginally significant levels. The most significant result is from the $17 < g < 19$ QSO-galaxy result of Scranton et al. which after correction gives $w_{qg} = 0.024 \pm 0.018$ at 1′.

We now correct the QSO-cluster cross-correlations for contamination. Here we base the correction on the galaxy-cluster cross-correlation results of Stevenson et al. (1988) who used the same group detection parameters as we do here. They cross-correlate galaxies with groups of galaxies with > 7 and more than > 15 members down to $b_j = 20.2$ (see their Fig. 9). We use their results for clusters with more than 7 members which matches our cluster selection and we correct our results assuming as before 1.8% contamination of galaxies in our DR1 QSO sample. At 1′ this correction is -0.11 and at the smallest bin $\theta = 0'.3$ the correction rises to -0.12. The results are shown in Fig. 3.13. Applying the 1.8% contamination correction to our results increases the anti-correlation at 1′ by a factor $\simeq 3$ and improves

consistency with the Myers et al. (2003) model at all scales.

Summarising, the effects of contamination are low for the photo-z QSOs when cross-correlated with $g < 21$ galaxy samples. They can be more significant at small scales for photo-z QSOs cross-correlated with $r < 21$ galaxy samples.

3.5.2 Contamination correction estimated via low-z objects in the 2QZ catalogue

A different way to correct for the contamination in the cross-correlation results is to base our correction on a cross-correlation between all the low redshift ($z \leq 0.6$) objects that are in the 2QZ catalogue (QSOs, NELGs, LINERs, ...) with the foreground galaxies. We found 2,667 low-z objects in the NGC of the 2QZ and the cross-correlation results with $g < 21$ galaxies appear in Fig. 3.14. Note that this result has a much lower amplitude than the $g < 21$ galaxy autocorrelation results due to the bigger mis-match between the average redshift of the $g < 21$ and $z < 0.6$ 2QZ samples. For the $g < 21$ galaxy results this cross-correlation correction used is similarly small to the auto-correlation corrections discussed above and so we only focus on the correction for the $r < 21$ galaxies of Scranton et al. We again use the 4% $z < 0.6$ contamination correction appropriate for $g < 21$ QSOs cross-correlated with $r < 21$ galaxies. The results are shown in Fig. 3.15 alongside the uncorrected results and the observational model ($\omega_{qg(\theta)} = -0.024 \pm^{0.008}_{0.007} \theta^{-1.0\pm0.3}$) from Myers et al. (2005). At $1'$ the correction is -0.0028 and at $\theta = 0'.3$ the correction is -0.004. So at $1'$ the auto-correlation function route gives a $2\times$ lower correction than the cross-correlation route. Since the $r < 21$ cross-correlation has poorer signal to noise while the autocorrelation route has more uncertainty associated with the assumed $n(z)$ in what follows we shall be using the average of these two corrections for the QSO-galaxy cross-correlations of Scranton et al. The (average) corrected results are also shown in Fig. 3.15.

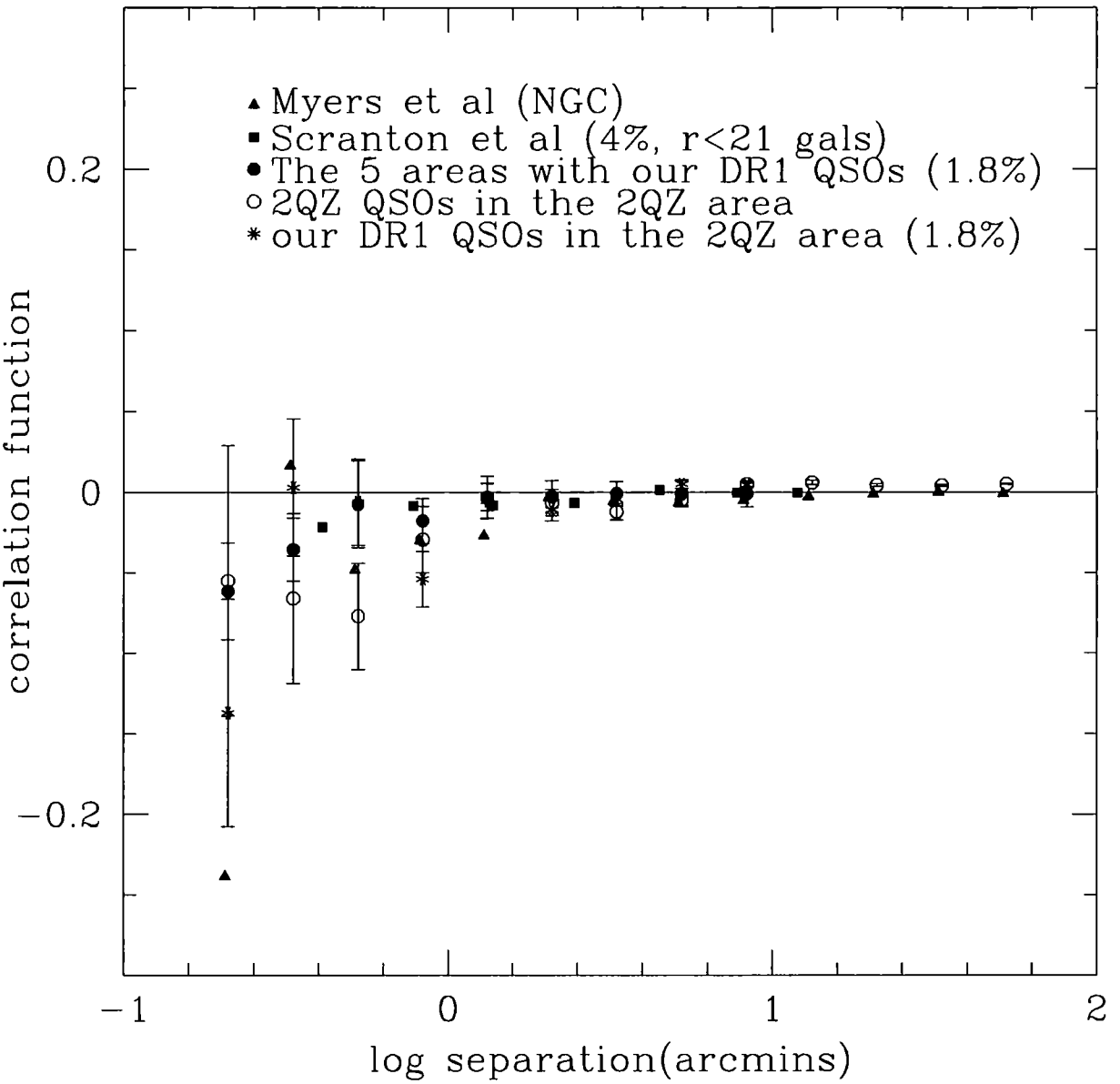

Figure 3.11: QSO-galaxy cross-correlation results as in Fig. 3.2 but our DR1 QSOs in the 5 areas (filled circles) and in the 2QZ area (asterisks) have been changed assuming contamination of 1.8% and the fit to $g < 21$ galaxy autocorrelation function shown in Fig. 3.16. Scranton et al. (squares) have also been changed assuming contamination of 4% and the fit to the $r < 21$ galaxy autocorrelation function (Fig. 3.16).

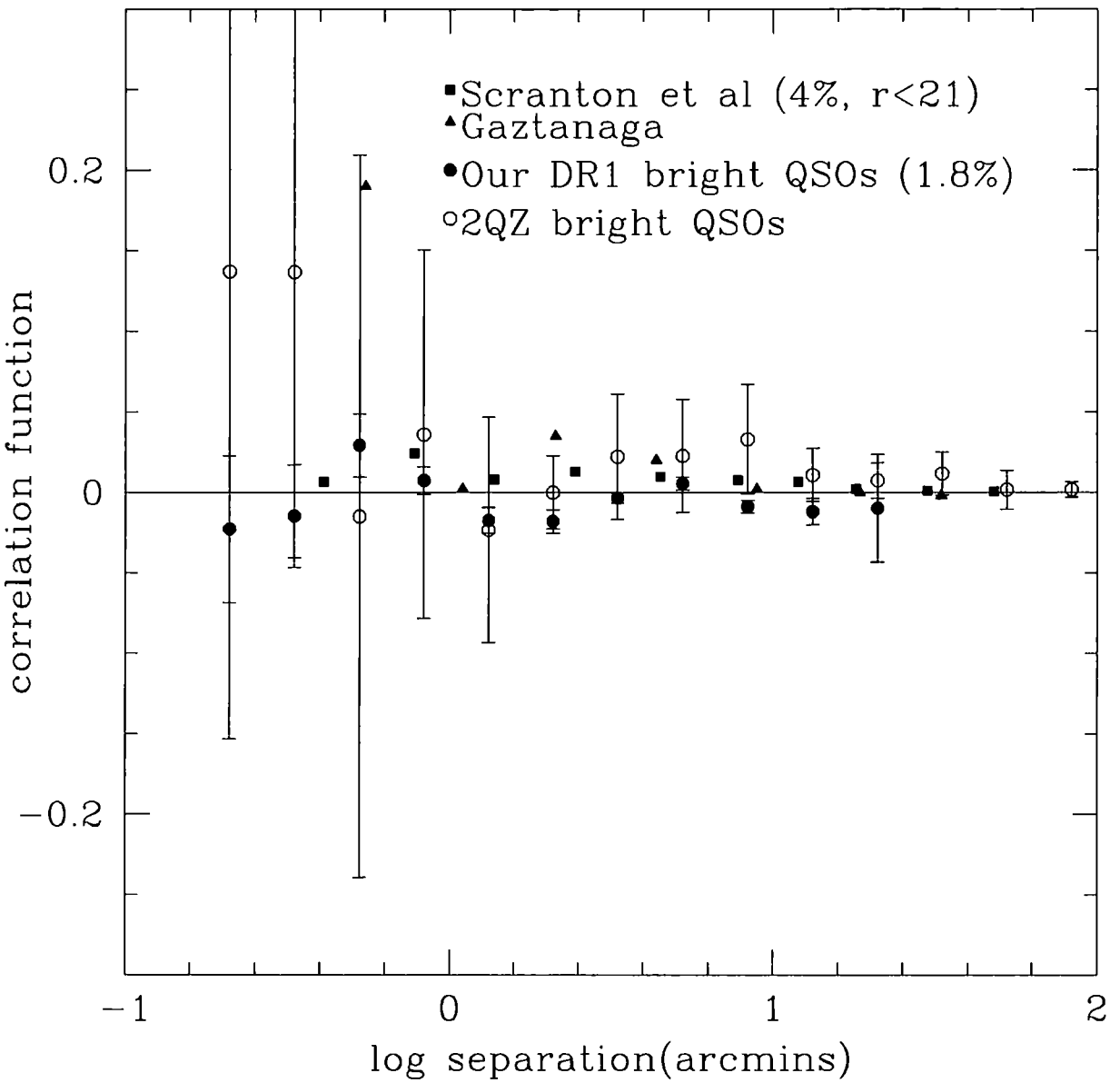

Figure 3.12: QSO-galaxy cross-correlation results for bright QSOs as in Fig. 3.4. Our DR1 QSO sample consists of QSOs with $17 \leq g \leq 19$ (filled circles) and is corrected assuming 1.8% contamination of the $g < 21$ galaxies, Scranton et al. (squares) is corrected assuming 4% contamination and the fit to the $r < 21$ galaxy autocorrelation function shown in Fig. 3.16. The triangles show the results from Gaztanaga (2004). His sample consists of QSOs with $18.3 \leq i \leq 18.8$ and $0.8 \leq z \leq 2.5$. Finally, we present the results from the 339 bright ($18.25 \leq b_j \leq 19.0$) 2QZ QSOs in the 2QZ area (open circles).

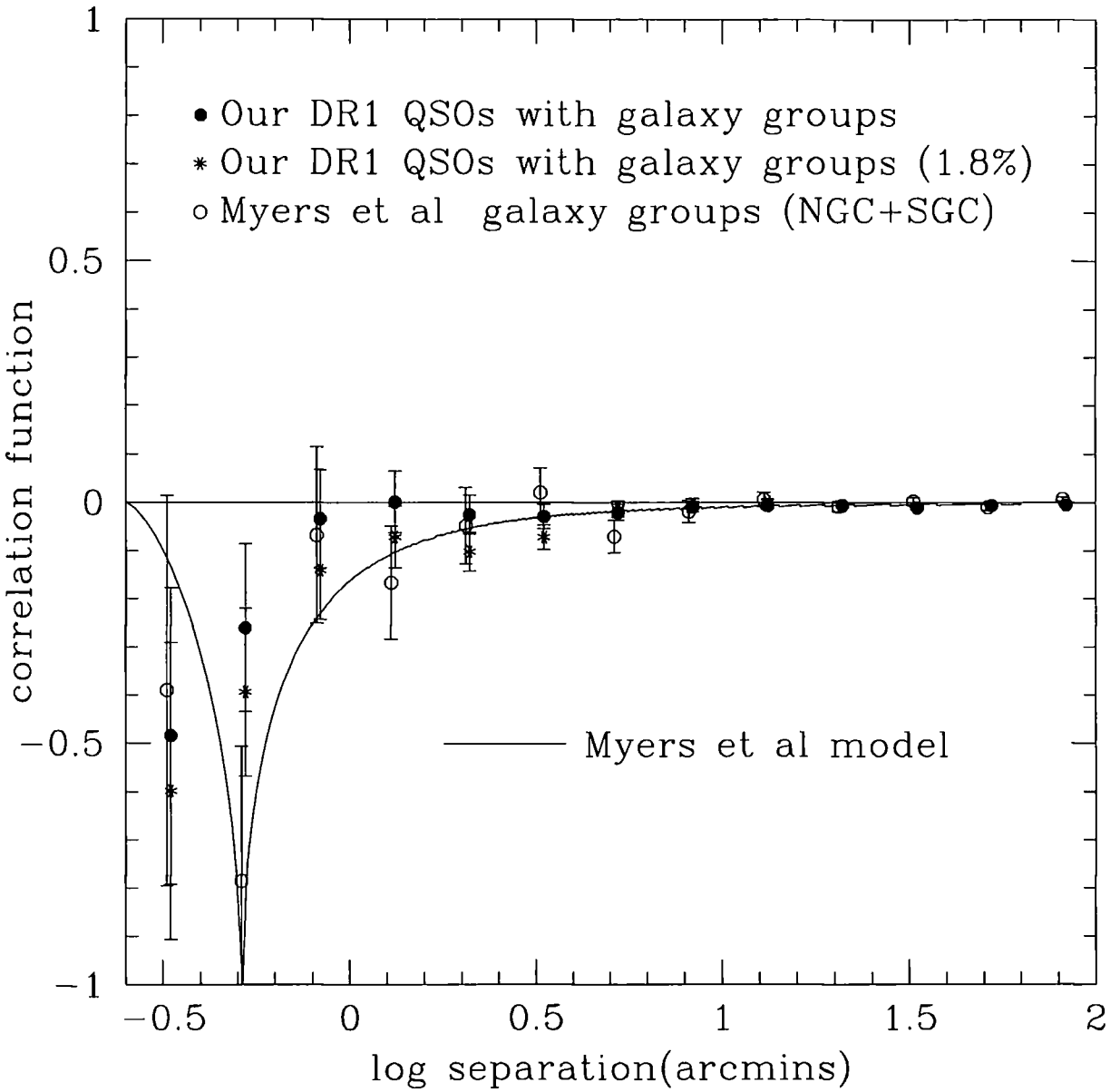

Figure 3.13: QSO-galaxy group centres cross-correlations. The filled circles show the QSO-group centres cross-correlation results as shown in Fig. 3.9. The asterisks show the results when we consider 1.8% contamination and take into account the galaxy-cluster results from Stevenson et al. Open circles show the results of Myers et al. (2003). The model from Myers et al. is also shown (solid line)

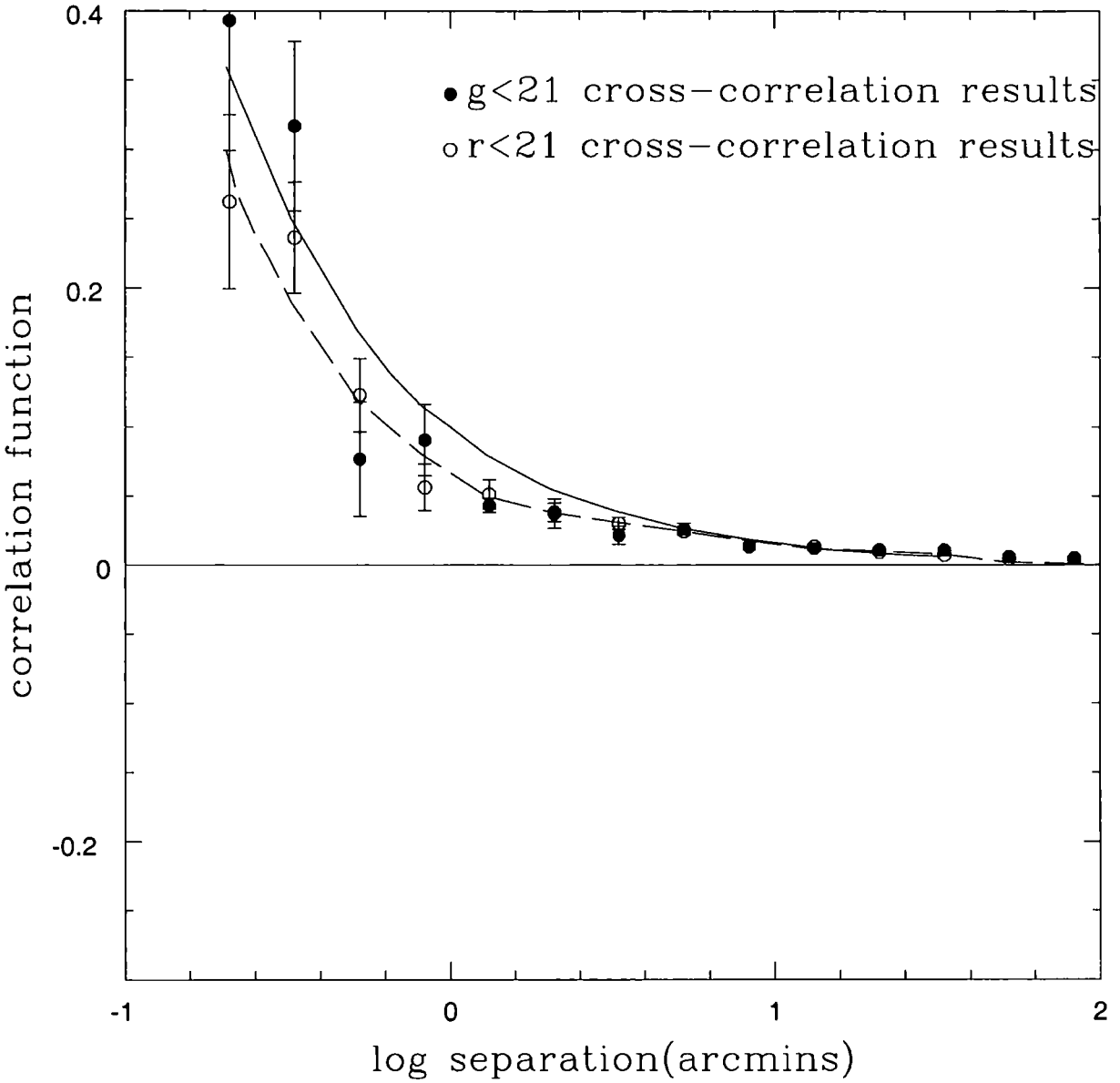

Figure 3.14: Cross-correlation of the 2,667 low redshift ($z < 0.6$) QSOs and NELGs in the NGC of the 2QZ with our $g < 21$ galaxy sample is shown by the filled circles. The line shows the best fit which is w=$0.11\theta^{-0.8}$. cross-correlation of the 2,667 low redshift ($z < 0.6$) QSOs and NELGs in the NGC of the 2QZ with our $r < 21$ galaxy sample is shown by the open circles. The dashed line shows the best fit which is w=$0.07\theta^{-0.8}$.

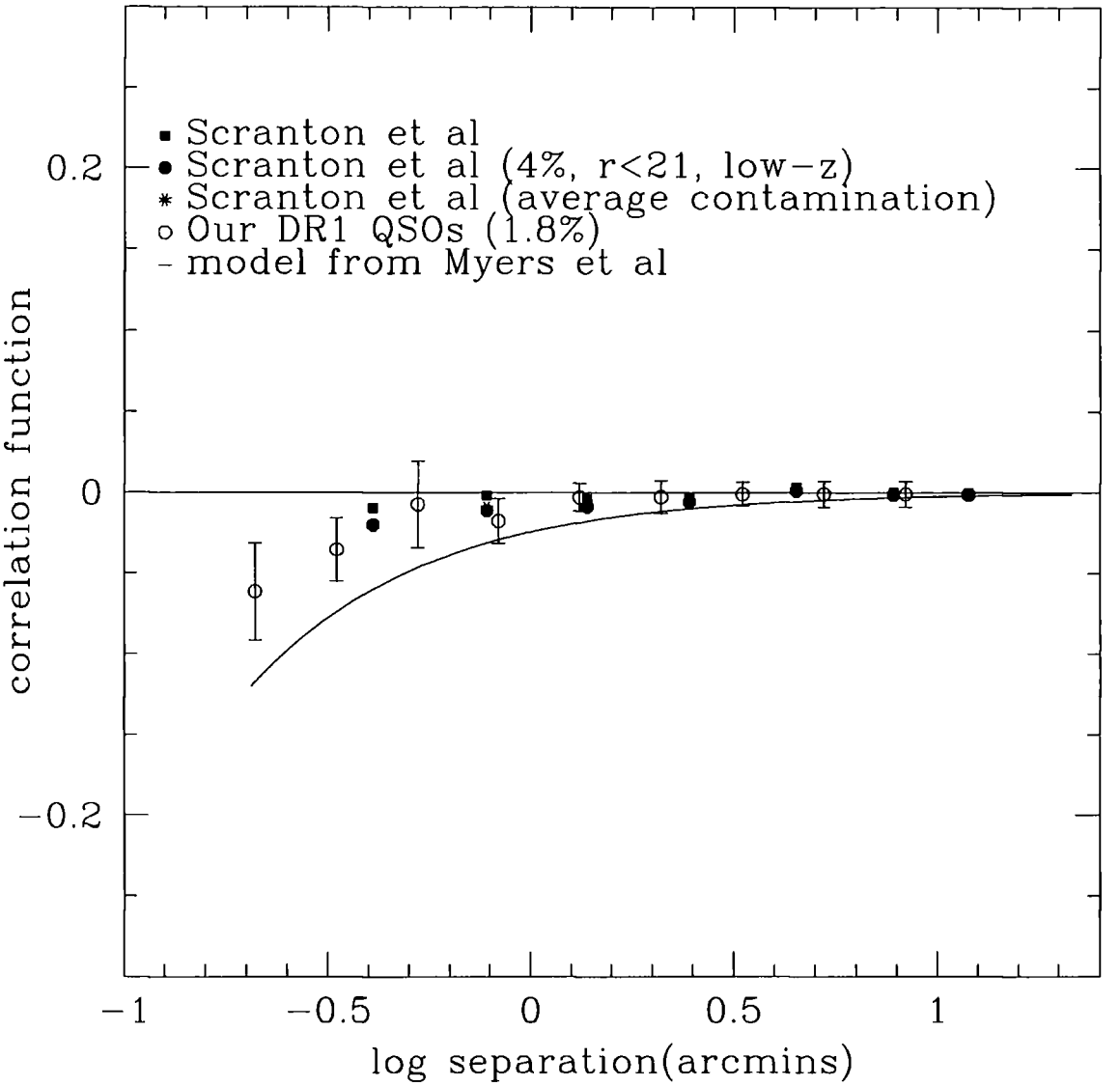

Figure 3.15: QSO-galaxy cross-correlation results. Squares show original Scranton et al. results, asterisks Scranton et al. assuming 4% contamination and the fit to the cross-correlation from the low redshift objects with $r < 21$ galaxies. Open circles show our DR1 QSOs when we apply 4% contamination and the fit to the cross-correlation from the low redhift objects with $g < 21$ galaxies. Filled circles show the results from the average of the two ways of estimating the contamination (galaxy auto-correlation and low-z objects) applied to Scranton et al. Finally, the line shows the Myers et al.(2005) model for QSO-galaxy cross-correlation.

3.6 2QZ versus SDSS comparison - including effect of the galaxy samples

As noted in Section 3.2 throughout our analysis we are using $g < 21$ galaxies whereas Scranton et al. use $r < 21$ galaxies. This is the reason (apart from the contamination of the photometric QSOs) that we don't expect to get the same answers for the QSO-galaxy cross-correlations. In Fig. 3.16 we show our auto-correlation results from $g < 21$ galaxies and the results from $r < 21$ galaxies. The galaxy auto-correlation for $g < 21$ is taken from Myers et al. (2005); the result for $r < 21$ has been calculated for 35000 SDSS galaxies to this limit. As we see there is a factor of 2-3 lower anti-correlation for the $r < 21$ galaxies. This is due to increased effects of projection on clustering in the $r < 21$ galaxy sample with its 50% increased depth and 3.5× higher sky density (3500deg^{-2} vs. 1000deg^{-2}) which leads to weaker clustering. Therefore we also expect lower lensing anti-correlation signal by a similar factor of 2-3, based at least on the models used by Myers et al. (2005) from either Williams & Irwin (1999) or Gaztanaga (2004). Using $b \approx 0.1$ in a standard ΛCDM cosmology we predict the QSO-galaxy cross-correlation result for Myers et al. for galaxies with $r < 21$ ($w_{qg}(r < 21) = \frac{A_{gg}(r<21)}{A_{gg}(g<21)} w_{qg}(g < 21)$ where A_{gg} is the amplitude of the galaxy auto-correlation function). The results are shown in Fig. 3.17. Squares show the Scranton et al. results (4% contamination averaged as described in Section 3.5.7) and the triangles show Myers et al. results renormalized for an $r < 21$ galaxy sample as described above. As we see the results are in very good agreement. So the disagreement between the Scranton et al. and Myers et al. results is due to these two factors; contamination was not taken into account by Scranton et al. and the galaxy samples in the two analyses are different. When the results are changed based on those two factors they are consistent.

As already noted, the low signal seen in the corrected cross-correlation results for bright galaxies could very well be explained by the slope of the QSO number counts in the region of interest. Table 1 of Scranton et al. (see also Myers et al., 2003) shows the slopes measured for the DR1 sample. At $19 < g < 19.5$ the slope is $\beta' = +0.56$ and at $19.5 < g < 20.0$ the slope is $\beta' = 0.43$. From equation

(A5) of Myers et al. the magnification implied for groups by the anti-correlation of $w_{qg} \simeq -0.15$ at a QSO limit of $g < 21$ is $\simeq 0.5$ mag for groups at separation of $1'$ (see Fig. 3.13). Assuming the former $\beta' = 0.56$ slope this would be imply $w_{qc} \simeq 0.2$ for the $g < 19$ QSO-group correlation in Fig. 3.10. Assuming the latter $\beta' = 0.43$ slope would imply $w_{qc} = 0.04$. This is consistent with the results shown in Fig. 3.10 at $1'$ where the contamination corrected $w_{qc} = 0.06 \pm 0.06$. The w_{qg} result of Scranton et al. at $17 < g < 19$ seems to show higher S/N than any of the others. If the contamination corrections obtained via Fig. 3.16 are the same as for the fainter samples, these results will only be slightly affected, decreasing from $w_{qg} = 0.02$ to $w_{qg} = 0.018$ on $1'$ scales.

The contamination corrected results from Scranton et al. for $17 < g < 19$ QSOs cross-correlated with $r < 21$ galaxies give $w_{qg} = 0.014 \pm 0.009$. If we take $w_{qg} = -0.01$ for $g < 21$ QSOs and the $r < 21$ galaxies then assuming $\beta' = 0.29$ at $g < 21$ and $\beta' = 0.564$ at $g \simeq 19$ this implies $w = 0.015$ from equation (A5) of Myers et al. (2003) and therefore the bright and faint results are in agreement, confirming the claim by Scranton et al. even after contamination correction.

In summary, the bright QSO-group galaxy correlation shows positive signal which is only slightly above the noise but is consistent with the anti-correlation signal at fainter magnitudes. From here on, we shall only model the faint QSO cross-correlation where the S/N is generally higher.

3.7 Galaxy model fitting

Since the observational results appear to be in agreement, the question then remains as to how the interpretations are so different. Scranton et al. claim that a standard ΛCM model can explain the QSO lensing data whereas Myers et al. suggest that $b \approx 0.1$ or a high mass density EdS cosmology (or both) is needed to explain the observations. Scranton et al. follow the Press-Schechter formalism of Jain, Scranton and Sheth (2003) assuming the standard cosmology and using the Halo Occupation Models (HOD) prescription of Zehavi et al. (2005) as fitted to the SDSS galaxy correlation function. Previous authors (e.g. Colin et al. 1999) have suggested

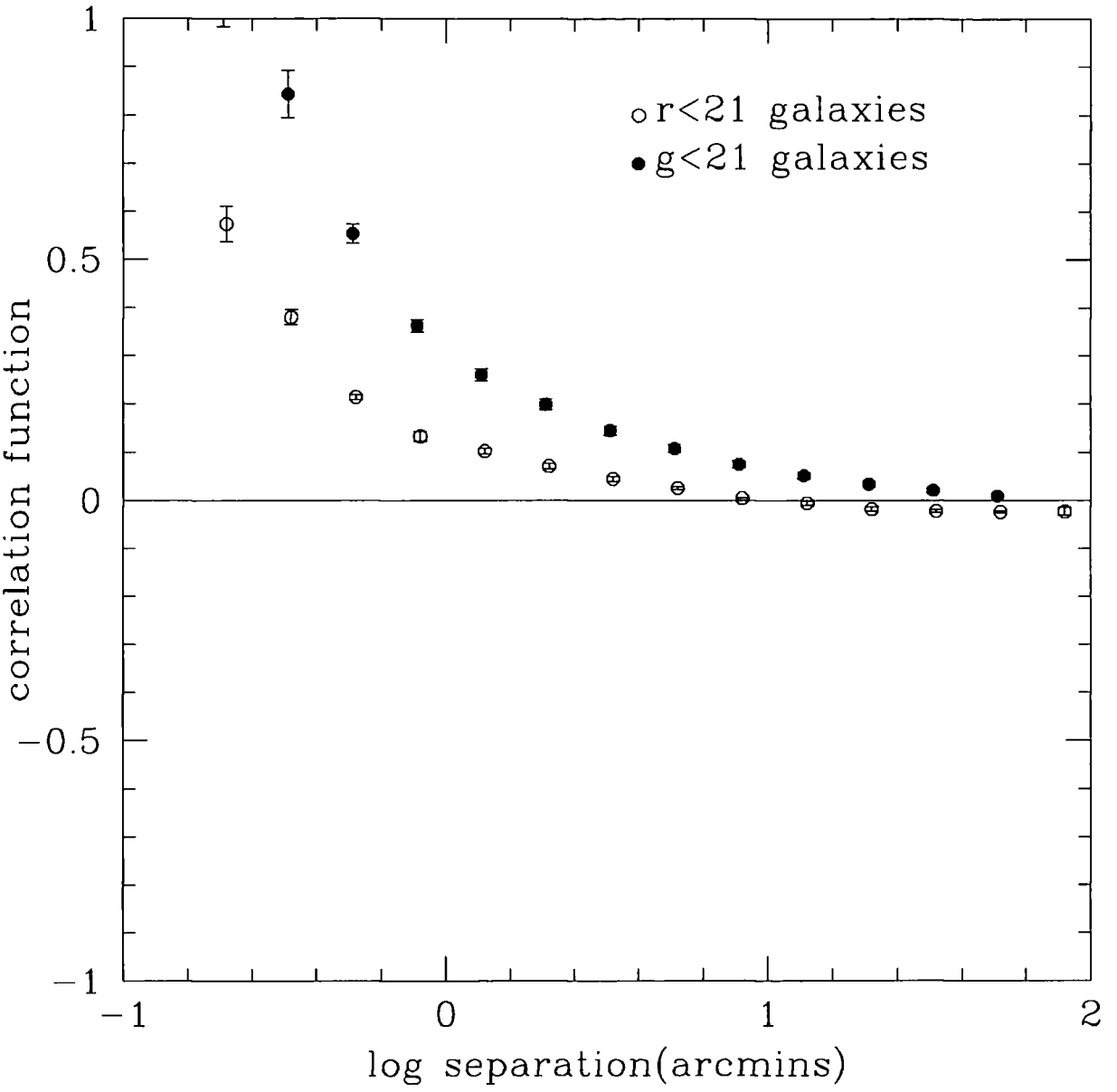

Figure 3.16: Galaxy auto-correlation results. The filled circles show the results from the $g < 21$ sample taken from Myers et al. (2005). Error bars represent 1σ jackknife errors. The open circles show the auto-correlation results for the $r < 21$ sample. The errors are field-field.

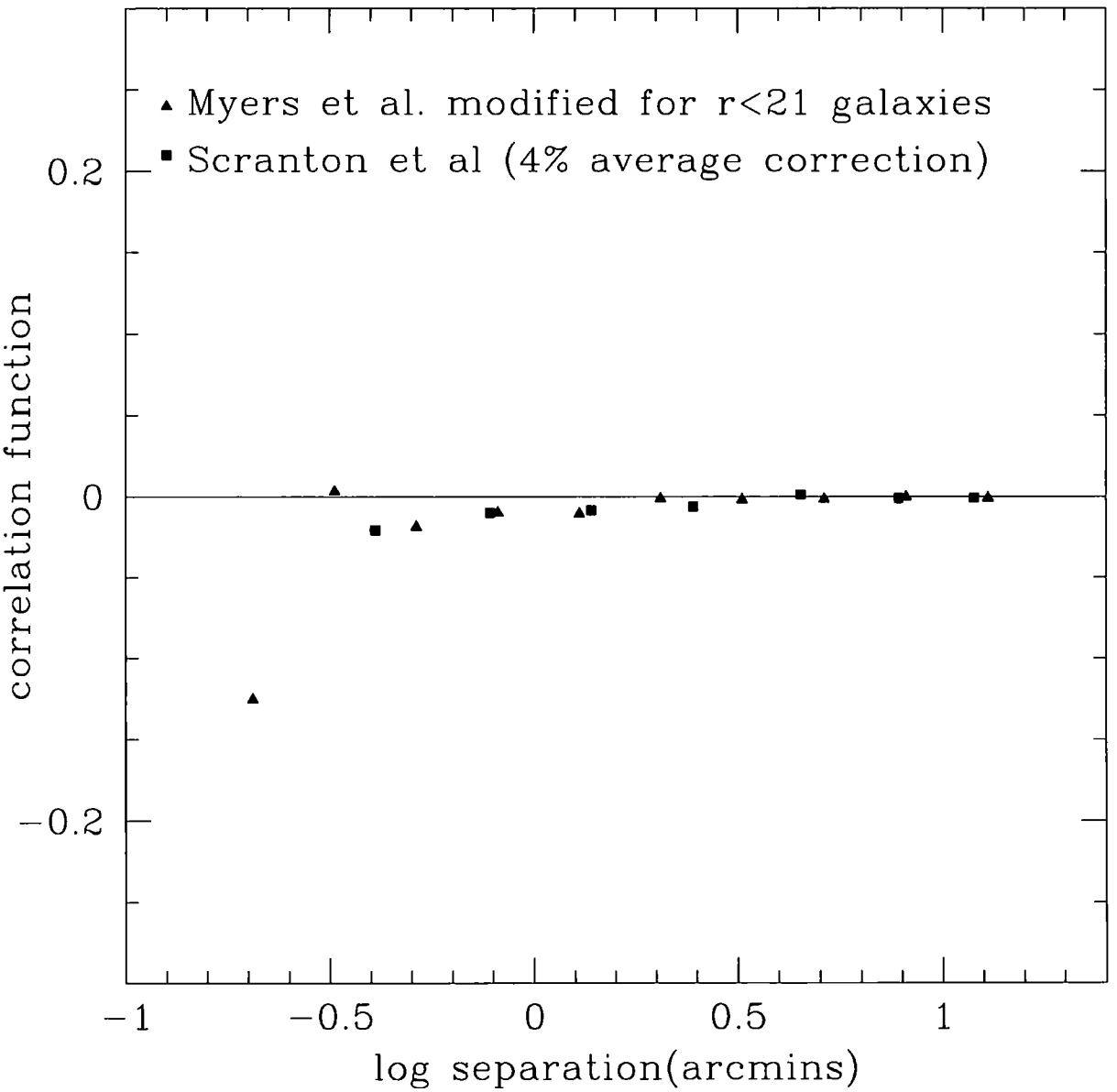

Figure 3.17: QSO-galaxy cross-correlations. The triangles show Myers et al. (2005) results modified for an $r < 21$ galaxy sample. Squares show the results from Scranton et al. averaged for 4% contamination as described in Section 5.7. The two results are in very good agreement.

that in such models there can be anti-bias at the level of up to $b \approx 0.6$ on scales $0.1 < r < 1\mathrm{h}^{-1}\mathrm{Mpc}$ with $b \approx 1$ on larger scales. As discussed by Myers et al. (2005) significantly stronger anti-bias than this at $0.1 < r < 1\mathrm{h}^{-1}\mathrm{Mpc}$ was required by their galaxy-QSO lensing results (see their Fig. 10) and these results are now strengthened by the agreement found in the new SDSS QSO datasets of Scranton et al. as well as those analysed here. We believe that the factor of ≈ 6 that we are seeking is too large to be explained by some subtlety in the HOD prescription. We also note that Guimaraes, Myers & Shanks (2006) used the Hubble Volume simulation of the standard model to test if some subtlety in either galaxy or group assignment could explain the large anti-correlation as an artefact. However, these authors confirmed that approximately unbiased galaxy distributions assuming the standard cosmology were a factor of ≈ 10 away from explaining the amplitude of anti-correlation seen with either galaxies or galaxy groups and clusters.

We take our best data for the spectroscopic 2QZ sample which is the Northern 2QZ strip reported here, combined with the Southern 2QZ strip as reported by Myers et al. (2003) for galaxies, inversely weighted by variance. We find that a fit of $w_{qg(\theta)} = -0.023 \pm 0.006\theta^{-0.96\pm0.3}$ describes our data, where θ is expressed in arcminutes. The results are shown in Fig. 3.18. Open circles show the weighted average results for both strips and the short-dashed line shows our model. The new $N+S$ result is almost exactly the same as that of Myers et al. (see their eq. 21) and so our fitted galaxy bias at $\theta = 1'$ ($\sim 0.1\mathrm{h}^{-1}\mathrm{Mpc}$) remains $b_{0.1} = 0.13 \pm 0.06$ from the model of Williams & Irwin (1998). The same model gives $b_{0.1} = 0.32 \pm 0.15$ in the Einstein-de Sitter case. Here and below, the model of Gaztanaga (2003) would give proportionately smaller bias values (see Table 1 of Myers et al. 2005).

We then take our best photometric DR1 5 areas QSO-galaxy result corrected for contamination as in Fig. 3.11. We find that a fit of $w_{qg(\theta)} = -0.007 \pm 0.005\theta^{-1.4\pm0.43}$ describes our data. In Fig. 3.18 filled circles show our results and the line shows our model. Scaling again via equation (19) of Myers et al. we find $b_{0.1} = 0.18 \pm 0.08$ for the standard cosmology in the Gaztanaga case. In the Williams & Irwin case, the result gives $b_{0.1} = 0.44 \pm 0.20$, still lower than $b \approx 1$ as suggested by Scranton et al.

Finally, we take the corrected Scranton et al. QSO-galaxy cross-correlation re-

sults (4% average correction) and find that a fit (Fig. 3.18) of $w_{qg(\theta)} = -0.009 \pm 0.003\theta^{-1.0\pm0.38}$. The squares in Fig. 19 show Scranton et al. results with a 4% average correction and the long dashed line shows our model. Scaling here via equation (19) of Myers et al. (2005) and taking into account their $r < 21$ galaxy limit gives $b_{0.1} = 0.14 \pm 0.06$ for the Gaztanaga model and $b_{0.1} = 0.32 \pm 0.15$ under the assumptions of Williams & Irwin. Again these results are in reasonable agreement with those of Myers et al.

3.8 Cluster Model Fitting

Here we fit our best new data in terms of the cluster/group lensing effect. We, first, assume that the mass distribution in the groups follow a Singular Isothermal Sphere (SIS) profile. In this case the sources are magnified by a factor

$$\mu = \frac{\theta}{\theta - 4\pi\frac{d_{ls}}{d_{os}}(\frac{\sigma}{c})^2}, \tag{3.1}$$

where d_{ls} is the distance between the lens and the source, d_{os} is the distance between the observer and the source, c is the speed of light, σ is the velocity dispersion of the SIS and θ is the angle between the source, the observer and the centre of the lens (Section 1.5). The factor $4\pi\frac{d_{ls}}{d_{os}}(\frac{\sigma}{c})^2$ is, as mentioned in Chapter 1, the Einstein radius, so $\theta_E = 4\pi\frac{d_{ls}}{d_{os}}(\frac{\sigma}{c})^2$. Then the correlation function is given by $w(\theta) = \mu^{2.5\beta'-1} - 1$, where β' is the slope of the number-magnitude relation. When $\beta' = 0.4$ then $w(\theta) = 0$, for higher values of β' we observe a correlation and for lower values an anti-correlation (Myers et al. 2003). Using the last two equations we can predict the form of the correlation function.

The second approach we follow is the so-called NFW density profile for dark matter haloes (Navarro, Frenk & White 1995, 1996, 1997). This density profile is described by the radial mass function

$$\rho(x) = \frac{\rho_s}{x(1+x)^2} \Rightarrow \theta = \frac{xr_s}{D_l}, \tag{3.2}$$

where ρ_s is the critical density and x is the radial coordinate in units of a scale radius r_s ($x \equiv \frac{r}{r_s}$). This density matter profiles describes haloes that have masses

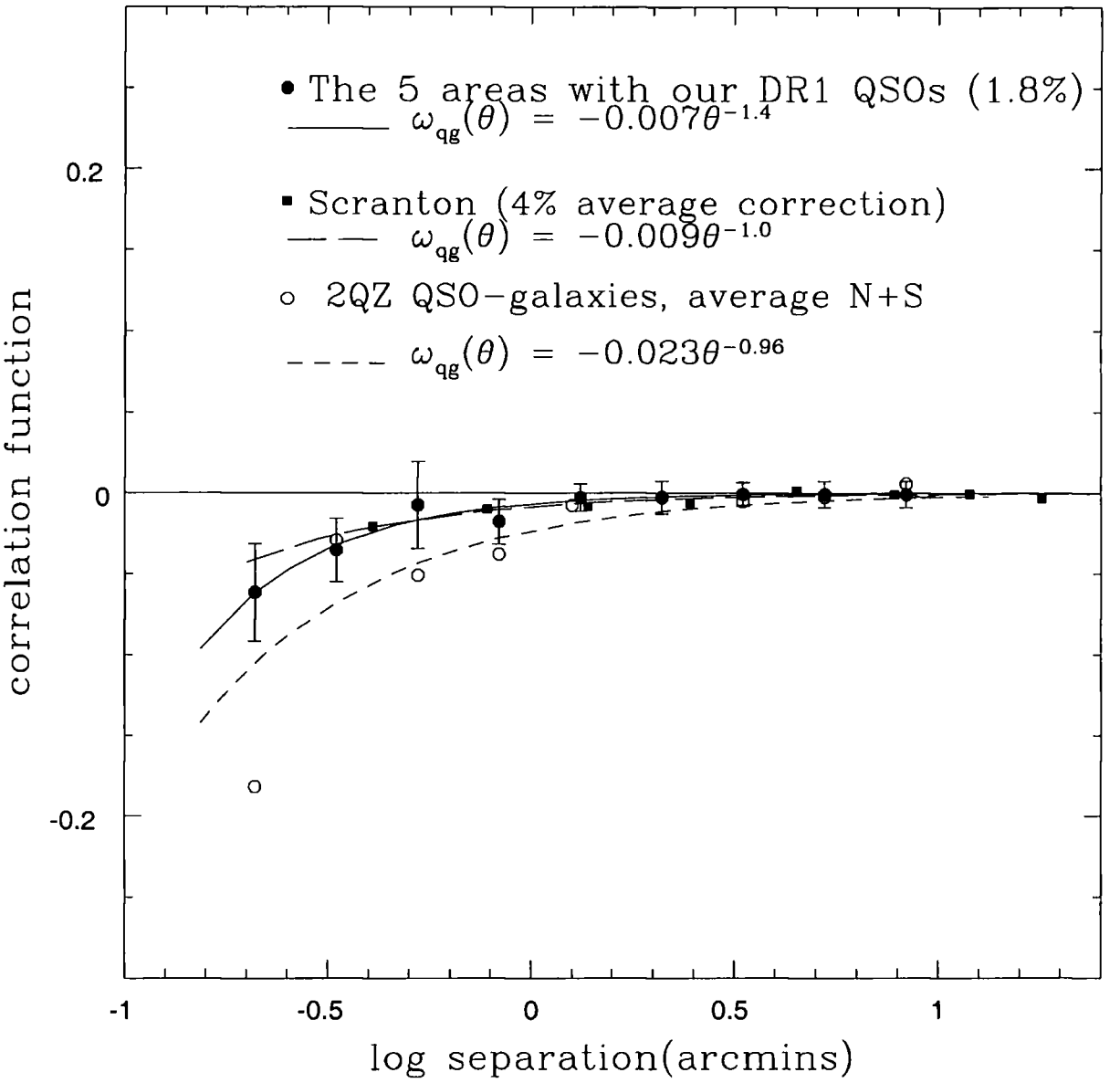

Figure 3.18: Our fits for our DR1 QSOs in the 5 areas (corrected for 1.8% contamination) and for Scranton et al. (4% average correction based on the $r < 21$ galaxy autocorrelation). The weighted averaged results from the NGC and SGC (Myers et al.) are shown by the open circles. The short dashed line shows our fit.

from 9 orders of magnitude, i.e. from globular clusters to galaxy clusters. Initially, it was restricted for the standard CDM model, but now is considered as a universal two parameter function describing the structure of dark matter haloes (Bartelmann, 1996). If we now consider lensing at a radius of the impact parameter b around the profile, then

$$x = \frac{b}{r_s} = \frac{D_l \theta}{r_s} \tag{3.3}$$

$$\theta = \frac{r_s}{D_l} x \tag{3.4}$$

$$d\theta = \frac{r_s}{D_l} dx. \tag{3.5}$$

The amount that the image will be magnified by the lens is given by equation 1.39.

$$\mu = \mid \frac{\theta}{\theta_q} \frac{d\theta}{d\theta_q} \mid . \tag{3.6}$$

Combining equation 3.4, 3.5 and 1.39 the latter becomes

$$\mu = \mid \frac{x r_s}{D_l \theta_q} \frac{r_s dx}{D_l d\theta_q} \mid \Rightarrow \mid (\frac{r_s}{D_l})^2 \frac{x dx}{\theta_q d\theta_q} \mid . \tag{3.7}$$

Maoz et al. (1997) estimated from Fig. 9 of Navarro et al. (1997) that the scale length r_s depends on the cluster mass as

$$r_s = 300(\frac{M}{10^{15} M_\odot})^\gamma h^{-1} kpc. \tag{3.8}$$

The index γ varies depending on the cosmological model and is $\gamma \sim 1/3$ for CDM. When γ is large, low mass clusters have dense central regions and can become efficient lenses. As it has already been shown (Section 1.5.1) the angle α that a light ray is bent passing within the impact parameter b from the centre of a cylindrically symmetric mass distribution is

$$\alpha = \frac{4GM(< b)}{bc^2} = \frac{d_{os}}{d_{ls}}(\theta - \theta q). \tag{3.9}$$

The latter can be re-written for a lensing cluster with surface density profile $\Sigma(r)$ and scale radius r_s, as (Maoz et al. 1996)

$$\alpha = \frac{4GM_{1.5}}{r_s c^2} f(x), \tag{3.10}$$

where $M_{1.5}$ is the mass within $1.5h^{-1}Mpc$ of the centre of the halo. The function f(x) is defined (Maoz et al. 1996)

$$f(x) \equiv \frac{1}{x}\frac{\int_0^x \Sigma(r)rdr}{\int_0^{1.5Mpc} \Sigma(r)rdr} = \frac{1}{x}\frac{g(x)}{g(1.5Mpc/r_s)}, \tag{3.11}$$

the function g(x) is given (Bartelmann, 1996)

$$g(x) = ln\frac{x}{2} + \frac{2}{\sqrt{x^2-1}} tan^{-1}\sqrt{\frac{x-1}{x+1}}\ , (x > 1) \tag{3.12}$$

$$g(x) = ln\frac{x}{2} + \frac{2}{\sqrt{1-x^2}} tanh^{-1}\sqrt{\frac{1-x}{1+x}}\ , (x < 1) \tag{3.13}$$

$$g(x) = ln\frac{x}{2} + 1(x = 1). \tag{3.14}$$

From 3.10 and 3.11 we get

$$\alpha = \frac{4GM_{1.5}}{c^2 r_s g(1.5Mpc/r_s)}\frac{g(x)}{x}. \tag{3.15}$$

From 3.9 and 3.15 we get

$$\frac{d_{os}}{d_{ls}}(\theta - \theta q) = \frac{4GM_{1.5}}{c^2 r_s g(1.5Mpc/r_s)}\frac{g(x)}{x} \Rightarrow \theta q = \theta - \frac{4GM_{1.5}}{c^2 r_s g(1.5Mpc/r_s)}\frac{g(x)}{x}\frac{d_{ls}}{d_{os}}. \tag{3.16}$$

The derivative of the last equation with respect to x gives,

$$\frac{d\theta q}{dx} = \frac{d\theta}{dx} - \frac{d_{ls}}{d_{os}}\frac{4GM_{1.5}}{c^2 r_s g(1.5Mpc/r_s)}\frac{d\frac{g(x)}{x}}{dx}. \tag{3.17}$$

Deviding now 3.16 by x gives,

$$\frac{\theta q}{x} = \frac{\theta}{x} - \frac{4GM_{1.5}}{c^2 r_s g(1.5Mpc/r_s)}\frac{g(x)}{x^2}\frac{d_{ls}}{d_{os}}. \tag{3.18}$$

Now taking into consideration from 3.4 that $\frac{x}{\theta} = \frac{D_l}{r_s}$, equation 3.18 gives,

$$\frac{\theta q}{x} = \frac{r_s}{D_l} - \frac{d_{ls}}{d_{os}}\frac{4GM_{1.5}}{c^2 r_s g(1.5Mpc/r_s)}\frac{g(x)}{x^2}. \tag{3.19}$$

Similarly, equation 3.17 becomes ($\frac{d\theta}{dx} = \frac{r_s}{D_l}$)

$$\frac{d\theta q}{dx} = \frac{r_s}{D_l} - \frac{d_{ls}}{d_{os}} \frac{4GM_{1.5}}{c^2 r_s g(1.5Mpc/r_s)} \frac{d\frac{g(x)}{x}}{dx}. \tag{3.20}$$

Implementing equation 3.19 and 3.20 into equation 3.7 we can numerically find the magnification.

Following now the 2 procedures written above we take our best photometric DR1 5 areas dataset corrected for contamination as in Fig. 3.13 for centres of groups. Using a χ^2 fit after the fashion of Myers et al., we find that a velocity dispersion of 1040 kms^{-1} fits the $n > 7$ group data ($\chi^2_{red} = 0.7$) and the SIS model is shown in Fig. 3.19 by the solid line. This value is higher by a factor of ≈ 3 than what is expected for groups (see also Chapter 5). One reason may be that our $n > 7$ galaxy group sample also contains very rich clusters with high velocity dispersions. Moreover line-of-sight contamination may be an additional reason that boosts our velocity dispersion measurements. Nevertheless, this is close to the value of 1156kms^{-1} found by Myers et al. We, also fit the NFW profile which is shown by the long dashed line. The best NFW fit has a mass of $M_{1.5}^{DR1} = 1.3 \times 10^{15} h^{-1} M_\odot$ with $\chi^2_{red} = 1.0$.

Finally, in a similar way as we did in the previous Section we combine our results from the cross-correlation of 2QZ QSOs with centres of groups in the NGC with Myers et al. results in the SGC and then we fit a model to our weighted average results (open circles, Fig. 3.19). Here our χ^2 fit for the SIS velocity dispersion yields 1060 kms^{-1} ($\chi^2_{red} = 1.3$) again close to the value found by Myers et al. The SIS model is shown by the dotted line in Fig. 3.19. The NFW profile in this case yields a mass of $M_{1.5}^{2QZ} = 1.0 \times 10^{15} h^{-1} M_\odot$ with $\chi^2_{red} = 1.5$.

3.9 Discussion + Conclusion

Using a photometric QSO sample which was extracted by the same method as that of Scranton et al. we have investigated the reasons that their results appear different from Myers et al. (2005), giving a lower anti-correlation signal.

We first cross-correlated our DR1 SDSS QSO sample with galaxies ($g < 21$)

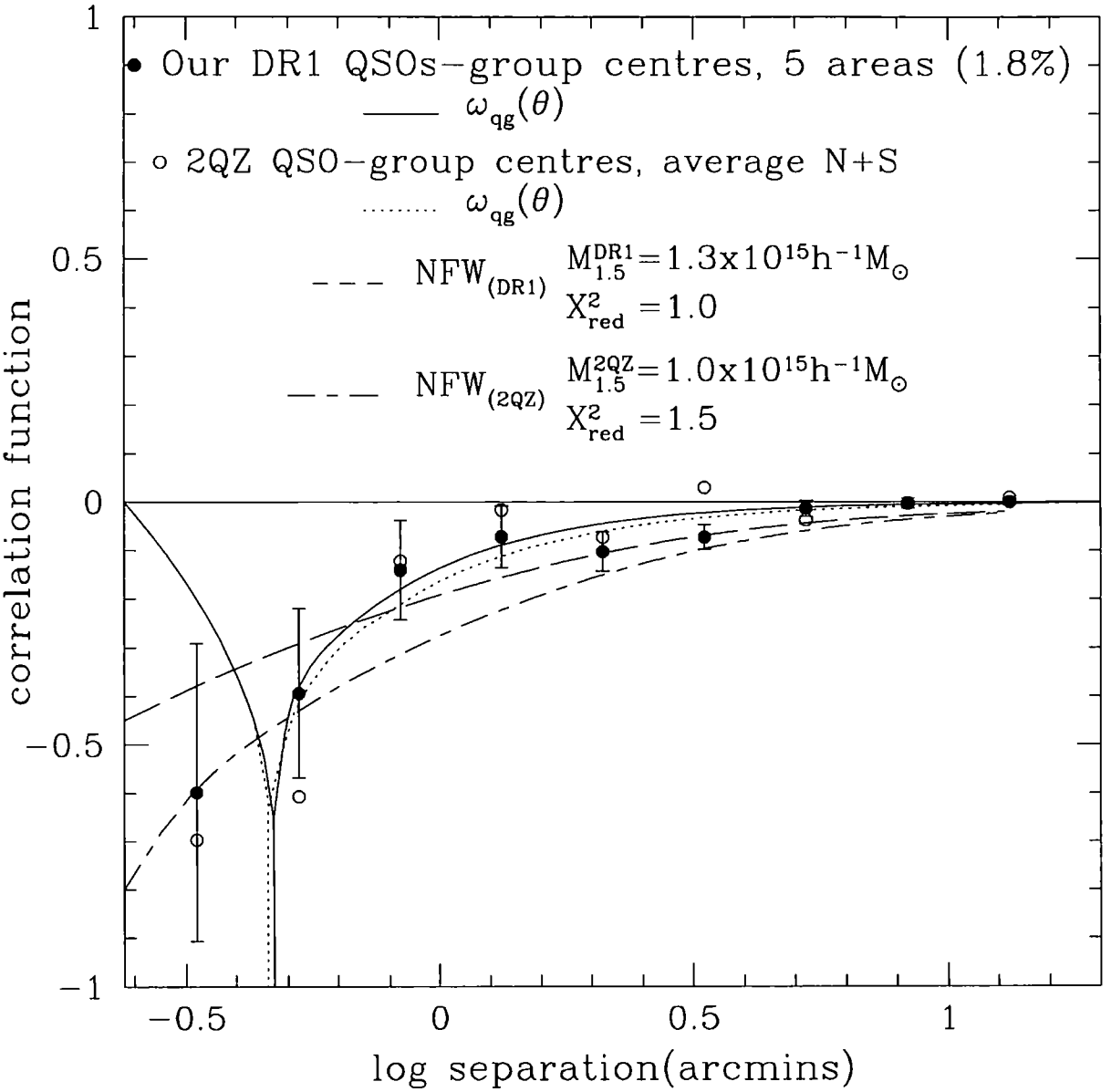

Figure 3.19: Our weighted average results for both the North and South strips are shown by the filled circles and the fit to them by the dotted line. The χ^2 fit for the cross-correlation of our DR1 QSOs and centres of groups in the 5 areas (corrected for 1.8% contamination) is shown by the solid line. 2QZ results are similarly represented by the open circles and the dotted line. The long dashed line shows the best fitting NFW model profile for the DR1 QSO-group centres cross-correlation and the long-short dashed line for the 2QZ QSO-group centres cross-correlation.

and found that our results are in reasonable agreement with Myers et al. (2005) at least on scales larger than 1′. 2QZ QSOs and DR1 QSOs cross-correlated with the same $g < 21$ galaxy sample give consistent results on scales larger than 1′. The results of Scranton et al. show a smaller anti-correlation signal as expected from the different galaxy sample ($r < 21$) that they use. In the case of cross-correlations between QSO-galaxies in clusters, the results repeat the same pattern in that we detected anti-correlation consistent with the results of Myers et al. (2003) but at considerably higher S/N than for galaxies.

Based on the low-redshift contamination in the $1 < z_p < 2.2$ photometric SDSS QSO sample as estimated in Chapter 2 ($\approx$ 2% for $z_s < 0.3$ and $\approx$ 4% for $z_s < 0.6$), we then corrected our DR1 results and Scranton et al. results assuming these percentages of contamination. Then comparing the autocorrelation results from $g < 21$ and $r < 21$ galaxies we modified Myers et al. (2005) QSO-galaxy cross-correlation results and we found that the observational results are actually in very good agreement.

Therefore we have found that there are two reasons that Scranton et al. and Myers et al. results look different. The first is that the low-redshift contamination in the photometric QSO sample has not been taken into account and the second is that the galaxy sample used in each analysis is different. *When we account for these effects, we consider that the Scranton et al. SDSS results at faint magnitudes provide strong observational confirmation of the results of Myers et al. (2005, 2003) in the same QSO magnitude range.*

Correcting for low-redshift contamination also lowers the positive correlation claimed by Scranton et al. at bright magnitudes. However, in the $17 < g < 19.0$ bin of Scranton et al. some positive signal is still seen even after contamination correction, at an appropriate amplitude to match the anti-correlation seen at fainter magnitudes. But the strong anti-correlation seen at QSO limit $g < 21$ suggests that the relevant slope for $g < 19$ QSO samples ($\beta' = 0.564$) is close to the critical $\beta' = 0.4$ slope found at $19 < g < 20$. This means that little positive correlation is expected in this magnitude range despite the strong anti-correlation seen at fainter QSO magnitudes. We note that for cluster/group lensing the relevant slope may

be in the n(m) bin fainter than the QSO limit because this is where the QSOs sit before magnification.

This then leaves the question of why Myers et al. require a strong anti-bias of $b \approx 0.1$ in the standard cosmology to explain the faint QSO anti-correlation whereas Scranton et al. require $b \approx 1$. We have noted that Scranton et al. use a more complicated analysis than that of Myers et al. (2005), using the HOD of Zehavi et al. (2005). However, the HOD that they use appears to have $b \approx 0.6 - 1$ in the region of interest and it appears difficult to explain away the factor of $6 - 10$ discrepancy by other subtleties in the HOD approach. Moreover, Guimaraes, Myers and Shanks (2005) used mock galaxy catalogues with $b \approx 1$ derived from the Hubble Volume simulation using standard parameters and confirmed that models with $b \approx 1$ are a factor of ≈ 10 away from explaining the QSO magnification data.

With the SDSS results now observationally confirming the 2QZ results, we believe that QSO lensing has now come of age. We note there remain discrepancies with the $b \approx 1$ results found from weak-lensing cosmic shear results. However as noted by Hirata & Seljak (2004) there are serious potential problems with weak lensing shear results in that the effects of intrinsic galaxy alignments are difficult, if not impossible, to eliminate from the shear analysis. It is important to reconcile the QSO magnification and weak shear results for if it proves that our QSO magnification results are more accurate then the consequences for cosmology would be significant. For example, Shanks (2007) has noted the potential impact of the QSO magnification results on the interpretation of the acoustic peaks in the CMB.

Chapter 4

QSO-LRG 2-Point Cross-Correlation Function and Redshift-Space Distortions

4.1 Introduction

Useful constraints on the nature of QSOs can be drawn from even the simplest measure of QSO clustering, the amplitude of the real-space 2-point correlation function. For example, measuring QSO clustering on small scales can constrain models of galaxy mergers and quasar formation (Myers et al. 2007). Furthermore, the redshift evolution and luminosity dependence of the QSO bias can be studied. Recent work on the clustering dependence of the QSO bias on redshift suggested evolution of the 2QZ QSO bias (Croom et al. 2005). However, the fact that the most luminous QSOs lie at high redshifts, while the faintest are at low redshifts, made it difficult to study how QSO properties depend on luminosity. Surveys such as 2SLAQ, that span a wide range of QSO luminosities, have broken that redshift-luminosity degeneracy and revealed little QSO clustering dependence on luminosity, at fixed redshift (da Ângela et al. 2008). Moreover, the amplitude of the QSO clustering is correlated with the average mass of the halos associated with the QSOs, providing indications of QSO lifetimes and making it possible to constrain QSO evolutionary models (Croom et al. 2005, da Ângela et al. 2008).

Redshift space distortions of the clustering pattern also contain dynamical information on the QSO bias that are independent of any assumption about underlying mass clustering. The clustering is affected at small scales by the rms velocity dispersion of QSOs along the line-of-sight (Fingers of god) and, second by dynamical infall of matter into higher density regions, which causes a flattening of the clustering pattern in the redshift direction. In addition to these dynamical distortions, geometrical distortions are introduced if a wrong cosmological model is used in order to convert the observed redshifts into comoving distances. They therefore also constrain, more weakly, the value of the cosmological density parameter, Ω_m.

In the linear regime of clustering, dynamical infall is governed by the parameter $\beta = \Omega_m^{0.6}/b$. (Peebles, 1980, Kaiser 1987, Loveday et al. 1996, Matsubara & Suto 1996, Matsubara & Szalay 2001, Peacock et al. 2001, Hoyle et al. 2002, da Ângela et al. 2008, Ross et al. 2007). In recent years, measurements of QSO clustering (da Ângela et al. 2008) yielded a $\beta_{QSO}(z = 1.4) = 0.60^{+0.14}_{-0.11}$ and $b_{QSO}(z = 1.4) = 1.5 \pm 0.2$ for a combined sample of QSOs from the 2dF QSO Redshift Survey (2QZ, Croom et al. 2004) and the 2dF-SDSS LRG and QSO Survey (2SLAQ, Cannon et al. 2006). Ross et al. 2007 performed similar measurements on the 2SLAQ Luminous Red Galaxies (LRGs) clustering and found $\beta_{LRG}(z = 0.55) = 0.45^{+0.05}_{-0.05}$ and $b_{LRG}(z = 0.55) = 1.66 \pm 0.35$.

In this Chapter we use QSOs from the 2QZ, 2SLAQ and SDSS (DR5) surveys and LRGs from 2SLAQ and AAOmega first to study the dependence of QSO-LRG clustering amplitude on QSO luminosity. We also measure QSO-LRG redshift distortions to estimate the dynamical infall parameter, β. These surveys provide large numbers of QSOs and LRGs with a range of luminosities at fixed redshifts. So our results, for example on QSO bias, should be statistically improved over those from QSO-QSO clustering. Moreover, we use photometric LRG samples, which are significantly larger than the spectroscopic ones and measure QSO 2-D correlation function amplitudes, using Limber's formula to convert to 3-D real-space measurements.

In Section 4.2 we describe the QSO and LRG samples we use in our measurements. In Section 4.3 we present results from the 2-point cross-correlation function $\omega(\theta)$, in Sections 4.4 and 4.5 we show our results for the redshift-space cross-

correlation function, ξ_s, and the semi-projected cross-correlation function, $w_p(\sigma)/\sigma$, respectively. Section 4.6 has our results for the real-space cross-correlation function and in Section 4.7 we present our $\xi(\sigma,\pi)$ results, model the redshift-space distortions and estimate the QSO infall mass and bias. We also study, in Section 4.8, the dependence of the redshift-space cross-correlation function, the QSO bias and the mass of the QSO-LRG Dark Matter Haloes (M_{DMH}) on QSO luminosities at fixed redshifts. Finally, in Section 4.9 we present our conclusions.

4.2 Data

4.2.1 Spectroscopic data

Our spectroscopic LRG sample is taken from the 2SLAQ and consists of 8,656 LRGs within $0.35 \leq z \leq 0.75$ (that is the 'Gold Sample' of Ross et al. 2007, see their Fig. 1 for the LRG distribution). 5,995 LRGs are in the Northern strip (sectors a, b, c, d, e, from Fig. 1 of Ross et al.) and 2,661 LRGs in the Southern strip (sector s).

Our QSOs are taken from three spectroscopic samples; the NGC of 2QZ, the NGC+SGC of 2SLAQ and the Data Release 5 (DR5) of SDSS. The QSO redshift range mainly used in our analysis is the same one as for the 2SLAQ LRGs ($0.35 \leq z \leq 0.75$). The 2SLAQ QSOs have the same distribution on the sky as the spectroscopic 2SLAQ LRGs (see Fig. 2 of da Ângela et al.). The 2QZ and SDSS QSOs cover only the NGC of the 2SLAQ LRGs. The brightest of our QSO samples is from SDSS, which consists of QSOs with $i_{AB} < 19.1$. Our 2QZ sample consists of QSOs with $18.25 \leq b_J \leq 20.85$ and the 2SLAQ sample of QSOs with $18.0 \leq g \leq 21.85$. After matching the QSO and spectroscopic 2SLAQ LRG areas we get the numbers shown in Table 4.1.

4.2.2 Photometric data

For measuring the 2-point angular cross-correlation function, $w(\theta)$, we can also use larger, photometric LRG samples from the 2SLAQ and the AAOmega surveys. For the AAOmega LRGs we have followed the selection criteria of Ross et al. (2007).

Table 4.1: The numbers of spectroscopic QSOs and spectroscopic 2SLAQ LRGs.

2SLAQ area ($0.35 \leq z \leq 0.75$)		
	QSOs	LRGs
2SLAQ	699	8,656
2QZ	307	5,995
SDSS	218	5,995

Table 4.2: The numbers of spectroscopic QSOs and photometric LRGs.

	2SLAQ area ($0.35 \leq z \leq 0.75$)		AAOmega area ($0.45 \leq z \leq 0.90$)	
	QSOs	LRGs	QSOs	LRGs
2SLAQ	503	19,300	786	23,836
2QZ	1,048	32,188	1,265	40,060
SDSS	7,395	468,416	7,083	571,676

The numbers for these LRG data sets and the new matched QSO samples are shown in Table 4.2. We should mention here that in the case of photometric 2SLAQ and AAOmega LRGs with the 2SLAQ QSOs we did not perfectly match the two areas. The photometric 2SLAQ LRG area is a rectangle ($137.5° \leq ra \leq 230.0°$, $-1.25° \leq dec \leq 1.0°$) which covers the whole NGC of 2SLAQ, including the gaps in between the sectors a, b, c, d, e, whereas the 2SLAQ QSOs have the distribution mentioned in the previous Section. This slight mis-match does not affect our results, but is the reason that, in Table 4.2, photometric 2SLAQ LRGs matched with 2SLAQ QSOs appear more numerous than the spectroscopic 2SLAQ LRGs matched with 2SLAQ QSOs in Table 4.1 (19,300 vs. 8,656). Furthermore, the 2SLAQ QSO set, in the 2SLAQ photometric area, is smaller than that in the 2SLAQ spectroscopic area (503 vs 699) because in the photometric case we do not use the SGC part of 2SLAQ (sector s).

The redshift distribution of all the QSO samples, in a redshift range of $0.0 < z \leq 1.0$ is shown in Fig. 4.1. The 2SLAQ and 2QZ distributions are, as expected,

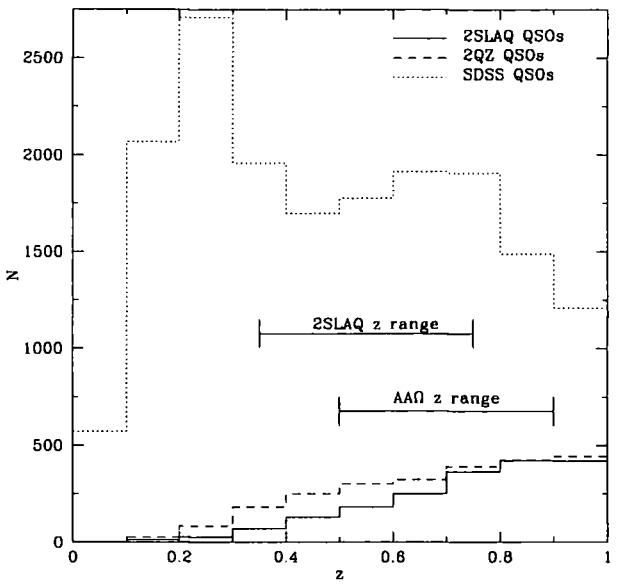

Figure 4.1: The solid line shows N(z) for the 2SLAQ, the dashed line for the 2QZ and the dotted line for the SDSS QSO samples. The 2SLAQ and 2QZ distributions are, as expected, very similar. The SDSS distribution is flat, in the 2SLAQ and AAOmega redshift ranges we are interested in.

very similar. The SDSS distribution is roughly flat, in the redshift range we are interested in, although we note a peak at $z \simeq 0.2$ which is outside our region of interest. Fig. 4.2 shows the redshift distribution of our 2SLAQ LRG sample.

4.3 QSO-LRG angular cross-correlation function

4.3.1 Cross-correlation and error estimators

In this Section we first estimate the 2SLAQ QSO−2SLAQ LRG and 2QZ QSO−2SLAQ LRG angular cross-correlation functions $w(\theta)$ using our spectroscopic samples, both for QSOs and LRGs. We then cross-correlate our photometric 2SLAQ and AAOmega LRG samples with 2SLAQ, 2QZ and SDSS (DR5) QSOs. The estimator we use is given by equation 1.44, where n_{ran} is the number of points in our random cata-

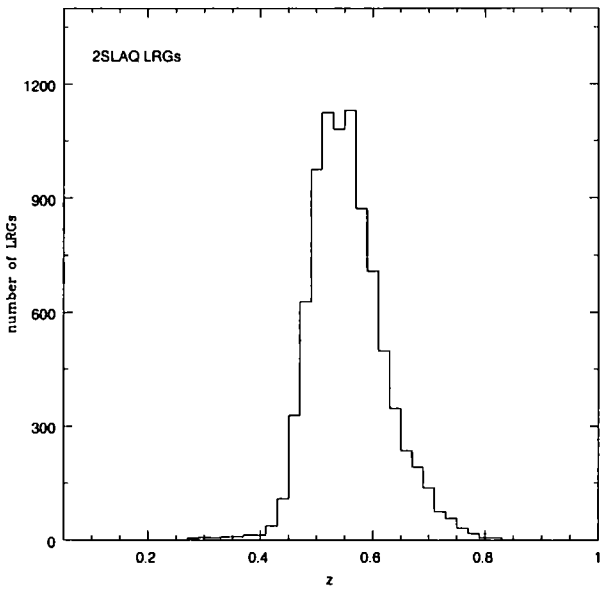

Figure 4.2: N(z) for the 2SLAQ LRG sample.

logue, n_{data} is the number of LRGs, $DD(\theta)$ are QSO-LRG pairs and $DR(\theta)$ are the QSO-random point pairs counted at angular separation $x = \theta$.

Our spectroscopic LRG random catalogue is the same as that described by Ross et al. 2007 (with 20× more randoms than LRGs) whereas the photometric 2SLAQ and AAOmega LRG random catalogues contain $\simeq 11\times$ more randoms than LRGs. Coverage completeness and spectroscopic completeness are taken into account in the construction of all random catalogues.

The accuracy of the errors on our measurements plays an important role, particularly when we use our results to model the redshift-space distortions in Section 4.7. For that, the error estimator we use throughout this Chapter is the Field-to-Field estimator given by equation 1.48. In order to calculate the Field-to-Field errors we have divided the 2SLAQ area into 4 approximately equal areas.

4.3.2 $w(\theta)$ results from the redshift samples and correction for fibre collision

Fig. 4.3 shows our angular correlation results when we cross-correlate 2SLAQ QSOs with spectroscopic 2SLAQ LRGs. Filled circles show the results when we cross-correlate our entire 2SLAQ QSO sample with the 2SLAQ LRGs. Open circles show the results from 2SLAQ QSOs in the redshift range of $1.0 \leq z \leq 2.2$ cross-correlated with the same LRG sample. Finally, triangles show the results when we use 2SLAQ QSOs in the redshift range of $0.35 \leq z \leq 0.75$. The fibre collision problem affects our results as can be seen from the anti-correlation we find, in all cases, between our QSOs and LRGs on small scales. The results are very similar when we use 2SLAQ QSOs in the whole redshift range and within $1.0 \leq z \leq 2.2$. The anti-correlation amplitude is increased when we use our low redshift QSO sample, which also shows an increased fibre effect, but its statistical significance is smaller as the sample is much smaller than the other two. Now, we shall use these results in order to correct our 2-D and 3-D results, for fibre collisions.

We shall base our correction on the Hawkins et al. (2003) expression, i.e.

$$w_f = \frac{1 + w_p}{1 + w_z}, \tag{4.1}$$

w_p is the cross-correlation results when our samples come from the input catalogue and in our QSO-LRG case $w_p = 0$ if there is no redshift overlap between QSOs and LRGs and assuming no lensing. w_z represents the cross-correlation results from the 2SLAQ catalogue and these are the results shown in Fig. 4.3. The correction should therefore be

$$w_f = \frac{1}{1 + w_z}. \tag{4.2}$$

Next, we determine w_z based on the measurements shown in Fig. 4.3. As already noted, on small scales ($\leq 2'$), we see the anti-correlation caused by the fibre effect. We also note a small positive bump on scales up to $\sim 80'$. This bump is expected to be caused by physical QSO-LRG cross-correlations for the $0.35 \leq z \leq 0.75$ range (triangles) and also to a lesser extent in the unrestricted redshift range (closed

circles). The cause of small positive excess seen at the $1.0 \leq z \leq 2.2$ could be due to the fibre collision effect. If we include this small positive bump in the fibre correction, our $\xi(s)$ cross-correlation measurements do not change. Therefore, this bump will be ignored when we present our 3-D results in the next Section. Nevertheless, the feature's effect is larger for the 2SLAQ QSO-2SLAQ (photometric) LRG $w(\theta)$ measurements which will be presented later (Fig. 4.5) and it will be taken into account there.

Finally, Fig. 4.4 shows our results when we cross-correlate 2QZ QSOs with spectroscopic 2SLAQ LRGs. No fibre collision effect is expected in this case since 2QZ QSOs had higher priority than 2dFGRS galaxies for spectroscopic observations. Thus there is no issue of fibre incompleteness (see also, e.g., Myers et al. 2003). The reason for performing these measurements is to see if we can detect any signal in the case of the overlapped redshift range (triangles). Although the results when we use 2QZ QSOs in $1.0 \leq z \leq 2.2$ range (open circles) seem to give a null average signal as expected, in the case of the common QSO-LRG redshift range (triangles) the samples are small and the results appear too noisy to draw any statistically significant conclusions.

4.3.3 Results from the photometric samples

Before we proceed to measure the redshift-space cross-correlation function, we shall repeat our $w(\theta)$ measurements, cross-correlating our spectroscopic QSO samples from SDSS, 2QZ and 2SLAQ with the photometric LRG samples, which were presented in Section 4.2.2 and Table 4.2. The purpose of these measurements is to see how the LRGs correlate with bright and faint QSOs and then use Limber's formula to convert these 2-D measurements into 3-D real-space measurements and compare them with our results from the spectroscopic samples (Section 4).

The results using 2SLAQ photometric LRGs are shown in Fig. 4.5 (filled circles are corrected for fibre collisions, from $0.1' < \theta < 100'$, i.e. including the bump in Fig. 4.3) and the results using the AAOmega photometric LRGs are shown in Fig. 4.6. We should note that neither the AAOmega nor the 2SLAQ results have been corrected for stellar contamination of the LRGs ($\simeq 15\%$ in AAOmega and $\approx 5\%$ in

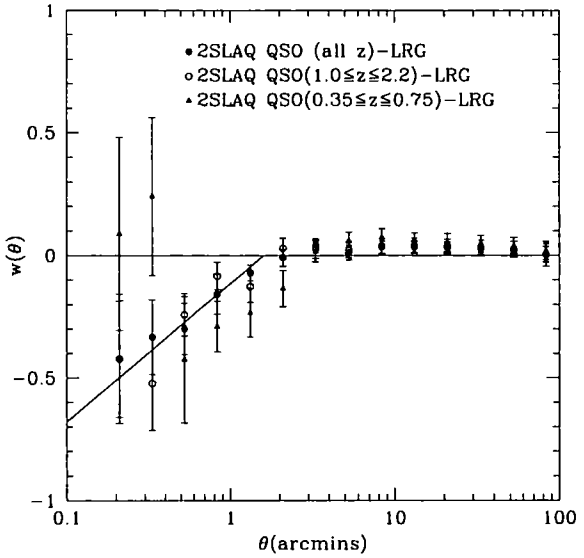

Figure 4.3: 2SLAQ QSO-2SLAQ (spectroscopic) LRG cross-correlation results. There are (9,044) 2SLAQ QSOs in the whole redshift range (filled circles), 6,002 2SLAQ QSOs between $1.0 \leq z \leq 2.2$ (open circles) and 699 2SLAQ QSOs with redshift range $0.35 \leq z \leq 0.75$. The 2SLAQ (spectroscopic) LRG sample consists of 8,656 LRGs. The solid line shows our best fit to the results (filled circles) on small scales ($\theta < 2'$).

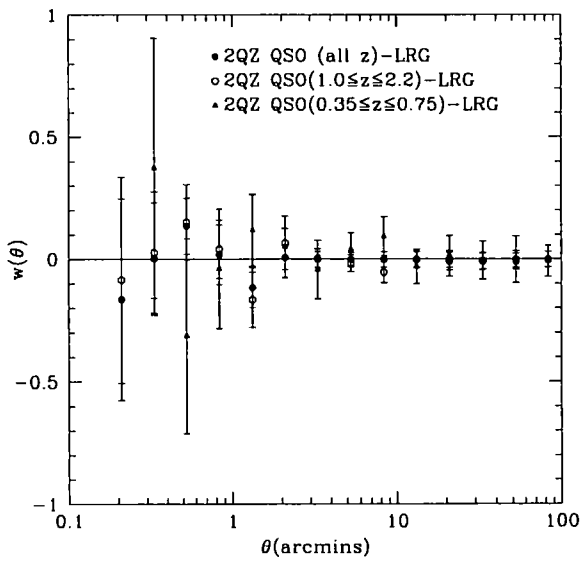

Figure 4.4: 2QZ QSO-2SLAQ LRG cross-correlation results. There are (2,854) 2QZ QSOs ('11' quality) in the whole redshift range (filled circles), 1,699 2QZ QSOs between $1.0 \leq z \leq 2.2$ (open circles) and 307 2SLAQ QSOs with redshift range $0.35 \leq z \leq 0.75$. The 2SLAQ (spectroscopic) LRG sample consists of 5,995 LRGs (NGP).

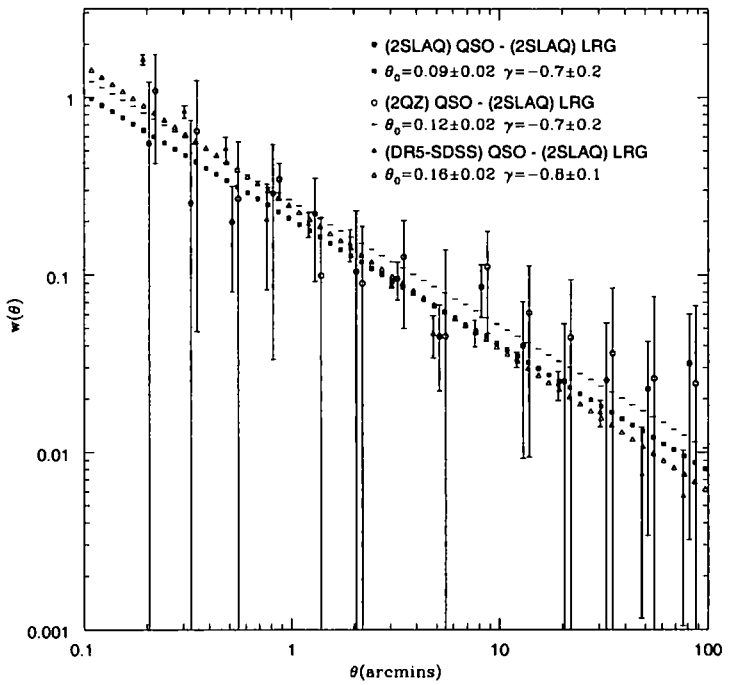

Figure 4.5: QSO-2SLAQ (photometric) LRG cross-correlation results. The 2SLAQ QSO-2SLAQ (photometric) LRG results (filled circles) have been corrected for fibre collisions. We have also plotted the fits to these measurements.

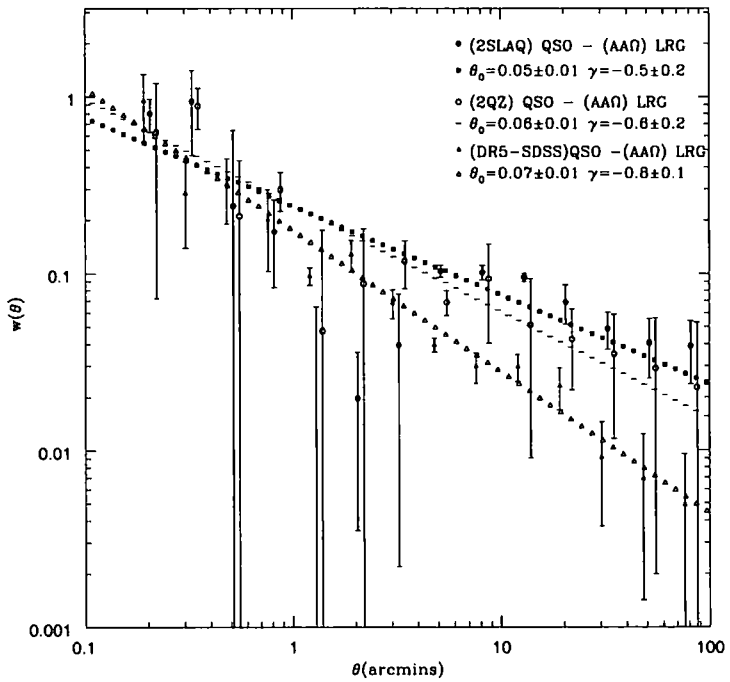

Figure 4.6: QSO-AAOmega (photometric) LRG cross-correlation results. We have also plotted the fits to these measurements.

2SLAQ). In both cases, triangles show the results using SDSS QSOs, filled circles using 2SLAQ QSOs and open circles using 2QZ QSOs. The θ_0 and r_0 values from the fits (in the range 0.1′-100′) to these measurements are also shown. We note, that both results show a slightly steeper slope for the brightest QSO sample (SDSS, $\gamma = -0.8 \pm 0.1$) compared to the other QSO samples.

Comparing our $w(\theta)$ results from 2QZ QSO-spectroscopic LRGs (triangles of Fig. 4.4) with those from 2QZ QSO-photometric LRGs (open circles of Fig. 4.5) we note that the latter shows a positive signal whereas the former shows no signal, at least on small scales, and appears to be noisy. This is probably because the 2QZ QSO sample is much larger ($\approx 3\times$) in the photometric LRG area (Table 4.2) than it is in the spectroscopic LRG area (Table 4.1).

4.4 3-D cross-correlation functions, $\xi(s)$ and $\xi(r)$

In this Section we present our results for the QSO-LRG redshift-space cross-correlation function, $\xi(s)$, for different QSO and LRG samples. Fig. 4.7 shows the results using our 2SLAQ QSO-2SLAQ (spectroscopic) LRG samples. Our 2SLAQ QSO sample consists of QSOs with the same average redshift as the 2SLAQ LRGs, i.e. $0.35 \leq z \leq 0.75$. Filled circles show the results when the fibre collision effect is not taken into account and open circles show the results when the fibre collision is taken into consideration, as described in the previous Section. As we can see the effect is bigger on small scales (i.e. $s \leq 3\mathrm{h}^{-1}\mathrm{Mpc}$) than it is on larger scales.

We also repeat this redshift-space cross-correlation measurement using the 2QZ and the SDSS QSO samples, both within a redshift range of $0.35 \leq z \leq 0.75$, and spectroscopic 2SLAQ LRGs. As already mentioned, the 2QZ survey has a brighter magnitude limit than 2SLAQ, i.e. $b_J = 20.85$ instead of $b_J = 21.85$. The brightest of the three samples is that from SDSS ($i_{AB} < 19.1$). Our results are shown in Fig. 4.8. On small scales, $\leq 5\mathrm{h}^{-1}\mathrm{Mpc}$ we can see the suppression of $\xi(s)$, due to the non-linear redshift-space distortions (small-scale peculiar velocities, $< w_z^2 >^{1/2}$). The effect is less for SDSS, possibly because SDSS uses narrow lines to determine redshifts for QSOs at low redshift and [OIII] 5007 is seen for the whole redshift

Table 4.3: r_0 and γ values from the fits on the QSO-2SLAQ (photometric) LRG $\xi(r)$ measurements.

	$\xi(r)$		
	photometric 2SLAQ LRGs		
	2SLAQ QSOs	2QZ QSOs	SDSS QSOs
r_0	$7.5^{+0.3}_{-0.3}$	$8.0^{+0.4}_{-0.4}$	$7.0^{+0.3}_{-0.3}$
$-\gamma$	$1.7^{+0.2}_{-0.2}$	$1.7^{+0.2}_{-0.2}$	$1.8^{+0.1}_{-0.1}$

range in question for SDSS spectra. 2SLAQ/2QZ redshifts are purely template fits and so will instead be driven by the broad lines. On larger scales the results are in good statistical agreement, regardless of the brightness of the QSO sample. This agreement is also confirmed by the fits to these measurements (Table 4.4). Since the results are affected by the 'Finger of god' effect on small scales, the fits are applied on $5-25\mathrm{h}^{-1}$Mpc scales. The agreement between the $\xi(s)$ results, suggests that QSO bias is also independent of QSO luminosity since the QSOs span a range of more than 2 magnitudes at fixed redshift.

To further check our observations, we use Limber's formula (Limber 1953, Rubin 1954) and following Phillipps et al. (1978) we calculate the real-space cross-correlation function, $\xi(r)$ from our previous (Section 4.3.3) $w(\theta)$ measurements from the photometric LRG samples. The fits appear in Fig. 4.9 and in Table 4.3. The black solid line ($r_0 = 7.5 \pm 0.3, \gamma = 1.7 \pm 0.2$) is the fit using the 2SLAQ QSO-2SLAQ LRG sample, the dotted line ($r_0 = 8.0 \pm 0.4, \gamma = 1.7 \pm 0.2$) using the 2QZ QSO-2SLAQ LRG sample and the dashed line ($r_0 = 7.0 \pm 0.3, \gamma = 1.8 \pm 0.1$) using the SDSS QSO-2SLAQ LRG sample. The blue lines are the fits using our QSO samples with AAOmega LRGs. Once again, we note that the results are approximately independent of the luminosity of the QSO sample.

In Fig. 4.8 we have plotted the fits from the QSO-2SLAQ (photometric) LRGs with the results from the spectroscopic 2SLAQ LRGs already discussed. This is a comparison between $\xi(r)$ (photometric) and $\xi(s)$ (spectroscopic) results. As we can see from Fig. 4.8 the agreement is not good at small scales ($< 5\mathrm{h}^{-1}$Mpc) but this

Table 4.4: s_0 and γ values from the fits on the QSO-2SLAQ (spectroscopic) LRG $\xi(s)$ measurements, on scales of 5-25h^{-1}Mpc.

	$\xi(s)$		
	spectroscopic 2SLAQ LRGs		
	2SLAQ QSOs	2QZ QSOs	SDSS QSOs
s_0	$8.2^{+0.1}_{-0.1}$	$8.0^{+0.3}_{-0.1}$	$7.5^{+0.3}_{-0.2}$
$-\gamma$	$1.6^{+0.2}_{-0.1}$	$1.7^{+0.2}_{-0.1}$	$1.8^{+0.2}_{-0.3}$

is due to non-linear redshift-space distortions (Finger of god) that affect $\xi(s)$ but not the $\xi(r)$ measurements on small scales. A fairer comparison can be made on larger scales. Taking into account the 'Kaiser boost' (see equation 4.14, ≈ 1.25 for $\beta = 0.35$, as we shall see next) we compare the fits (Tables 4.3 and 4.4) to the QSO-2SLAQ (photometric) LRGs and QSO-2SLAQ (spectroscopic) LRGs, respectively. We see that they are in reasonable agreement.

Finally, in Fig. 4.10 we compare our redshift-space measurements for QSO-LRGs with QSO-QSO (da Ângela et al. 2008) and LRG-LRG (Ross et al. 2007) measurements. Triangles show the 2QZ+2SLAQ QSO $\xi(s)$ results, filled circles show the 2SLAQ LRG $\xi(s)$ results and open circles show our results for the 2SLAQ QSO-2SLAQ (spectroscopic) LRG redshift-space cross-correlation. The fact that QSO-QSO and QSO-LRG results appear flatter than the LRG-LRG ones, on small scales, may be explained by the intrinsic dispersion and the redshift errors, which are higher for broad emission line QSOs than for LRGs (≈ 650kms^{-1} vs. ≈ 300kms^{-1}). This would affect mostly the QSO-QSO results and the least the LRG-LRG results, as observed. The QSO-LRG measurements should then lie in between the QSO-QSO and LRG-LRG measurements, as they do. On larger scales (≥ 5h^{-1}Mpc) the QSO-QSO correlation amplitude appears lower than the LRG-LRG one. This implies that the QSO bias is smaller than the LRG bias. Assuming the model $\xi_{mm} = \frac{\xi_{QL}}{b_Q b_L}$ (see Section 4.7.2), the agreement between the QSO-LRG amplitude and the LRG-LRG amplitude would imply that $b_Q \approx b_L$. So the overall conclusion is that $b_Q \lesssim b_L$. These issues will be further discussed in Section 4.8.

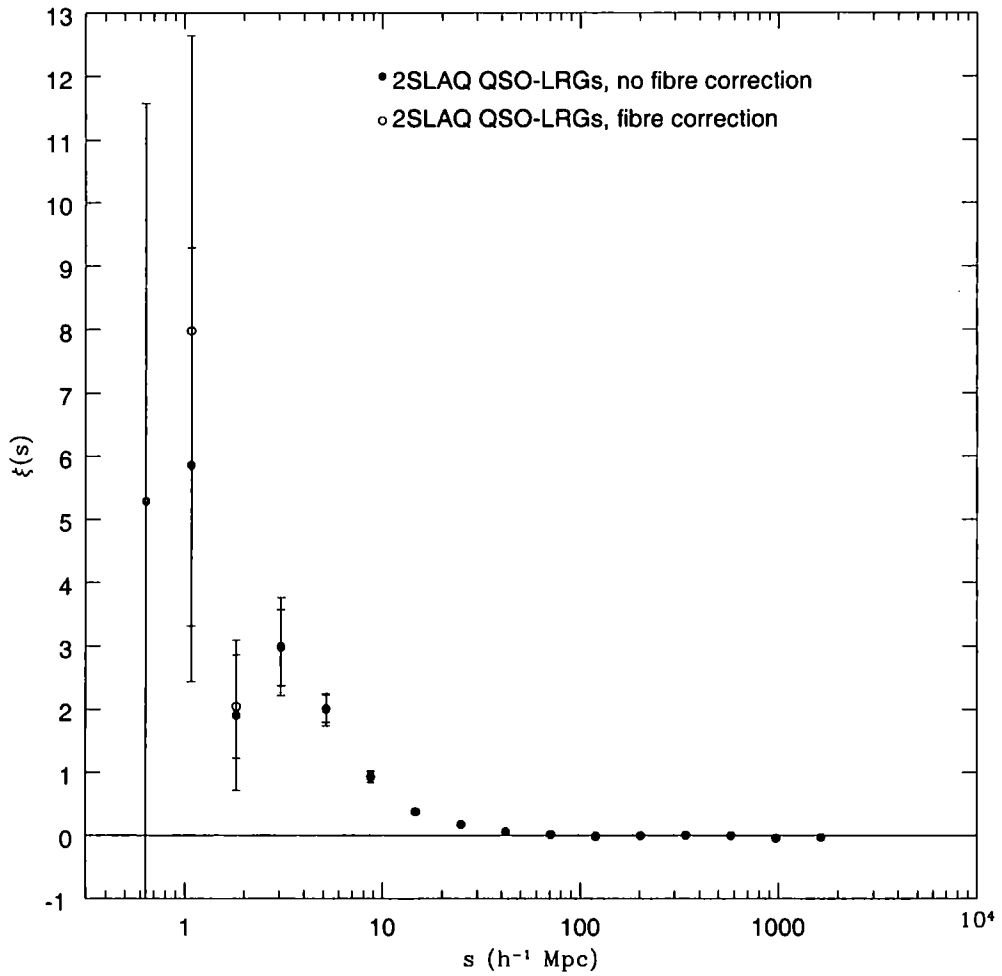

Figure 4.7: 2SLAQ QSO-2SLAQ (spectroscopic) LRG redshift-space cross-correlation results. Filled circles show the results when the fibre collision effect is not taken into account and open circles show the results when the fibre collision is taken into consideration. As we can see the effect is bigger on small scales (i.e. $s \leq 3\mathrm{h}^{-1}\mathrm{Mpc}$) than it is on larger scales.

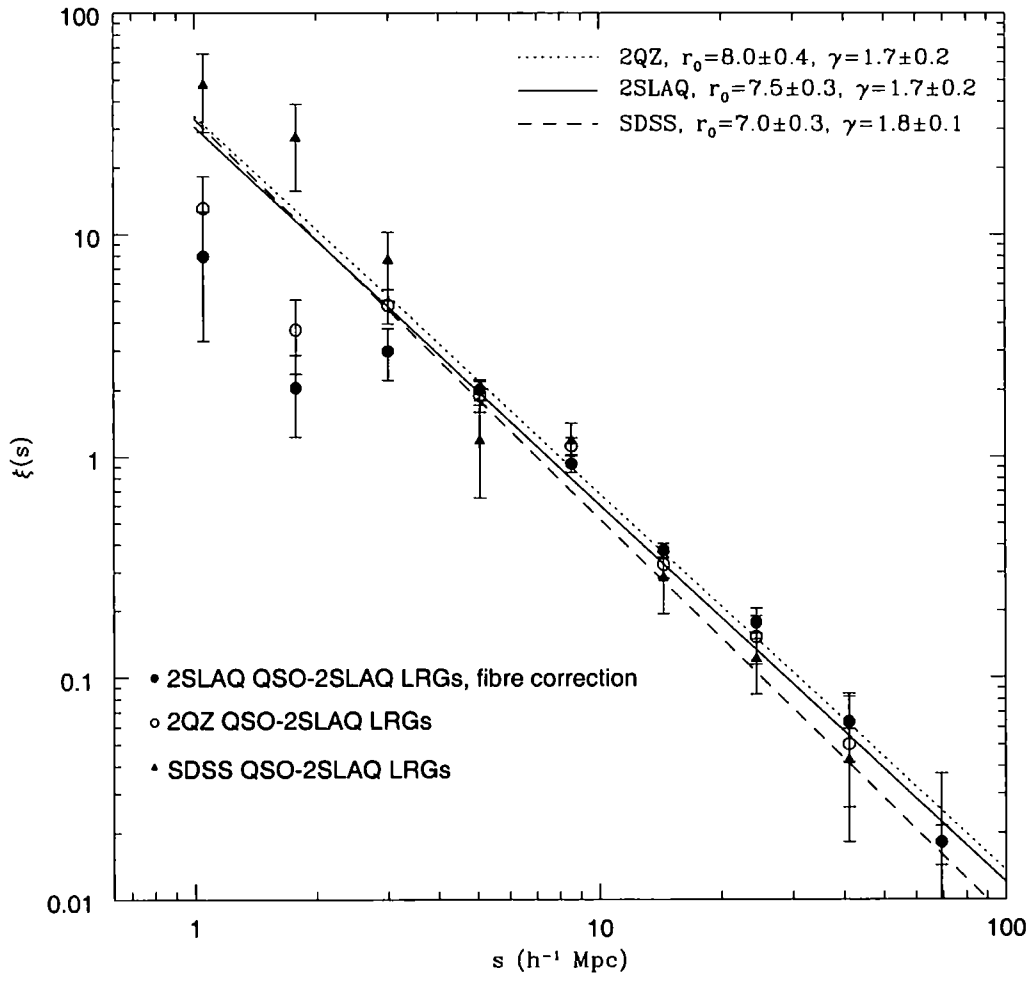

Figure 4.8: QSO-2SLAQ LRG redshift-space cross-correlation results. Filled circles show the results when using 2SLAQ QSOs, open circles using 2QZ QSOs and triangles using SDSS DR5 QSOs ($0.35 \leq z \leq 0.75$, in all cases). All measurements have been made with spectroscopic 2SLAQ LRGs. The lines show the $\xi(r)$ fits from the photometric samples, which appear to be in agreement with the spectroscopic results.

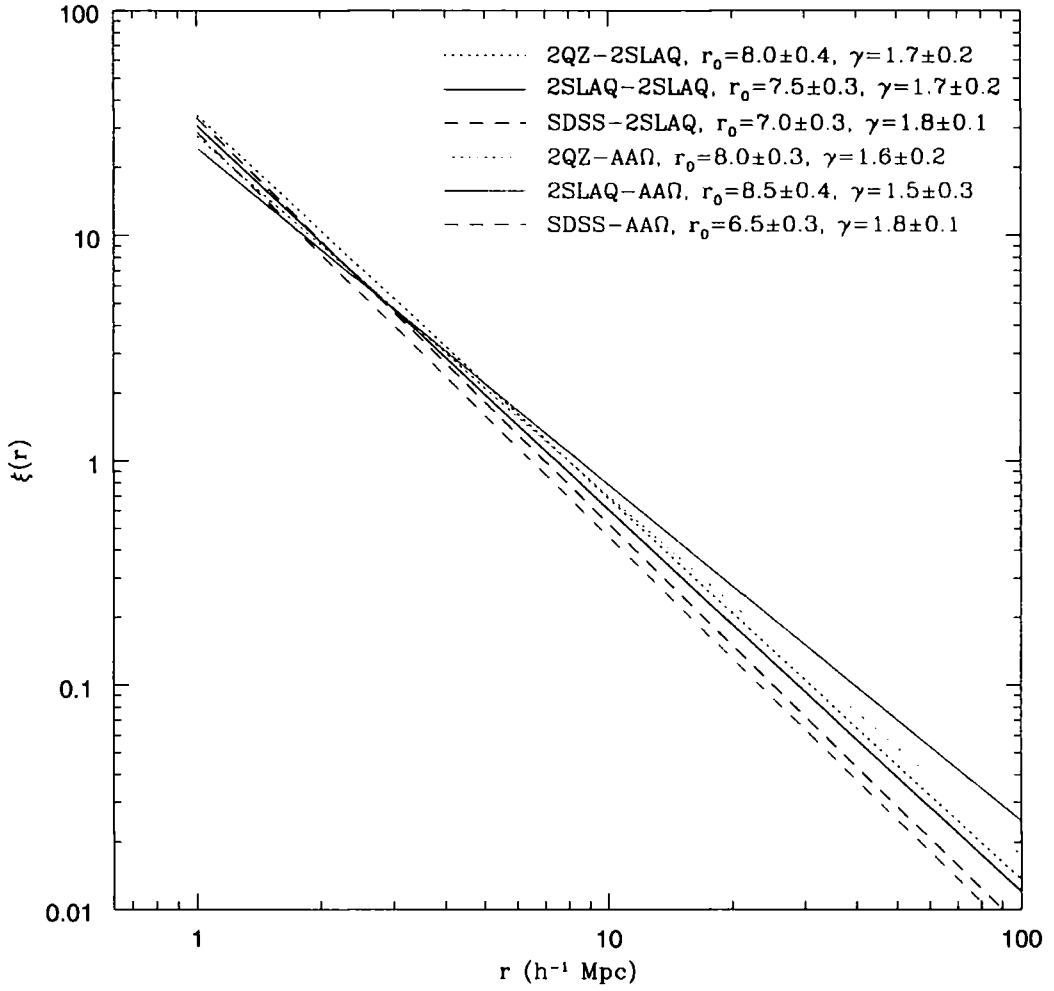

Figure 4.9: $\xi(r)$ fits via Limber's formula following Phillipps et al. 1977, of our $w(\theta)$ measurements from spectroscopic QSO samples with photometric 2SLAQ and AAOmega LRG samples.

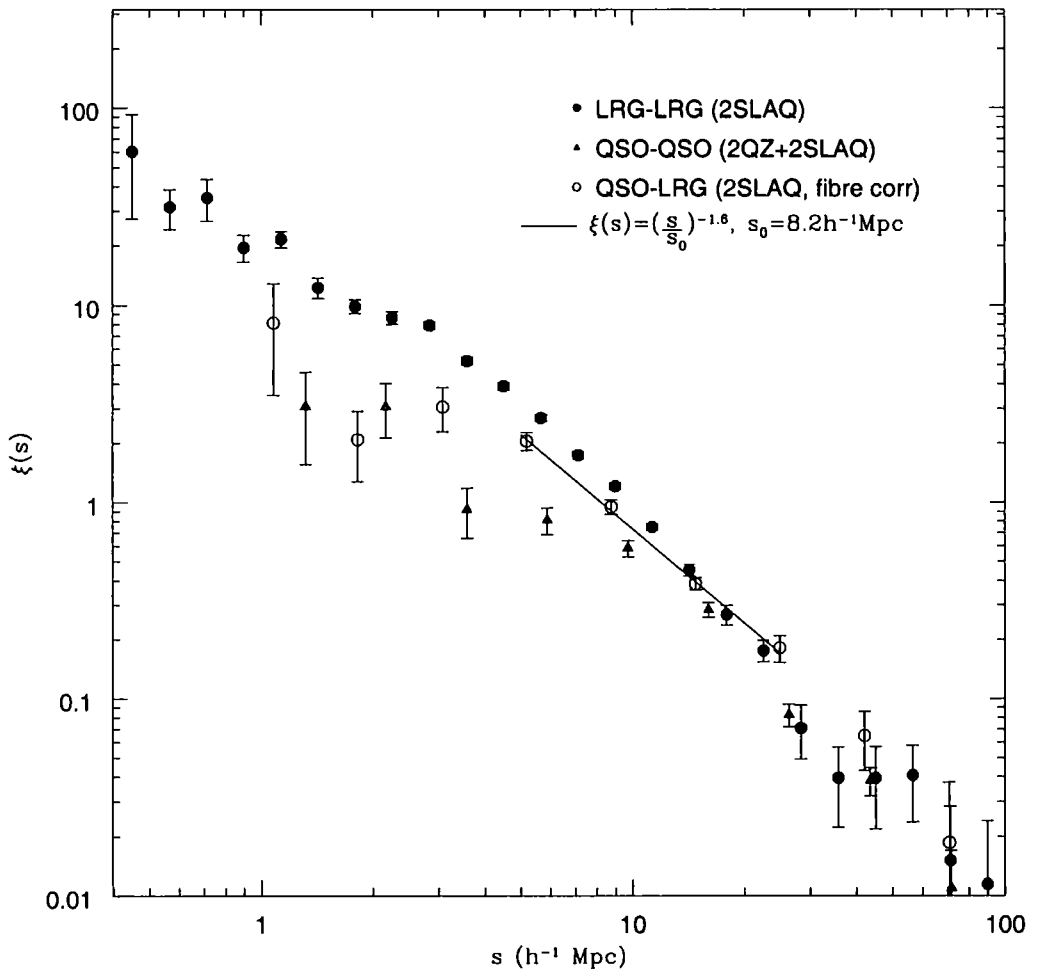

Figure 4.10: Comparison of $\xi(s)$ measurements for QSO-LRGs with QSO-QSO (da Ângela et al. (2005) and LRG-LRG (Ross et al. 2006) measurements. Triangles are the 2QZ+2SLAQ QSO $\xi(s)$ results ($0.3 < z < 2.2$), filled circles show the 2SLAQ LRG $\xi(s)$ results and open circles show the results for the 2SLAQ QSO-2SLAQ LRG redshift-space cross-correlation. The solid line shows our χ^2 fit to the data from $5 - 25\mathrm{h}^{-1}\mathrm{Mpc}$, which gives $s_0 = 8.2 \pm 0.1\mathrm{h}^{-1}\mathrm{Mpc}$ and $\gamma = 1.6^{+0.2}_{-0.1}$.

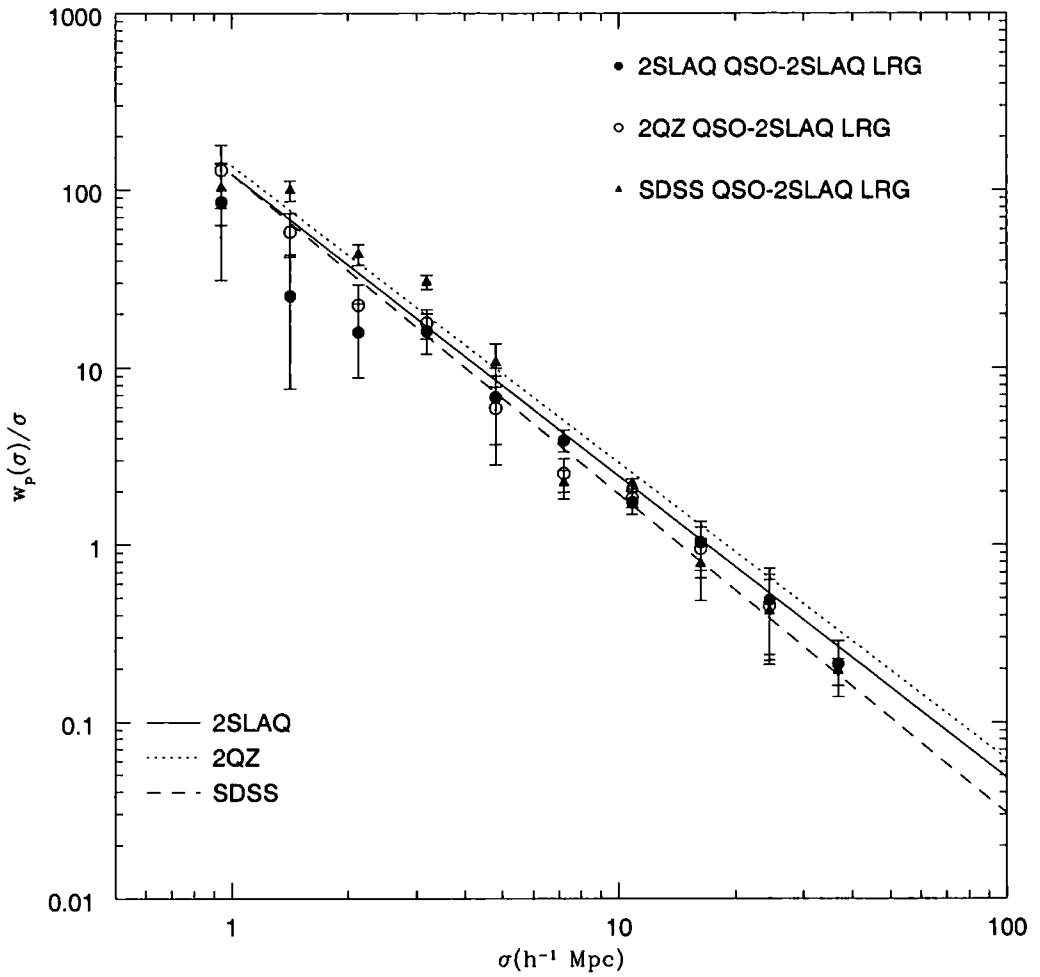

Figure 4.11: The semi-projected cross-correlation function results for the 2SLAQ QSOs-2SLAQ (spectroscopic) LRGs (filled circles), the 2QZ QSOs-2SLAQ (spectroscopic) LRGs (open circles) and SDSS QSOs-2SLAQ (spectroscopic) LRGs (triangles). We have also plotted the fits from the $w(\theta)$ measurements of the photometric 2SLAQ LRG sample, using Limber's formula.

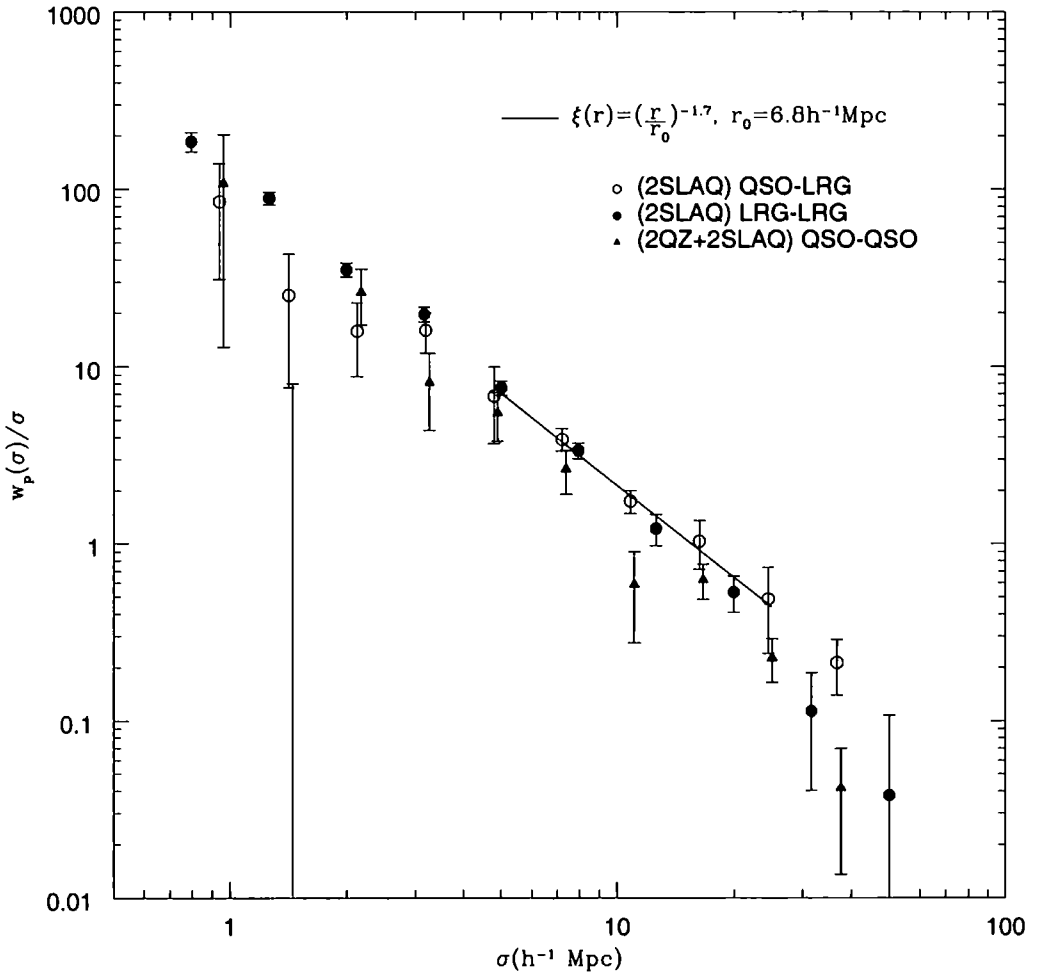

Figure 4.12: The semi-projected correlation function results for the (2QZ+2SLAQ) QSO (open circles) and the 2SLAQ LRG-LRG (triangles) from da Ângela et al. (2005) and Ross et al. (2007), respectively. The solid line shows our χ^2 fit to the data from $5 - 25h^{-1}$Mpc, which gives $r_0 = 6.8^{+0.1}_{-0.3}h^{-1}$Mpc and $\gamma = 1.7^{+0.2}_{-0.3}$.

4.5 The semi-projected cross-correlation function

If s_1 and s_2 are the distances of two objects 1, 2, measured in redshift-space, and θ the angular separation between them, then σ and π are defined as

$$\pi = (s_2 - s_1), \text{along the line-of-sight} \tag{4.3}$$

$$\sigma = \frac{(s_2 + s_1)}{2}\theta, \text{across the line-of-sight.} \tag{4.4}$$

The effects of redshift distortion appear only in the radial component, π; integrating along the π direction, we calculate what is called the projected correlation function, $w_p(\sigma)$

$$w_p(\sigma) = 2\int_0^\infty \xi(\sigma, \pi)d\pi. \tag{4.5}$$

In our case we take the upper limit of the integration to be equal to $\pi_{max} = 70\mathrm{h}^{-1}\mathrm{Mpc}$. This limit has been chosen to minimise the effect of the small-scale peculiar velocities and redshift errors (da Ângela et al.). If we include very large scales, the signal becomes dominated by noise and, on the other hand, if we take our measurements on very small scales the amplitude will be underestimated. Now, since $w_p(\sigma)$ describes the real-space clustering, the last equation can be written in terms of the real-space correlation function, $\xi(r)$, (Davis & Peebles, 1983), i.e.

$$w_p(\sigma) = 2\int_\sigma^{\pi_{max}} \frac{r\xi(r)}{\sqrt{(r^2 - \sigma.^2)}}dr \tag{4.6}$$

Calculating the projected cross-correlation function $w_p(\sigma)$ will help us estimate the real-space cross-correlation function, $\xi(r)$. The r_0 from the $w_p(\sigma)/\sigma$ fits is estimated using the following equation:

$$\frac{w_p(\sigma)}{\sigma} = \left(\frac{r_0}{\sigma}\right)^\gamma \frac{\Gamma(\frac{1}{2})\Gamma(\frac{\gamma-1}{2})}{\Gamma(\frac{\gamma}{2})}, \tag{4.7}$$

where $\Gamma(x)$ is the Gamma function.

Fig. 4.11 shows our $w_p(\sigma)/\sigma$ measurements from the different QSO samples cross-correlated with the spectroscopic 2SLAQ LRGs. Filled circles show the results

using 2SLAQ QSOs-2SLAQ LRGs, open circles using 2QZ QSOs-2SLAQ LRGs and triangles SDSS QSOs-2SLAQ LRGs. We see that the semi-projected cross-correlation function confirms our results in redshift-space, i.e. the measurements are in agreement regardless of the luminosity of the QSO sample. This can also be confirmed by the fits to these measurements shown in Table 4.5. As for the $\xi(s)$ case, we also include the fits from the $w(\theta)$ measurements of the photometric 2SLAQ LRG sample, using Limber's formula. The photometric fits are, again, in good agreement with the spectroscopic measurements, further supporting the idea that the cross-clustering is independent of QSO luminosity.

Fig. 4.12 shows the $w_p(\sigma)/\sigma$ results for the 2SLAQ QSO-LRGs (filled circles). As in the previous Section, we have also included the semi-projected correlation function results for the (2QZ+2SLAQ) QSO (open circles) and the 2SLAQ LRG-LRG (triangles) from da Ângela et al. (2006) and Ross et al. (2007), respectively. We note that, at small scales ($\leq 3\mathrm{h}^{-1}\mathrm{Mpc}$), although the results are noisier than for the $\xi(s)$ measurements, QSO-LRG and QSO-QSO measurements have a slightly smaller amplitude than the LRG-LRG one but to a much lesser degree than in the $\xi(s)$ measurements. This confirms our previous explanation that the amplitude difference in the redshift-space measurements at small scales is due to the QSO redshift errors, an effect which does not affect the $w_p(\sigma)/\sigma$ measurements. On larger scales, $w_p(\sigma)/\sigma$ measurements confirm our previous observations for lower QSO-QSO amplitude comparing with the QSO-LRG and the LRG-LRG amplitude. Finally, the solid line shows our χ^2 fit to the QSO-LRG data from $5 - 25\mathrm{h}^{-1}\mathrm{Mpc}$ (for consistency reasons with the $\xi(s)$ fits), which gives $r_0 = 6.8^{+0.1}_{-0.3}\mathrm{h}^{-1}\mathrm{Mpc}$ and $\gamma = 1.7^{+0.2}_{-0.3}$. This is similar to the (2SLAQ) LRG-LRG auto-correlation amplitude ($r_0 = 7.45 \pm 0.35\mathrm{h}^{-1}\mathrm{Mpc}$) and both are higher than the (2QZ+2SLAQ) QSO-QSO amplitude ($r_0 \simeq 5.0\mathrm{h}^{-1}\mathrm{Mpc}$) at $z = 1.4$.

4.6 The real-space cross-correlation function

Using the results from the projected cross-correlation function, described in the previous Section, and following Saunders et al. 1992, we can calculate the real-

Table 4.5: r_0 and γ values from the fits on the $w_p(\sigma)/\sigma$ measurements, on scales of 5-25h^{-1}Mpc.

$w_p(\sigma)/\sigma$			
	spectroscopic 2SLAQ LRGs		
	2SLAQ QSOs	2QZ QSOs	SDSS QSOs
r_0	$6.8^{+0.1}_{-0.3}$	$6.0^{+0.4}_{-0.2}$	$6.3^{+0.3}_{-0.1}$
$-\gamma$	$1.7^{+0.2}_{-0.3}$	$1.5^{+0.1}_{-0.2}$	$1.8^{+0.1}_{-0.1}$

Table 4.6: r_0 and γ values from the fits on the $\xi(r)$ measurements, on scales of 5-25h^{-1}Mpc.

$\xi(r)$			
	spectroscopic 2SLAQ LRGs		
	2SLAQ QSOs	2QZ QSOs	SDSS QSOs
r_0	$7.0^{+0.2}_{-0.1}$	$7.0^{+0.3}_{-0.3}$	$5.5^{+0.4}_{-0.2}$
$-\gamma$	$2.1^{+0.2}_{-0.1}$	$1.6^{+0.1}_{-0.1}$	$2.3^{+0.2}_{-0.3}$

space cross-correlation function, $\xi(r)$, as follows:

$$\xi(r) = -\frac{1}{\pi}\int_r^\infty \frac{d\omega(\sigma)/d\sigma}{\sqrt{(\sigma^2 - r^2)}} d\sigma. \tag{4.8}$$

Assuming a step function for $w_p(\sigma) = w_i$,

$$\xi(\sigma_i) = -\frac{1}{\pi}\sum_{j\geq i} \frac{\omega_{j+1} - \omega_j}{\sigma_{j+1} - \sigma_j} ln\left(\frac{\sigma_{j+1} + \sqrt{\sigma_{j+1}^2 - \sigma_i^2}}{\sigma_j + \sqrt{\sigma_j^2 - \sigma_i^2}}\right), \tag{4.9}$$

for $r = \sigma_i$.

The QSO-2SLAQ (spectroscopic) LRG real-space results are shown in Fig. 4.13. In the same Figure we have also plotted the $\xi(r)$ fits from the QSO-photometric LRG $w(\theta)$ measurements, described in Section 4.4. All the samples seem to give consistent results although, as already mentioned, these $\xi(r)$ measurements from the spectroscopic samples are very noisy and no significant conclusions can be drawn.

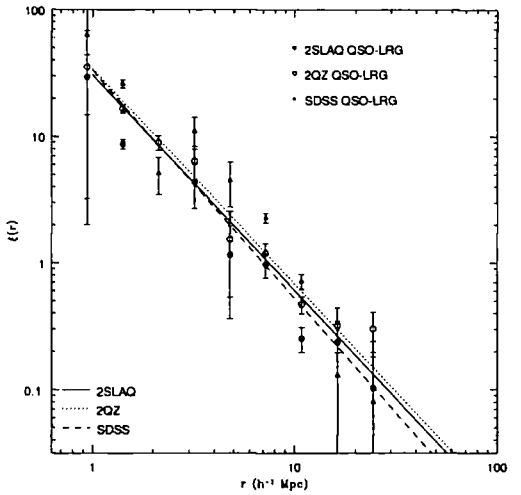

Figure 4.13: The real-space cross-correlation function, $\xi(r)$, results for our different samples. The dashed lines show the fits from the QSO-photometric LRG $w(\theta)$ measurements.

Finally, Table 4.6 shows the r_0 and γ values from the fits to the spectroscopic samples, on scales of $5 \leq r \leq 25 h^{-1}$Mpc.

4.7 Contraints on β from redshift-space distortions

4.7.1 The $\xi(\sigma, \pi)$ cross-correlation function

As already noted, QSO-LRG velocity dispersion and their dynamical infall into higher density regions are two mechanisms that distort the spherically symmetric clustering pattern in real space. We measure the $\xi(\sigma, \pi)$ cross-correlation function in the case of 2SLAQ, 2QZ and SDSS QSOs with the (spectroscopic) 2SLAQ LRGs. The purpose is to use the shape of the $\xi(\sigma, \pi)$ and our previous ξ measurements in order to model the redshift-space distortions and put constraints on β. Fig. 4.14 shows a comparison between our 2SLAQ QSO-2SLAQ LRG $\xi(\sigma, \pi)$ (solid line)

results and the results using our model I (dashed line, see below). As we can see, model I is in very good agreement with the data both on small and large scales.

4.7.2 Description of $\xi(\sigma, \pi)$ models

To place constraints on the infall parameter we model the redshift-space distortions measured above. First, we define our models for bias, b, and infall parameter β,

$$\xi_{mm} = \frac{\xi_{QL}}{b_Q b_L}, \tag{4.10}$$

where b_Q and b_L are the QSO and LRG bias, respectively, given by

$$b_Q \simeq \frac{\Omega_m^{0.6}}{\beta_Q}, b_L \simeq \frac{\Omega_m^{0.6}}{\beta_L}, \tag{4.11}$$

where β_Q and β_L are the QSO and LRG infall parameter, respectively and Ω_m is given in a flat universe as

$$\Omega_m(z) = \frac{\Omega_m^0(1+z)^3}{\Omega_m^0(1+z)^3 + \Omega_\Lambda^0}. \tag{4.12}$$

In our analysis in this Section we shall use two models. **Model I** is the one used in da Ângela et al. modified accordingly to match our cross-correlation analysis, instead of the auto-correlation (QSO-QSO) which was used in that study.

In general, the power spectrum in real and redshift space is given by (Kaiser 1987)

$$P_s(k) = (1 + \beta(z)\mu_k^2)^2 P_r(k), \tag{4.13}$$

and the similar relation between $\xi(r)$ and $\xi(s)$ is (Hamilton 1993)

$$\xi(r) = \frac{\xi(s)}{1 + \frac{2}{3}\beta(z) + \frac{1}{5}\beta(z)^2}, \tag{4.14}$$

where $P_s(k)$ is the power-spectrum in redshift-space, $P_r(k)$ is the power-spectrum in real-space, and μ_k is the cosine of the angle between the wavevector $\mathbf{k}$ and the line-of-sight. Equation 4.13 can also take the form,

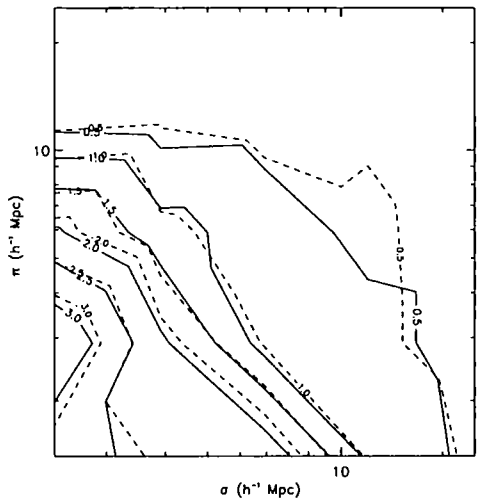

Figure 4.14: A comparison between our 2SLAQ QSO-2SLAQ LRG $\xi(\sigma,\pi)$ (solid line) results and the results using our Model I (dashed line). As we can see, model I is in very good agreement with the data both on small and large scales.

$$\begin{aligned}\xi(\sigma,\pi) &= \left(1+\frac{2}{3}\beta(z)+\frac{1}{5}\beta(z)^2\right)\xi_0(r)P_0(\mu)\\ &\left(-\frac{4}{3}\beta(z)+\frac{4}{7}\beta(z)^2\right)\xi_2(r)P_2(\mu)\\ &+\frac{8}{35}\beta(z)^2\xi_4(r)P_4(\mu).\end{aligned} \tag{4.15}$$

μ is now the cosine of the angle between r and π, $P_l(\mu)$ are the Legendre polynomials of order l and $\xi_0(r)$, $\xi_2(r)$ and $\xi_4(r)$ being the monopole, quadrupole and hexadecapole components of the linear $\xi(r)$.

In our analysis there are two infall parameters, β_Q and β_L, one for QSOs and one for LRGs. Therefore, equations 4.14, 4.13 and 4.15 (Jiang, priv. communication) should be modified as follows:

$$\xi(r) = \frac{\xi(s)}{1+\frac{1}{3}(\beta_Q(z)+\beta_L(z))+\frac{1}{5}\beta_Q(z)\beta_L(z)}, \tag{4.16}$$

$$P_s(k) = (1+\beta_Q(z)\mu_k^2)(1+\beta_L(z)\mu_k^2)P_r(k), \tag{4.17}$$

$$\begin{aligned}\xi(\sigma,\pi) &= \left(1+\frac{1}{3}(\beta_Q(z)+\beta_L(z))+\frac{1}{5}\beta_Q(z)\beta_L(z)\right)\xi_0(r)P_0(\mu)\\ &\left(-\frac{2}{3}(\beta_Q(z)+\beta_L(z))+\frac{4}{7}\beta_Q(z)\beta_2(z)\right)\xi_2(r)P_2(\mu)\\ &+\frac{8}{35}\beta_Q(z)\beta_L(z)\xi_4(r)P_4(\mu),\end{aligned} \tag{4.18}$$

The problem with this formalism is that the model only constrains the sum of the infall parameters, i.e. $\beta_Q + \beta_L$, and not to each of them individually. So, in what follows we keep β_L constant using the value found by Ross et al., $\beta_L = 0.45 \pm 0.05$, and use the model to constrain the QSO infall parameter β_Q.

Now, the magnitude of the elongation along the π-direction of the $\xi(\sigma,\pi)$ plot caused by the peculiar velocity of the object is denoted by $< \omega_z^2 >^{1/2}$, which can be expressed by a Gaussian (Ratcliffe et al. 1996), as

$$f(\omega_z) = \frac{1}{\sqrt{2\pi} < \omega_z^2 >^{1/2}} exp(-\frac{1}{2}\frac{|\omega_z|^2}{< \omega_z^2 >^{1/2}}). \tag{4.19}$$

To include the small scale redshift-space effects due to the random motions of galaxies, we convolve the $\xi(\sigma,\pi)$ model with the peculiar velocity distribution, given by equation 4.19. Then, $\xi(\sigma,\pi)$ is given by

$$\xi(\sigma,\pi) = \int_{-\infty}^{+\infty} \xi'(\sigma,\pi-\omega_z(1+z)/H(z))f(\omega_z)\mathrm{d}\omega_z, \tag{4.20}$$

where $\xi'(\sigma,\pi-\omega_z(1+z)/H(z))$ is given by equation 4.15.

Finally, we exploit the Alcock–Paczynski effect (Alcock & Paczynski 1979) which says that the ratio of observed angular size to radial size varies with cosmology (isotropic clustering). If we assume that the cluster is isotropic, then we can constrain the cosmological parameters by requiring that they produce equal tangential and radial sizes. In our case the angular and the radial size are σ and π. Following the application of the test and assumed cosmology as used by da Ângela et al. and using their fitting procedure we obtain our results (see below). In particular, we use the γ values from our fits to $\xi(s)$, let r_0 and the velocity dispersion vary as free parameters and compute the χ^2 values for each $\Omega_m^0 - \beta(z)$ pair.

The second model (**model II**) is as follows. $\xi(\sigma,\pi)$ is now defined as (Peebles 1980, Hoyle 2000)

$$1+\xi(\sigma,\pi)=\int_{-\infty}^{+\infty}(1+\xi(r))f(\omega_z)\mathrm{d}\omega_z, \tag{4.21}$$

where the $f(\omega_z)$ is given, as before, by equation 4.19. Next we introduce the infall velocity of the galaxies, $v(r_z)$, as a function of the real-space separation along the π direction, r_z. This can be derived from the equation of conservation of particle pairs, which are within a comoving separation r from a mass particle, i.e. (Peebles 1980)

$$\frac{\delta}{\delta t}\int_0^r x^2\xi^m(x,t)\mathrm{dx}+\frac{1}{\alpha(\mathrm{t})}\mathrm{r}^2(1+\xi^{\mathrm{m}}(\mathrm{r},\mathrm{t}))v(\mathrm{r},\mathrm{t})=0, \tag{4.22}$$

where $a(t)$ is the scale factor. Assuming that $\xi(r)$ is described by a power law model, we solve the above equation to find the infall velocity of the particles, which is

$$v(r_z)=-\frac{2}{3-\gamma}\Omega_m(z)^{0.6}H(z)r_z\frac{\xi_{QL}(r)}{b_Q b_L+\xi_{QL}(r)}. \tag{4.23}$$

We now modify equation 4.21 to include the effects of the bulk motions

$$1+\xi(\sigma,\pi)=\int_{-\infty}^{+\infty}(1+\xi(r))f(\omega_z(1+z)-v(r_z))\mathrm{d}\omega_z. \tag{4.24}$$

This is the model II $\xi(\sigma,\pi)$; we then follow the same implementation of the "Alcock-Paczynski" effect and fitting procedure as for model I. As in model I, we keep b_L constant, using the same value as above (Ross et al.), i.e. $\beta_L=0.45\pm0.05$ and $b_L=1.66\pm0.35$.

4.7.3 Results

We now use our $\xi(\sigma,\pi)$ measurements from the previous Section and the s_0 and γ values from the $\xi(s)$ fits shown in Table 4.4 to put constraints on β_Q and b_Q and $<\omega_z^2>^{1/2}$, for each of the QSO samples. The results are shown in Table 4.7 and in Fig. 4.15.

Comparing the results from both models from the three different QSO samples associated with the same spectroscopic 2SLAQ LRG sample, we note that model

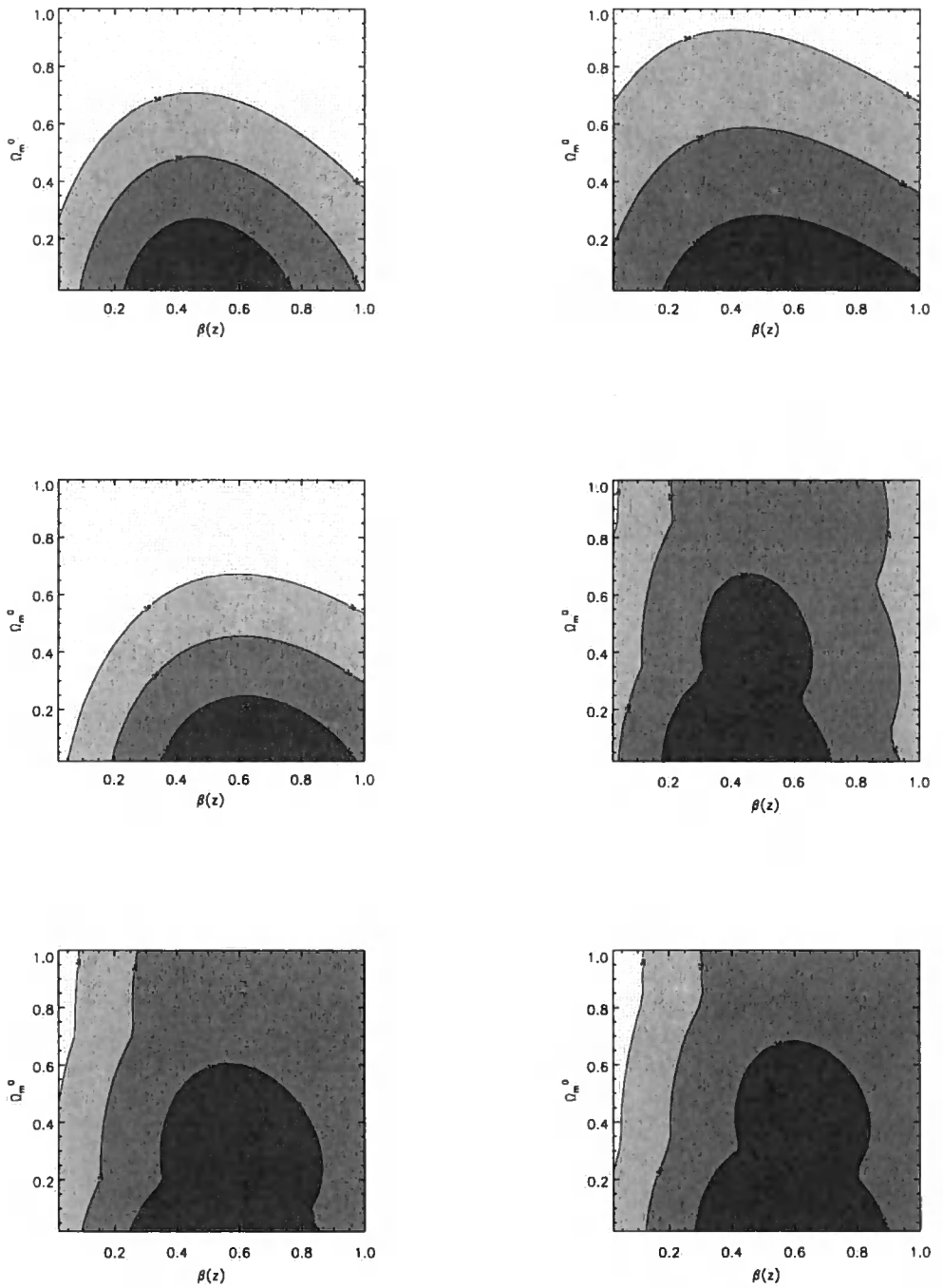

Figure 4.15: Likelihood contours of $\Omega_m^0 - \beta(z = 0.55)$ for QSO−2SLAQ LRGs, using model I (left) and II (right). The QSO samples are from (top to bottom) 2SLAQ, 2QZ and SDSS. The best fit values are shown in Table 4.7.

Table 4.7: QSO b_Q, β_Q and $< \omega_z^2 >^{1/2}$ measurements from modelling the redshift-space distortions.

	QSO b_Q and β_Q					
	model I			model II		
	2SLAQ	2QZ	SDSS	2SLAQ	2QZ	SDSS
$b_Q(\simeq \frac{\Omega_m^{0.6}}{\beta_Q})$	$1.66^{+1.58}_{-0.69}$	$1.36^{+1.41}_{-0.67}$	$1.25^{+0.88}_{-0.46}$	$1.87^{+2.28}_{-0.83}$	$1.25^{+1.74}_{-0.37}$	$1.15^{+1.11}_{-0.32}$
β_Q	$0.45^{+0.32}_{-0.22}$	$0.55^{+0.53}_{-0.38}$	$0.60^{+0.35}_{-0.25}$	$0.40^{+0.32}_{-0.22}$	$0.60^{+0.25}_{-0.35}$	$0.65^{+0.25}_{-0.37}$
$< \omega_z^2 >^{1/2}$ (kms^{-1})	630	560	670	750	720	710

I gives slightly lower QSO-LRG velocity dispersions than model II, but both are consistent ($\sim$620kms^{-1} and $\sim$ 727kms^{-1}) with the expected $< \omega_z^2 >^{1/2} \simeq$612kms^{-1}, produced by adding in quadrature QSO and LRG velocity dispersions from previous QSO-QSO and LRG-LRG studies, which gave 800kms^{-1} and 330kms^{-1}, respectively. Comparison of b_Q between the different samples (for both models) shows that the results are in good statistical agreement (Table 4.7). The best way to summarise the results is to average them. All six measurements (the three samples and the two models) give an average of $\beta_Q = 0.55 \pm 0.10$ and $b_Q = 1.4 \pm 0.2$ at z=0.55, which is consistent with the values found by da Ângela et al., $\beta_Q = 0.60^{+0.14}_{-0.11}$ and $b_Q = 1.5 \pm 0.2$ at z=1.4 and $b_Q = 1.1 \pm 0.2$ at $z \simeq 0.6$ (see their Fig. 13).

4.8 QSO bias and halo masses

4.8.1 QSO-LRG clustering dependence on luminosity

Previous attempts to study the dependence of clustering on luminosity, were not successful because of the redshift-luminosity degeneracy, as higher luminosity QSOs reside at higher redshifts. Combining QSOs with large LRG samples provides the statistical power to break this degeneracy. In this Section, we shall try to examine if and how the QSO-LRG clustering depends on QSO luminosity, at fixed redshift.

We first estimate the average absolute magnitude of each of our QSO samples,

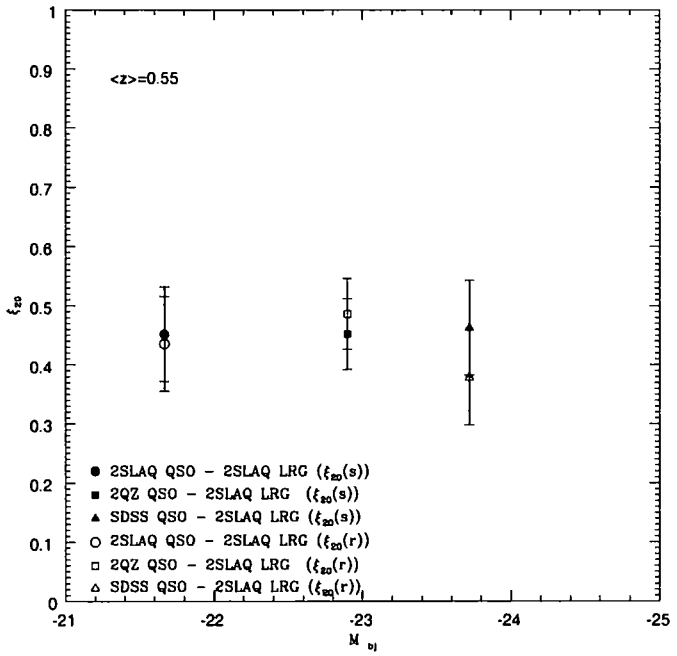

Figure 4.16: ξ_{20} cross-correlation measurements of the three QSO samples with 2SLAQ LRGs. Filled symbols show the results using spectroscopic samples and open symbols using photometric (LRG) samples.

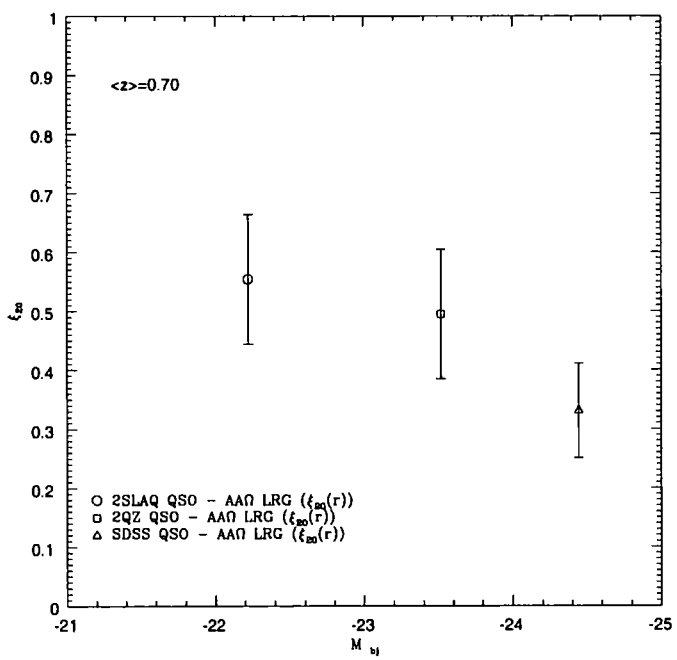

Figure 4.17: ξ_{20} cross-correlation measurements from the three QSO samples with (photometric) AAOmega LRGs.

as follows:

$$M_{b_J} = b_J - 25 - 5log_{10}d_L + 2.5(1+\alpha')\log_{10}(1+z), \quad (4.25)$$

where M_{b_J} is the absolute magnitude of each QSO, b_J (or g) is its apparent magnitude, d_L is the luminosity distance (Mpc) that corresponds to the redshift z and the last term is the k-correction, where we have assumed a QSO spectral index $\alpha' = -1.0$. We should note here that we treat the b_J band (2QZ) as being equivalent to the g band (2SLAQ, SDSS) (Richards et al. 2005).

In order now to check if there is a dependence of QSO-LRG clustering on luminosity we use the integrated correlation function, as a more robust statistical tool (see da Ângela et al.). We calculate the integrated correlation function up to scales of $20h^{-1}$Mpc and normalise the result to the volume contained in a sphere with radius of $20h^{-1}$Mpc:

$$\xi_{20} = \frac{3}{20^3}\int_0^{20} \xi(s)s^2 ds. \quad (4.26)$$

The choice of the radius has been made for two reasons. The first is that the $20h^{-1}$Mpc scale is large enough to apply linear theory (Croom et al. 2005), and redshift-space distortions (finger of god or redshift errors) do not significantly affect the measurements.

In the case of the QSOs-2SLAQ (spectroscopic) LRGs we have estimated ξ_{20} via equation 4.26 using the $\xi(s)$ measurements shown in Fig. 4.8. For the QSO-2SLAQ (photometric) and AAOmega LRGs we have substituted the $\xi(s)$ in equation 4.26 with the $\xi(r)$ fits shown in Fig. 4.9. The results using 2SLAQ LRGs (spectroscopic and photometric) are shown in Fig. 4.16 and using AAOmega LRGs are shown in Fig. 4.17. No conclusion can be drawn about the redshift evolution of the QSO-LRG clustering as the average redshift of the samples is too restricted. Although the ξ_{20} results using the AAOmega LRGs, show some indications that bright QSOs (SDSS) cluster less with LRGs than faint QSOs (2SLAQ), the results using the 2SLAQ LRG samples (both spectroscopic and photometric) stay statistically constant, thus confirming the results in the previous Sections, that the QSO-LRG clustering is independent of QSO luminosity.

4.8.2 QSO bias

Having tested the luminosity dependence of the QSO-LRG clustering, we now investigate the dependence of the QSO bias on the luminosity. Assuming that this bias is independent of scale, we calculate the QSO bias using:

$$b_Q b_L = \frac{\xi_{QL}(r)}{\xi_{mm}} \Rightarrow b_Q \approx \frac{1}{b_L}\frac{\xi_{QL}(r,20)}{\xi_{mm}(r,20)}, \tag{4.27}$$

where ξ_{mm} is the matter real-space correlation function, averaged in $20h^{-1}$Mpc spheres. In the case of QSO-photometric LRGs we use our $\xi(r,20)$ measurements as estimated before. For consistency, we use our $w_p(\sigma)$ measurements (shown in Table 4.8) for the QSO-2SLAQ (spectroscopic) LRGs, since these measurements are less noisy than those for $\xi(r)$. To estimate ξ_{mm} we use the values as estimated by da Ângela et al. (2008). For the case of QSO-AAOmega LRGs $\xi_{mm} = 0.11$ at ($z \approx 0.7$) and in the case of QSO-2SLAQ LRGs $\xi_{mm} = 0.12$ ($z \approx 0.55$). Finally, we calculate the LRG bias for the AAOmega and 2SLAQ, based on the results shown in Table 5 of Ross et al. 2007 (AAOmega: $r_0 = 9.03 \pm 0.93$ and $\gamma = 1.73 \pm 0.08$, 2SLAQ: $r_0 = 7.45 \pm 0.35$ and $\gamma = 1.72 \pm 0.06$). We find, $b_{L(AA\Omega)} = 2.35 \pm 0.20$ and $b_{L(2SLAQ)} = 1.90 \pm 0.08$. The latter is in reasonable agreement with the value found by Ross et al., from redshift-space distortions, $b_{L(2SLAQ)} = 1.66 \pm 0.35$. The derived QSO bias values for each case are shown in Tables 4.8 and 4.9 (as well as the corresponding β_Q values) and in Figures 4.18 and 4.19.

Comparing the values for the QSO biases from the different samples, we note that the QSO biases using 2SLAQ LRG samples show indications for luminosity dependent QSO bias, in the sense that b_Q reduces for higher luminosity samples, at least in the case of spectroscopic 2SLAQ LRGs. The same pattern is repeated when using AAOmega LRG samples. The spectroscopic samples yield lower b_Q values than the photometric samples. This is due to the fact that the amplitude of the $\xi(r)$ measurements of the photometric samples is higher than the amplitude of the $w_p(\sigma)$ measurements of the spectroscopic samples (see Fig. 4.11). Combining the 2SLAQ (photometric and spectroscopic) samples with the photometric AAOmega samples we find $b_Q = 1.90 \pm 0.22$, $b_Q = 1.85 \pm 0.23$ and $b_Q = 1.45 \pm 0.26$, for 2SLAQ, 2QZ and SDSS QSOs, respectively. Comparing now the values for the QSO bias

from the spectroscopic 2SLAQ LRG samples with those obtained in Section 4.7.3, we note that the amplitude results, give an average of $b_Q = 1.5 \pm 0.1$ which is in very good agreement with the average of $b_Q = 1.4 \pm 0.2$ obtained from the redshift-space distortion results. Our measurements find an overall QSO bias of $b_Q \approx 1.5$ at $z = 0.55$ and $M_{bj} \approx -23$.

In Figures 4.18 and 4.19 we have also plotted two points (stars), that are at low redshifts, taken from Fig. 13 of da Ângela et al.. The one with $M_{b_J} \simeq -24.0$ at $z \simeq 0.7$ is in statistical agreement with our b_Q values from the AAOmega LRG samples, at the same mean redshift and brightness. The second one, with $M_{b_J} \simeq -22.9$ at $z \simeq 0.6$, is lower than our b_Q values from 2SLAQ LRG samples, at $z = 0.55$, but statistically not rejected by them (at least not by those from the spectroscopic samples). The overall impression is that our $b_Q \approx 1.5$ at $z = 0.55$ is in agreement with the values found by da Ângela et al., $b_Q = 1.5 \pm 0.2$ at $z = 1.4$ and slightly higher than $b_Q = 1.1 \pm 0.2$ found at $z \simeq 0.6$.

4.8.3 Dark Matter Halo Mass

Since the bias of Dark Matter Halos is correlated to their mass (Mo & White 1996), we shall attempt to measure this mass (M_{DMH}). In our analysis we shall follow da Ângela et al. and Croom et al. and assume an ellipsoidal collapse model, described by Sheth et al. (2001). Then the bias and the M_{DMH} are related via

$$b(M_{DMH}) = 1 + \frac{1}{\alpha^{0.5}\delta_c(z)}[\alpha^{0.5}(\alpha\nu^2) + \alpha^{0.5}b(\alpha\nu^2)^{1-c} - \frac{(\alpha\nu^2)^c}{\alpha\nu^2 + b(1-c)(1-\frac{c}{2})}], \quad (4.28)$$

where $\alpha = 0.707$, $b = 0.5$ and $c = 0.6$. ν is defined as $\nu = \delta_c(z)/\sigma(M_{DMH}, z)$, with δ_c to be the critical density for collapse, given by, $\delta_c = 0.15(12\pi)^{\frac{2}{3}}\Omega_m(z)^{0.0055}$ (Navarro et al. 1997). $\sigma(M_{DMH}, z) = \sigma(M_{DMH})G(z)$, where $\sigma(M_{DMH})$ is the rms fluctuation of the density field on the mass scale with value M_{DMH} and $G(z)$ is the linear growth factor (Peebles 1984). The $\sigma(M_{DMH})$ can then calculated as

$$\sigma(M_{DMH})^2 = \frac{1}{2\pi^2}\int_0^\infty k^2 P(k) w(kr)^2 \mathrm{dk}, \quad (4.29)$$

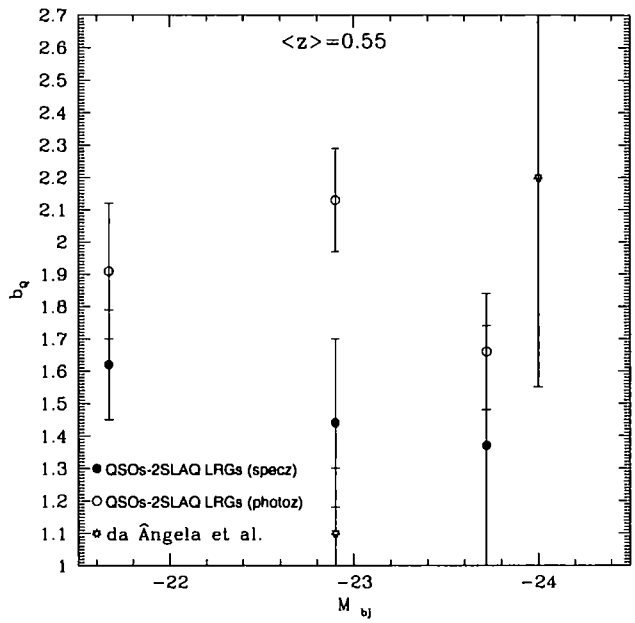

Figure 4.18: Measurement of the QSO bias, b_Q, for QSOs and 2SLAQ LRG samples. For consistency, spectroscopic samples use ξ_{20} from $w_p(\sigma)$ in Table 4.8 rather than the $\xi(s)$ values shown in Fig. 4.16. Stars show the two points taken from Fig. 13 of da Ângela et al. The fainter one is at $< z > \simeq 0.6$ and the brighter at $< z > \simeq 0.7$.

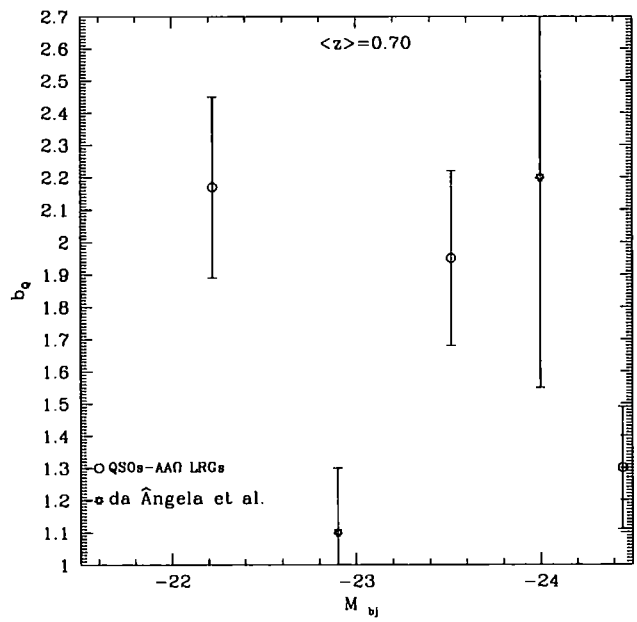

Figure 4.19: Measurement of the QSO bias, b_Q, for QSOs and the (photometric) AAOmega LRG sample. Stars show the two points taken from Fig. 13 of da Ângela et al. The fainter one is at $< z > \simeq 0.6$ and the brighter at $< z > \simeq 0.7$.

with P(k) to be the power spectrum of density perturbations and $w(kr)$ is the Fourier transform of a spherical top hat, which is given by (Peebles 1980):

$$w(kr) = 3\frac{\sin(kr) - kr\cos(kr)}{(kr)^3}, \tag{4.30}$$

where the radius and mass are related through

$$r = \left(\frac{3M_{DMH}}{4\pi\rho_0}\right)^{\frac{1}{3}}, \tag{4.31}$$

where ρ_0 is the present mean density of the Universe, given by $\rho_0 = \Omega_m^0\rho_{crit}^0 = 2.78 \times 10^{11}\Omega_m^0 h^2 M_\odot Mpc^{-3}$. The power spectrum used in our analysis has the linear form, $P(k) = P_0 T(k)^2 k^n$, with P_0 to be a normalisation parameter which depends on σ_8 and T(k) is the transfer function (Bardeen et al. 1986).

The results are shown in Figures 4.20 and 4.21. Once again, although for the AAOmega LRG samples the derived QSO halo masses show indications of increasing as we move to fainter QSO samples, in the case of 2SLAQ (photometric and spectroscopic) LRG samples halo masses stay statistically constant. The average value is $M_{DMH} = 10^{13}h^{-1}M_\odot$. Comparing now this result with those from other authors (Croom et al. 2005, da Ângela et al. 2008), we note that their M_{DMH} estimates are generally lower than ours ($\sim 3 \times 10^{12}h^{-1}M_\odot$) although at higher redshifts ($z = 1.4$). They also find that the hosts of QSOs have the same mass at all redshifts, thus rejecting cosmologically long-lived QSO models. Our higher masses at $z = 0.55$ may be more consistent with the long-lived predictions of $6 \times 10^{14}h^{-1}M_\odot$ at $z = 0$ and $10^{13}h^{-1}M_\odot$ at $z \simeq 0.5$. The caveat is that for our measurements we need to use a value for b_L in order to derive b_Q.

4.9 Discussion + Conclusions

In this Chapter we have performed an analysis of the clustering of QSOs with LRGs. For this purpose, we first used the 2-point angular cross-correlation function, $w(\theta)$, and measured the cross-correlation between 2SLAQ and AAOmega LRGs and different luminosity QSOs. The results show that there is little cross-correlation dependence on QSO luminosity.

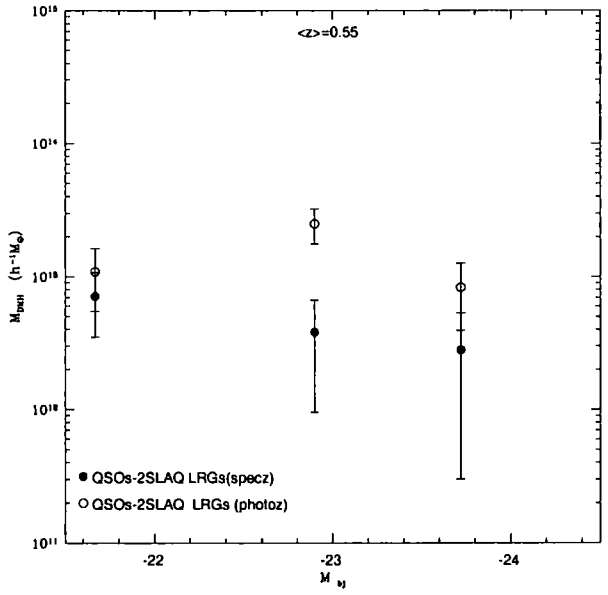

Figure 4.20: Measurement of the M_{DMH}, for different QSO and 2SLAQ LRG samples.

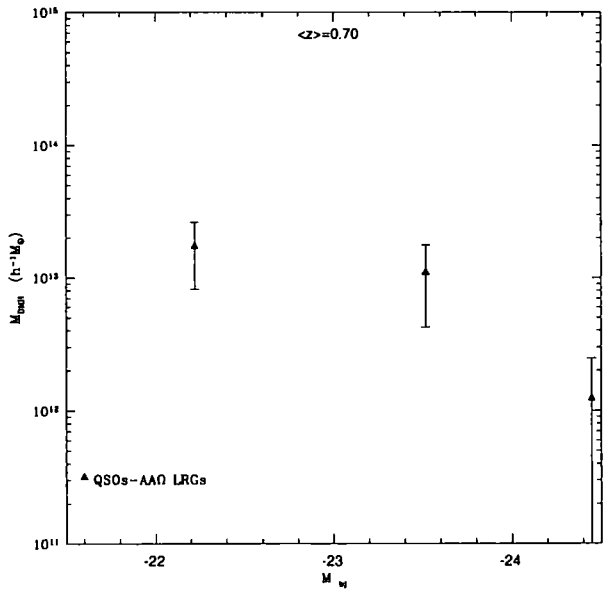

Figure 4.21: Measurement of the M_{DMH}, for different QSO and AAOmega LRG samples.

Table 4.8: QSO-2SLAQ LRG ξ_{20} cross-correlation measurements, as well as QSO b_Q and β_Q measurements, assuming $b_{L(2SLAQ)} = 1.90 \pm 0.08$, from the amplitude results. For consistency, the ξ_{20} measurements for the spectroscopic samples come from $w_p(\sigma)$ and from $\xi(r)$ via $w(\theta)$ for the photometric cases.

	QSO b_Q and β_Q					
	spectroscopic 2SLAQ LRGs			photometric 2SLAQ LRGs		
	2SLAQ QSOs	2QZ QSOs	SDSS QSOs	2SLAQ QSOs	2QZ QSOs	SDSS QSOs
ξ_{20}	0.37 ± 0.06	0.33 ± 0.10	0.31 ± 0.14	0.44 ± 0.08	0.49 ± 0.06	0.38 ± 0.08
b_Q	$1.62^{+0.17}_{-0.17}$	$1.44^{+0.26}_{-0.26}$	$1.37^{+0.37}_{-0.37}$	$1.91^{+0.21}_{-0.21}$	$2.15^{+0.16}_{-0.16}$	$1.67^{+0.18}_{-0.18}$
$\beta_Q(\simeq \frac{\Omega_m^{0.6}}{b})$	$0.46^{+0.05}_{-0.05}$	$0.51^{+0.09}_{-0.09}$	$0.54^{+0.14}_{-0.14}$	$0.28^{+0.03}_{-0.03}$	$0.35^{+0.02}_{-0.02}$	$0.45^{+0.05}_{-0.05}$
M_{bj}	-21.7	-22.9	-23.7	-21.7	-22.9	-23.7

Table 4.9: QSO-AAO LRG ξ_{20} cross-correlation measurements, as well as QSO b_Q and β_Q measurements, assuming $b_{L(AA\Omega)} = 2.35 \pm 0.20$, from the amplitude results.

	QSO b_Q and β_Q		
	photometric AAOmega LRGs		
	2SLAQ QSOs	2QZ QSOs	SDSS QSOs
ξ_{20}	0.55 ± 0.11	0.50 ± 0.11	0.33 ± 0.08
b_Q	$2.17^{+0.28}_{-0.28}$	$1.95^{+0.27}_{-0.27}$	$1.30^{+0.19}_{-0.19}$
$\beta_Q(\simeq \frac{\Omega_m^{0.6}}{b})$	$0.37^{+0.05}_{-0.05}$	$0.41^{+0.06}_{-0.06}$	$0.61^{+0.10}_{-0.10}$
M_{bj}	-22.2	-23.5	-24.5

Next, we measured the redshift-space cross-correlation function. We again see no QSO-LRG clustering dependence on QSO luminosity, as all the QSO-spectroscopic LRG samples gave similar results. We used Limber's formula to fit r_0 to 2-D results. The fits for r_0 from 3-D $\xi(s)$ are in very good agreement with the fits to the 2-D $w(\theta)$ results. Then, we compared our QSO-LRG clustering with 2SLAQ LRG-LRG (Ross et al. 2007) and 2QZ+2SLAQ QSO-LRG (da Ângela et al. 2008) clustering results. We noted that, on small scales, the QSO-QSO and QSO-LRG results appear flatter than the LRG-LRG results. As confirmed later by the $w_p(\sigma)/\sigma$ measurements, this is due to the larger QSO redshift errors (broad-lines). On larger scales ($\geq 5\mathrm{h}^{-1}\mathrm{Mpc}$) the QSO-QSO correlation amplitude appears lower than the QSO-LRG and LRG-LRG amplitudes, suggesting that $b_Q \lesssim b_L$. The fractional errors on ξ_{QL} are $\sim 50\%$ smaller than those on ξ_{QQ} in same redshift range.

The results from the semi-projected cross-correlation function, $w_p(\sigma)/\sigma$, are in agreement with our $\xi(s)$ observations, yielding consistent r_0 and γ values with them. The comparison with the 2SLAQ LRG-LRG (Ross et al. 2007) and 2QZ+2SLAQ QSO-LRG (da Ângela et al. 2008) confirms our results from redshift-space, i.e. that the small-scale amplitude difference in $\xi(s)$ is due to the larger QSO redshift errors and that QSO-QSO clustering amplitude is lower than QSO-LRG and LRG-LRG amplitude. The real-space cross-correlation function, $\xi(r)$, also seems to agree with the $\xi(s)$ and $w_p(\sigma)/\sigma$ results, although it is noisier.

Then, we measured the $\xi(\sigma,\pi)$ cross-correlation function for all our (spectroscopic) samples and used the results to model the redshift-space distortions. For that, we used two models which gave consistent results with each other and between the different samples. The redshift-space distortions yielded an average of $\beta_Q = 0.55 \pm 0.10$, $b_Q = 1.4 \pm 0.2$ which is slightly higher than $b_Q = 1.1 \pm 0.2$ at $z \simeq 0.6$, from da Ângela et al.

After calculating the average absolute magnitude of each QSO sample we measured the integrated cross-correlation function for each one of our QSO-LRG samples. We noted no evidence for QSO-LRG clustering dependence on QSO luminosity. Then, using LRG biases as estimated by previous studies, we calculated the QSO biases. In this case there were indications of luminosity dependence, in the sense

that b_Q may reduce as we move to brighter QSO samples. Our analysis yielded a $b_Q = 1.5 \pm 0.1$ (at $M_{bj} \approx -23$) which is in very good agreement with our result from redshift-space distortions.

Finally, using the relation between bias and M_{DMH} suggested by Sheth et al. (2001), we calculated the corresponding masses of the QSO hosts. QSO halo masses were estimated to be $\sim 10^{13} h^{-1} M_{\odot}$ at $z \approx 0.55$. Our M_{DMH} estimations are higher than those from Croom et al. (2005) and da Ângela et al. (2006) (at $z = 1.4$) and may be explained by long-lived QSO population models. Since the bias values are independent of QSO luminosity at fixed redshift, the halo masses are also independent of luminosity and this represents the main result of this Chapter.

Chapter 5

Cross-clustering of 2PIGG galaxy groups and 2dFGRS galaxies

5.1 Introduction

Previous QSO lensing results (Myers et al. 2003, 2005, Mountrichas & Shanks 2007) have indicated that galaxies are anti−biased on small scales at a higher level than predicted by the standard cosmological model. In continuation of this investigation, we now make dynamical infall estimates of the masses associated with 2dFGRS Percolation-Inferred Galaxy Groups (2PIGG) groups and clusters to compare our results with QSO lensing estimates and also the velocity dispersion mass estimates of Eke et al. (2006).

Here we obtain those dynamical infall estimates of group masses using redshift distortion analysis. The analytical background has already been discussed in the previous Chapter. These redshift-space distortions can be investigated using either the spatial two-point correlation function (e.g. Ratcliffe et al. 1997) or its Fourier transform, the power spectrum (e.g. Outram, Hoyle and Shanks 2001). In recent years many galaxy catalogues have been used for this purpose, the Durham/UKST Galaxy Redshift Survey (Ratcliffe et al. 1996), the IRAS Point Source Redshift Survey (PSCz, Taylor et al. 2000), the Nearby Optical Galaxy (NOG) sample (Giuricin et al. 2001), the Zwicky catalogue (Padilla et al. 2001) and others. The parameters we can measure in these analyses are the velocity dispersion of the galaxies (or

galaxy groups), the infall parameter β, the amplitude of galaxy clustering r_0, the density parameter, Ω_m, and the bias factor, b.

Recently, large group catalogues have been used to study the variation of their halo mass-to-light ratio (M/L) with luminosity. These calculations show us in what halo sizes mass is most efficiently converted into stars. Most recently, the 2PIGG team analysed 2PIGG group velocity dispersion on the 2PIGG group catalogue (Eke et al. 2004a) and found a variation of the halo mass-to-light ratio with group luminosity. More precisely, they found an increase by a factor of 5 in the b_J band and 3.5 in the r_F band, of the halo M/L with a 100 times increased group luminosity (Eke et al. 2004b) as well as a minimum at a total group luminosity of L$\approx$ 5 $\times$ $10^9 h^{-2} L_\odot$ (Eke et al. 2006). Padilla et al. 2004 measured the clustering amplitude of 2PIGG galaxy groups. They found that the most luminous groups are 10 times more clustered than the full 2PIGG catalogue.

In the work presented here, we try to estimate group masses using dynamical infall rather than just the velocity dispersion. We believe that estimating masses by infall may be more accurate because no stability or virial assumptions are needed. We do this by estimating the 3-D redshift space cross-correlation function, $\xi_{cg}(s)$, between the 2PIGG groups and clusters with the 2dFGRS galaxies (Section 5.3) as well as the semi-projected cross-correlation function, $w_p(\sigma)/\sigma$ and the real-space cross-correlation function, $\xi_{cg}(r)$ (Sections 5.4, 5.5). In Section 5.6 we present our $\xi_{cg}(\sigma, \pi)$ results and constrain the cluster-galaxy infall parameter, β, by modelling the redshift-space distortions. In Section 5.7 we find the group luminosities and we repeat our previous measurements, as a function of luminosity. Finally, our conclusions are presented in Section 5.8.

5.2 Data and Clustering Analysis

5.2.1 Data

The 2dFGRS galaxies (Lewis et al. 2002) are here used both as the source of the group and cluster catalogue and as dynamical tracers. The 2dFGRS sample contains 191,440 galaxies (NGP+SGP) once cuts have been applied for field and

Table 5.1: Number of groups in the data and mock catalogues ($z < 0.12$).

n_{gal}	data	mock
=1	45,227	20,152
2-3	11,742	9,959
=4	2,517	1,096
5-8	3,005	1,375
9-17	1,082	592
18-29	204	201
30-44	54	100
45-69	43	67
≥ 70	39	80

sector completeness. The magnitude limit of the survey is $b_J = 19.45$.

The galaxy groups we use are taken from the 2dFGRS Percolation-Inferred Galaxy Group (2PIGG) catalogue (Eke et al. 2004a). The groups are derived using a friends-of-friends (FOF) algorithm. This algorithm has been calibrated and tested using mock 2dFGRS catalogues and then applied to the real 2dFGRS in order to construct the 2PIGG catalogue. The algorithm as well as its calibration is described in detail by Eke et al. 2004a. The catalogue consists of 28,877 groups with at least two members (in the whole redshift range). Following Eke et al. we shall only use groups with $z < 0.12$ because at higher redshifts the fraction of the total group luminosity observed falls below 50% and also the contamination rate increases. We also follow the group membership classes used in Fig. 5 of Eke et al. 2004a but we split the $18 \leq n_{gal} \leq 44$ and $n_{gal} \geq 45$ each into 2 subsamples to get group samples with intermediate and high memberships. Moreover we use two more 'group' samples at small memberships, those with $2 \leq n_{gal} \leq 3$ and $n = 1$. The numbers of each group sample used are shown in Table 5.1.

In our measurements we also use mock catalogues constructed by the 2PIGG team (Eke et al. 2004a) and which are available on the World Wide Web. Mock catalogues are simulated samples which follow the same selection criteria with the

real samples. In our case, high-resolution N-body simulations of cosmological volumes (Jenkins et al. 1998) and a semi-analytical model of galaxy formation (Cole et al. 2000) were used for the construction of the mock catalogues. A full description of the catalogues and the methods used for their construction is given by Eke et al. 2004a. The mock catalogue consists of 25,201 groups in both the NGP and the SGP (in the whole redshift range). This number is slightly lower than the corresponding one from the real data. We divide the mock groups in the same classes as for the data and apply the redshift cut of $z < 0.12$. The numbers are again shown in Table 5.1. We note that the mock catalogue contains more large membership groups than the data catalogue.

For our random catalogues, field and sector completeness have been taken into account. The catalogues consist of $\approx 11\times$ the number of our galaxies, i.e. 2,105,840 random points in the NGP+SGP.

5.2.2 Cross-correlation and errors estimators

The correlation function estimator that we use for our analysis is given by equation 1.44, where n_{ran} is the number of the random points in our catalogue, n_{data} is the number of galaxies we use, $DD(\theta)$ is the group-galaxy pairs and $DR(\theta)$ is the group-random point pairs counted at angular separation θ.

The errors we use throughout our analysis are Field-to-Field errors (equation 1.48). For that purpose we have divided NGC and the SGC each into 3 equal areas and then measure the correlation functions for each one of these 6 areas. In the next Section we shall see how the Field-to-Field errors compare with Poisson errors (equation 1.47) for our $\xi(s)$ measurements.

5.3 Redshift−space cross-correlation function

In this Section we present our measurements for the group-galaxy redshift-space cross-correlation function $\xi_{cg}(s)$ for different group memberships, as they were described in Section 5.2. The purpose of these measurements is to study how the clustering amplitude changes for different groups and clusters and to obtain the

values for the correlation amplitude s_0 and the slope γ from single power law fits, in order to use them later on when we shall model our $\xi(\sigma,\pi)$ measurements (even though, as shall be explained, we will ultimately let s_0 float as a free parameter in the redshift distortion fits). We first measure $\xi_{cg}(s)$ in each Galactic Cap separately, i.e. NGC and SGC and then by adding the DDs together and the normalised DRs and using the expression 1.42 we combine these measurements to get the overall result. We should note that the SGC tends to give a slightly bigger correlation length, which is in accordance with the fact that larger membership clusters are found in the SGC. The combined results (North+South) are shown in Fig. 5.1.

As expected the groups with larger memberships have higher correlation lengths (s_0) and the ungrouped galaxies have by far the smallest correlation length. This is reflected in the fits ($2 \leq s \leq 20\mathrm{h}^{-1}\mathrm{Mpc}$) to these cross-correlation functions. All the fits assume the same power law form, i.e. $\xi_{cg}(s) = (s/s_0)^{-\gamma}$ with both s_0 and γ allowed to vary. The error estimates come from the 1σ deviation from the minimized χ^2 on these fits. The solid line in Figure 5.1 is the best fit to our $\xi_{cg}(s)$ measurements for our group sample with $n_{gal} = 4$. The slope is $\gamma = 1.6 \pm 0.1$ and the correlation length is $s_0 = 4.5 \pm 0.4\mathrm{h}^{-1}\mathrm{Mpc}$. The dashed line is the fit to our groups with the largest membership, i.e. $n_{gal} \geq 70$, with $\gamma = 1.5 \pm 0.3$ and $s_0 = 11.5 \pm 1.1\mathrm{h}^{-1}\mathrm{Mpc}$. The fits for all the other group samples have also been estimated and appear in Table 5.2. As we see our fits give $\gamma \sim 1.5 - 1.8$ and $s_0 \sim 2.0 - 11.5\mathrm{h}^{-1}\mathrm{Mpc}$.

We next repeat our measurements using the mock catalogues for galaxies and groups. The $\xi_{cg}(s)$ results are shown in Fig. 5.2. The s_0 and γ values from the fits on the results appear in Table 5.3. From the comparison between the $\xi_{cg}(s)$ measurements from the data and the mock catalogues we see that the results are very similar on all scales. The agreement is confirmed from the fits shown in Tables 5.2 and 5.3.

As already mentioned in the previous Section, for our measurements we have used Field-to-Field errors. Fig. 5.3 shows how the ratio of these errors to Poisson errors, depends on the separation, s. We note that the ratio increases as we move to larger scales. The reason is that on larger scales the group-galaxy pairs become less independent causing an underestimation by Poisson errors. On our scales of interest

(i.e. $2 - 20\mathrm{h}^{-1}\mathrm{Mpc}$), the results follow a power law, i.e. $(s/0.5\mathrm{h}^{-1}\mathrm{Mpc})^{1.1}$.

5.4 The semi-projected cross-correlation function

The semi-projected cross-correlation function, $w_p(\sigma)/\sigma$, has already been described in Section 4.5. Fig. 5.4 shows the $w_p(\sigma)/\sigma$ results for the different galaxy-group samples. Since the measurements are noisier than those for $\xi(s)$, we make fits on scales of $2 \leq r \leq 10\mathrm{h}^{-1}\mathrm{Mpc}$. The solid line (Fig. 5.4) shows the fit for the galaxy sample with $n_{gal} = 4$ which gives a correlation length of $r_0 = 5.5\mathrm{h}^{-1}\mathrm{Mpc}$ with slope of $\gamma = 1.8$. The dashed line is our fit for the galaxy groups with $n_{gal} \geq 70$ which gives $r_0 = 11.5\mathrm{h}^{-1}\mathrm{Mpc}$ and $\gamma = 2.4$. The fits for all the other group samples appear in Table 5.2. With the exception of very small groups and very rich clusters, the slope remains roughly the same, whereas the amplitude, as expected, increases with increased group membership. Fig. 5.5 shows the $w_p(\sigma)/\sigma$ results for the different galaxy-group samples using the mock catalogues and Table 5.3 shows the fits ($2 \leq r \leq 10\mathrm{h}^{-1}\mathrm{Mpc}$). From the comparison between the data and the mock catalogues, we see that the results are very similar on all scales.

5.5 The real-space cross-correlation function

The real-space cross correlation function, $\xi_{cg}(r)$, has already been described in Section 4.6. The results are shown in Fig. 5.6. As in the previous Sections, Table 5.2 shows the r_0 and γ values from the fits ($2 \leq r \leq 10\mathrm{h}^{-1}\mathrm{Mpc}$). Once again, we notice that the real space cross-correlation function has a higher correlation length for groups with larger membership. The results seem to be in agreement with the $\xi_{cg}(s)$ and the $w_p(\sigma)/\sigma$ measurements, although they are much noisier.

Then we repeat the $\xi_{cg}(r)$ measurements using the mock catalogues. The results are shown in Fig. 5.7. The results from the fits appear in Table 5.3. From the comparison between the data and the mock catalogues, we see that the results are very similar on all scales.

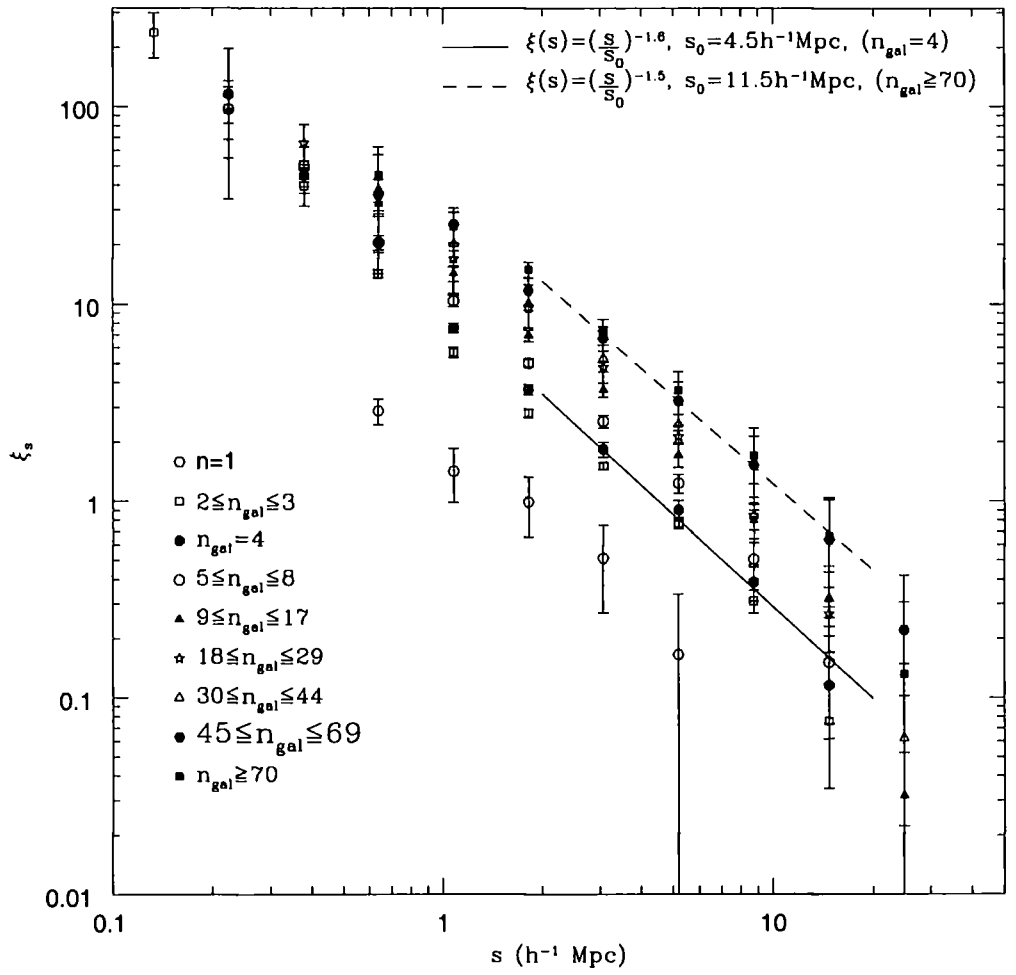

Figure 5.1: The galaxy group-galaxy redshift-space cross-correlation function $\xi_{cg}(s)$ for different group memberships. The solid line is the best fit to our $\xi_{cg}(s)$ measurements for our group sample with $n_{gal} = 4$. The slope is $\gamma = 1.6$ and the correlation length is $s_0 = 4.5\text{h}^{-1}\text{Mpc}$. The dashed line is the fit to our groups with the largest membership, i.e. $n_{gal} \geq 70$, with $\gamma = 1.5$ and $s_0 = 11.5\text{h}^{-1}\text{Mpc}$.

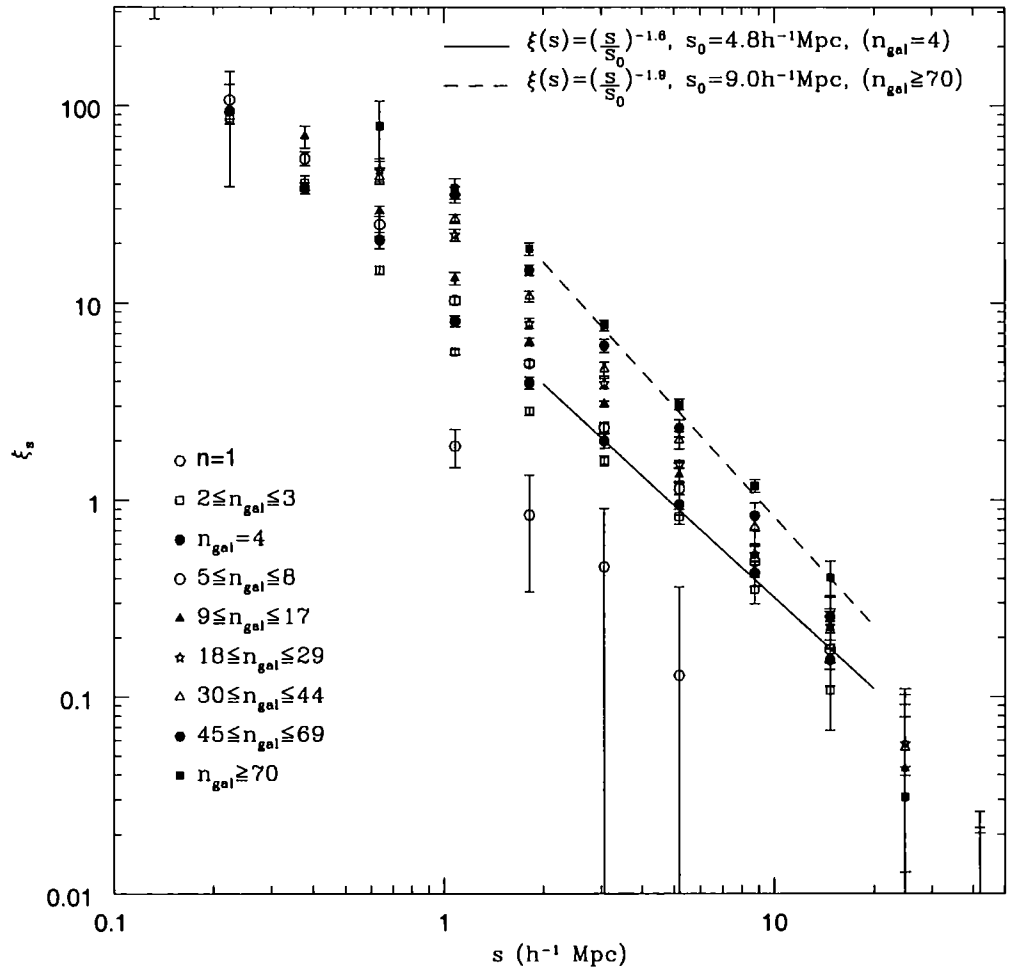

Figure 5.2: The galaxy group-galaxy redshift-space cross-correlation function $\xi_{cg}(s)$ for different group membership using the mock catalogues. The solid line is the best fit to our $\xi_{cg}(s)$ measurements for our group sample with $n_{gal} = 4$. The slope is $\gamma = 1.6$ and the correlation length is $s_0 = 4.8\mathrm{h}^{-1}\mathrm{Mpc}$. The dashed line is the fit to our groups with the largest membership, i.e. $n_{gal} \geq 70$, with $\gamma = 1.9$ and $s_0 = 9.0\mathrm{h}^{-1}\mathrm{Mpc}$.

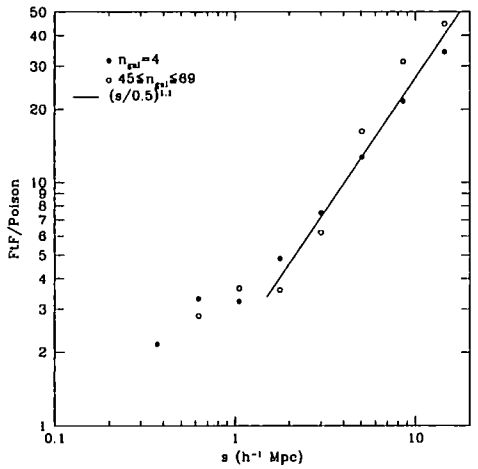

Figure 5.3: Variation between $\xi_{cg}(s)$ Field-to-Field and Poisson errors over the separation s. Filled circles correspond to galaxy groups with $n_{gal} = 4$ and open circles to galaxy groups with $45 \leq n_{gal} \leq 69$. On our scales of interest (i.e. $2 - 20h^{-1}$Mpc) the results follow a power law, i.e. $(s/0.5)^{1.1}$.

Table 5.2: r_0 (or s_0) and γ values for the three cross-correlation functions, i.e. $\xi_{cg}(s)$, $w_p(\sigma)/\sigma$ and $\xi_{cg}(r)$, using the data catalogues.

n_{gal}	$\xi(s)$		$w_p(\sigma)/\sigma$		$\xi(r)$	
	s_0	γ	r_0	γ	r_0	γ
=1	1.8 ± 0.2	1.6 ± 0.2	3.0 ± 0.2	2.7 ± 0.2	3.5 ± 0.5	1.3 ± 0.2
2-3	4.0 ± 0.4	1.5 ± 0.1	4.0 ± 0.5	2.2 ± 0.2	3.5 ± 0.5	1.2 ± 0.3
=4	4.5 ± 0.4	1.6 ± 0.1	5.5 ± 0.5	1.8 ± 0.3	3.5 ± 0.4	1.1 ± 0.3
5-8	5.5 ± 0.4	1.6 ± 0.2	8.0 ± 0.8	1.8 ± 0.2	5.5 ± 1.0	1.5 ± 0.2
9-17	7.0 ± 0.5	1.5 ± 0.2	10.5 ± 0.9	1.7 ± 0.2	6.5 ± 1.0	1.5 ± 0.2
18-29	7.5 ± 0.6	1.7 ± 0.2	14.0 ± 1.4	1.6 ± 0.2	9.0 ± 1.0	1.3 ± 0.2
30-44	7.5 ± 0.8	1.8 ± 0.2	16.0 ± 1.5	1.5 ± 0.2	8.5 ± 0.8	1.3 ± 0.2
45-69	11.0 ± 0.9	1.5 ± 0.3	15.5 ± 2.0	1.9 ± 0.2	5.0 ± 1.0	2.3 ± 0.4
≥ 70	11.5 ± 1.1	1.5 ± 0.3	11.5 ± 1.5	2.4 ± 0.2	6.5 ± 0.6	2.3 ± 0.4

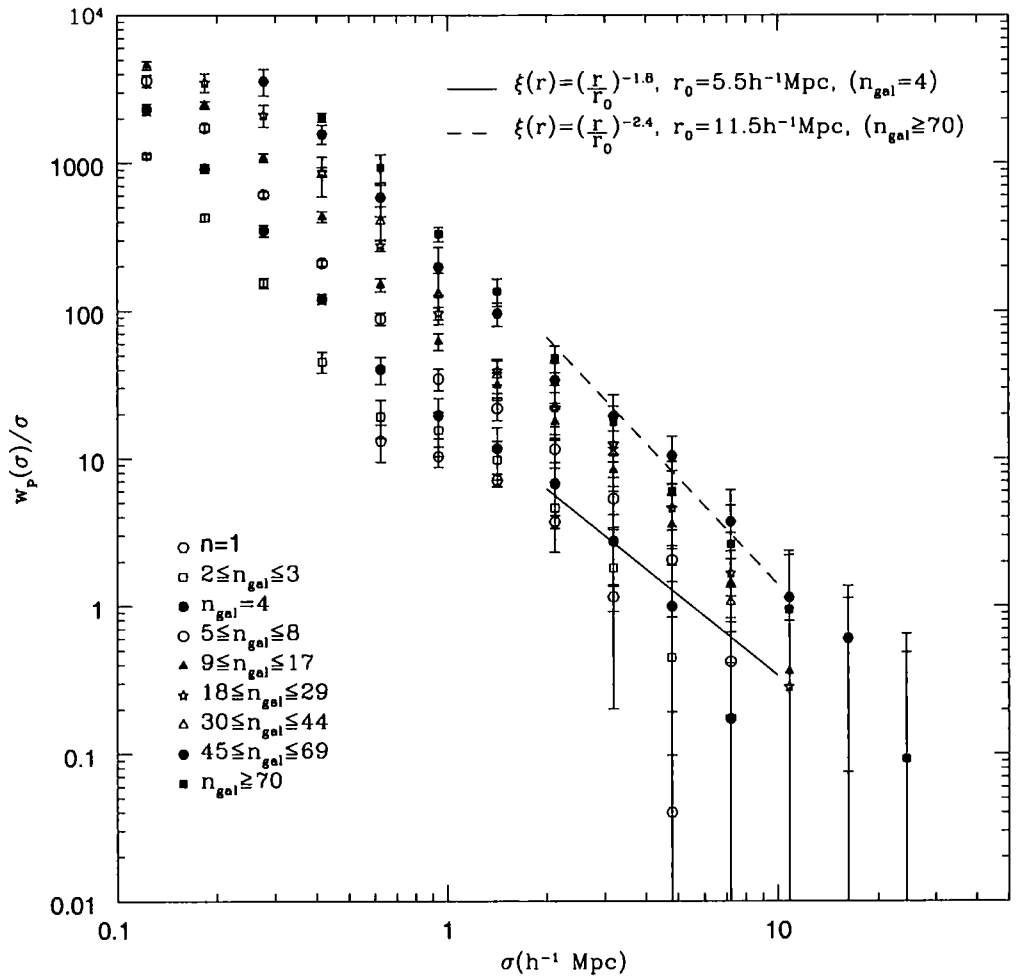

Figure 5.4: The galaxy group-galaxy semi-projected cross-correlation function $\omega_p(\sigma)$ for different group membership, using the data catalogues. The solid line shows the fit for the galaxy sample with $n_{gal} = 4$ which gives a correlation length of $r_0 = 4.5h^{-1}$Mpc with slope of $\gamma = 2.6$. The dashed line is our fit for the galaxy groups with $n_{gal} \geq 70$ which gives $r_0 = 11.5h^{-1}$Mpc and $\gamma = 2.4$.

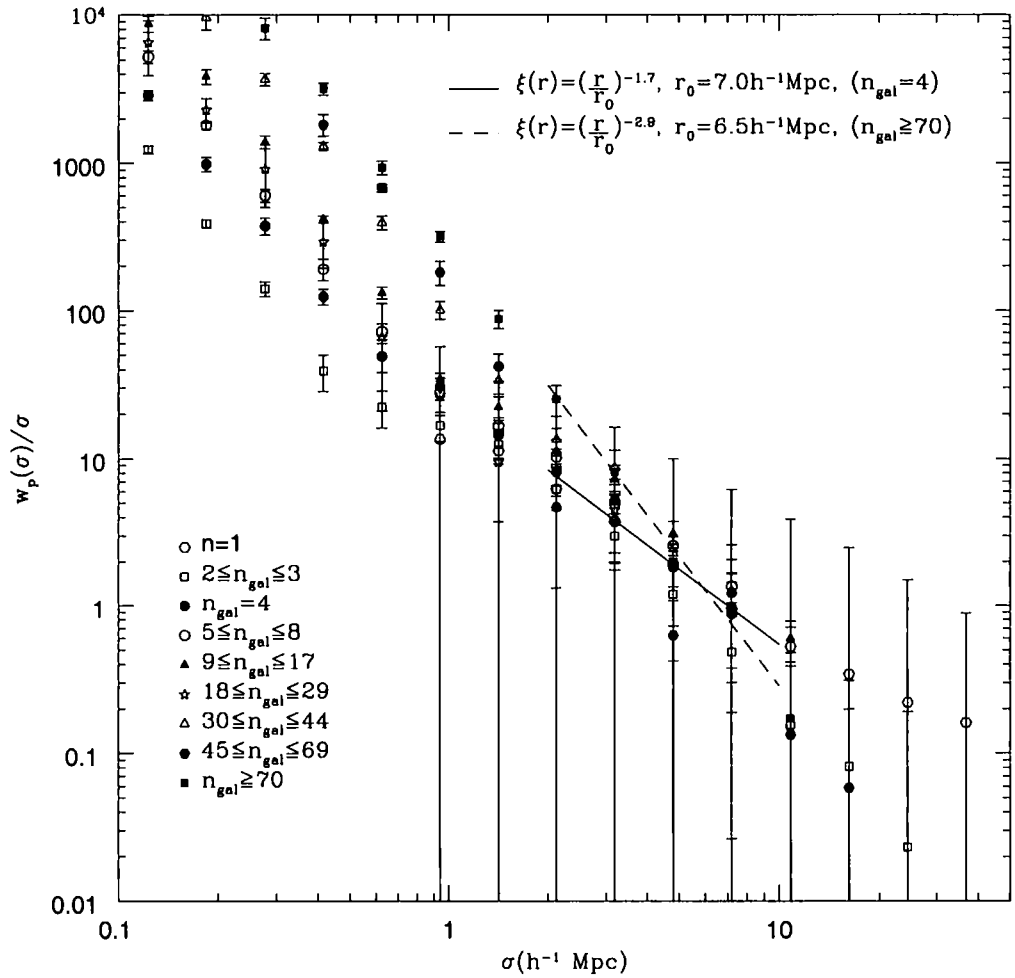

Figure 5.5: The galaxy group-galaxy semi-projected cross-correlation function $\omega_p(\sigma)$ for different group membership using the mock catalogues. The solid line shows the fit for the galaxy sample with $n_{gal} = 4$ which gives a correlation length of $r_0 = 7.0h^{-1}$Mpc with slope of $\gamma = 1.7$. The dashed line is our fit for the galaxy groups with $n_{gal} \geq 70$ which gives $r_0 = 6.5h^{-1}$Mpc and $\gamma = 2.9$.

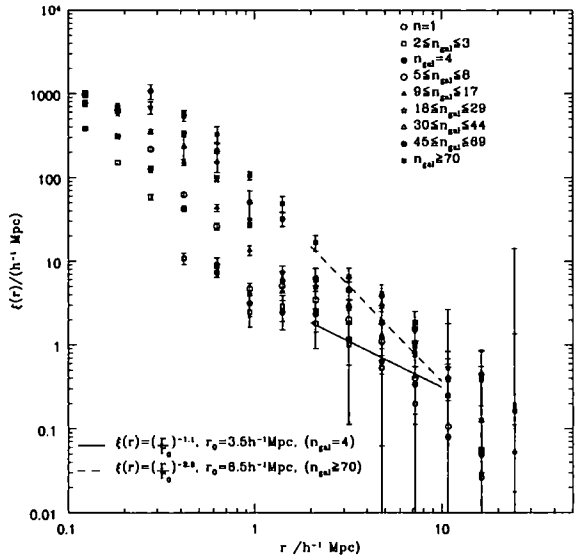

Figure 5.6: The real-space cross-correlation function, $\xi_{cg}(r)$, results using the data sets.

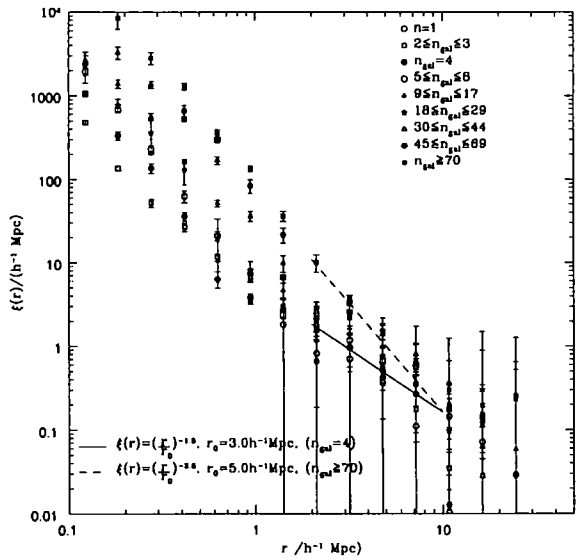

Figure 5.7: The real-space correlation function, $\xi_{cg}(r)$, results using the mock catalogues.

Table 5.3: r_0 (or s_0) and γ values for the three cross-correlation functions, i.e. $\xi_{cg}(s)$, $w_p(\sigma)/\sigma$ and $\xi_{cg}(r)$, using the mock catalogues.

n_{gal}	$\xi(s)$		$w_p(\sigma)/\sigma$		$\xi(r)$	
	s_0	γ	r_0	γ	r_0	γ
=1	1.8 ± 0.2	1.8 ± 0.1	8.0 ± 0.5	1.4 ± 0.1	2.0 ± 0.2	1.2 ± 0.2
2-3	4.0 ± 0.3	1.5 ± 0.1	5.5 ± 0.4	1.9 ± 0.1	3.0 ± 0.2	1.5 ± 0.2
=4	4.8 ± 0.4	1.6 ± 0.2	7.0 ± 0.5	1.7 ± 0.1	3.0 ± 0.2	1.5 ± 0.2
5-8	5.0 ± 0.4	1.6 ± 0.2	9.0 ± 0.9	1.6 ± 0.2	3.5 ± 0.4	1.5 ± 0.2
9-17	6.0 ± 0.4	1.6 ± 0.2	10.5 ± 1.0	1.6 ± 0.1	5.5 ± 1.0	1.3 ± 0.2
18-29	6.0 ± 0.5	1.9 ± 0.2	7.5 ± 0.8	1.9 ± 0.2	4.5 ± 0.5	1.7 ± 0.2
30-44	7.0 ± 0.6	1.8 ± 0.2	10.5 ± 1.0	1.7 ± 0.2	3.0 ± 0.3	2.2 ± 0.3
45-69	7.5 ± 0.7	2.0 ± 0.3	5.0 ± 0.8	2.0 ± 0.3	4.5 ± 0.6	2.4 ± 0.4
≥ 70	9.0 ± 1.0	1.9 ± 0.2	6.5 ± 0.5	2.9 ± 0.2	5.0 ± 0.5	2.6 ± 0.4

5.6 Constraining β from redshift-space distortions

5.6.1 The $\xi_{cg}(\sigma, \pi)$ cross-correlation function

Now we shall present our $\xi_{cg}(\sigma, \pi)$ results from the group-galaxy data samples as well as the mock catalogues. These results will be used later in order to model the redshift-space distortions. More precisely, the shape of the $\xi_{cg}(\sigma, \pi)$ measurements will be used.

Fig. 5.8 shows our results for galaxy groups with $n_{gal} = 4$, $9 \leq n_{gal} \leq 17$ and $45 \leq n_{gal} \leq 69$ (solid lines). Comparing the results from different samples we see that, moving to bigger galaxy groups, differentiations from the nearly symmetric clustering pattern of $n_{gal} = 4$ group-galaxies start to increase. Elongations in the redshift direction along the line-of-sight (π-direction) are most evident for the larger membership galaxy-group samples of $45 \leq n_{gal} \leq 69$.

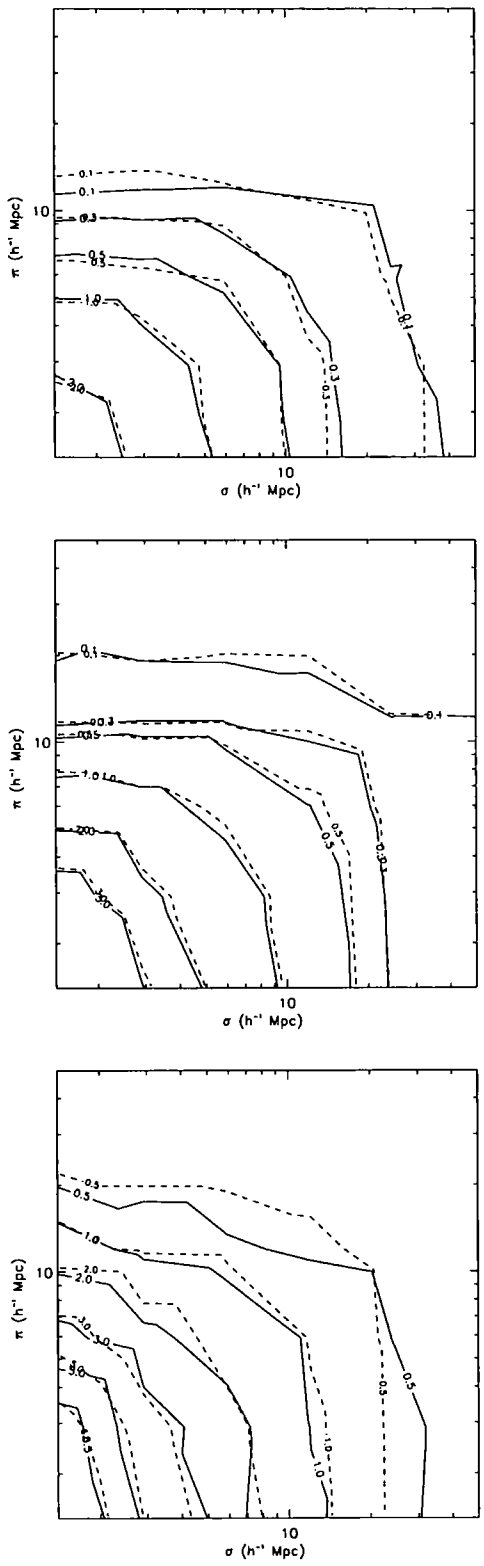

Figure 5.8: $\xi_{cg}(\sigma, \pi)$ results for group-galaxy sample with $n_{gal} = 4$, $18 \leq n_{gal} \leq 29$ and $45 \leq n_{gal} \leq 69$ group samples (from top to bottom). The results from the fitted models (dashed lines) are consistent with those from the data (solid lines) in all cases.

5.6.2 Model description

We assume that the effects of redshift-space distortions can be modelled by adjusting $\xi(r)$ for the effects of velocity dispersion and a simple infall model. The model we assume for the bias is,

$$\xi_{cm} = \frac{\xi_{cg}}{b}. \tag{5.1}$$

Next we introduce the infall velocity of the galaxies, $v(r_z)$, as a function of the real-space separation along the π direction, r_z, adapting eqn 77.24 of Peebles (1980) and assuming a power law of slope $-\gamma$ for $\xi_{cg}(r)$ we get,

$$v(r_z) = -\frac{1}{3-\gamma}\beta H(z) r_z \xi_{cg}(r), \tag{5.2}$$

where we have substituted $\beta = \frac{\Omega^{0.6}}{b}$. Equation 5.2 applies in the linear regime ($\xi_{cm} \lesssim 1$) for infall into rich clusters. We accept it is an approximation to apply equation 5.2 to groups, where group-group interactions may be non-negligible.

The magnitude of the elongation along the π-direction of the $\xi_{cg}(\sigma, \pi)$ plot caused by the galaxy velocity dispersion denoted by $< \omega_z^2 >^{1/2}$, is again given by equation 4.19. In order to include the small scale redshift-space effects due to the random motions of galaxies, we convolve the $\xi_{cg}(\sigma, \pi)$ model with the velocity dispersion distribution, given by the equation 4.19. Then $\xi_{cg}(\sigma, \pi)$ is given by (Peebles 1980, Hoyle 2000)

$$1 + \xi(\sigma, \pi) = \int_{-\infty}^{+\infty} (1 + \xi(r)) f(\omega_z) \mathrm{d}\omega_z, \tag{5.3}$$

and modifying this to include the effects of the bulk motions we finally get

$$1 + \xi_{cg}(\sigma, \pi) = \int_{-\infty}^{+\infty} (1 + \xi_{cg}(r)) f(\omega_z - v(r_z))) \mathrm{d}\omega_z. \tag{5.4}$$

This is the $\xi_{cg}(\sigma, \pi)$ we get from our model and following the fitting procedure described in Section 4.7.2 we put constraints on β_{cg} for each one of our group-galaxy samples.

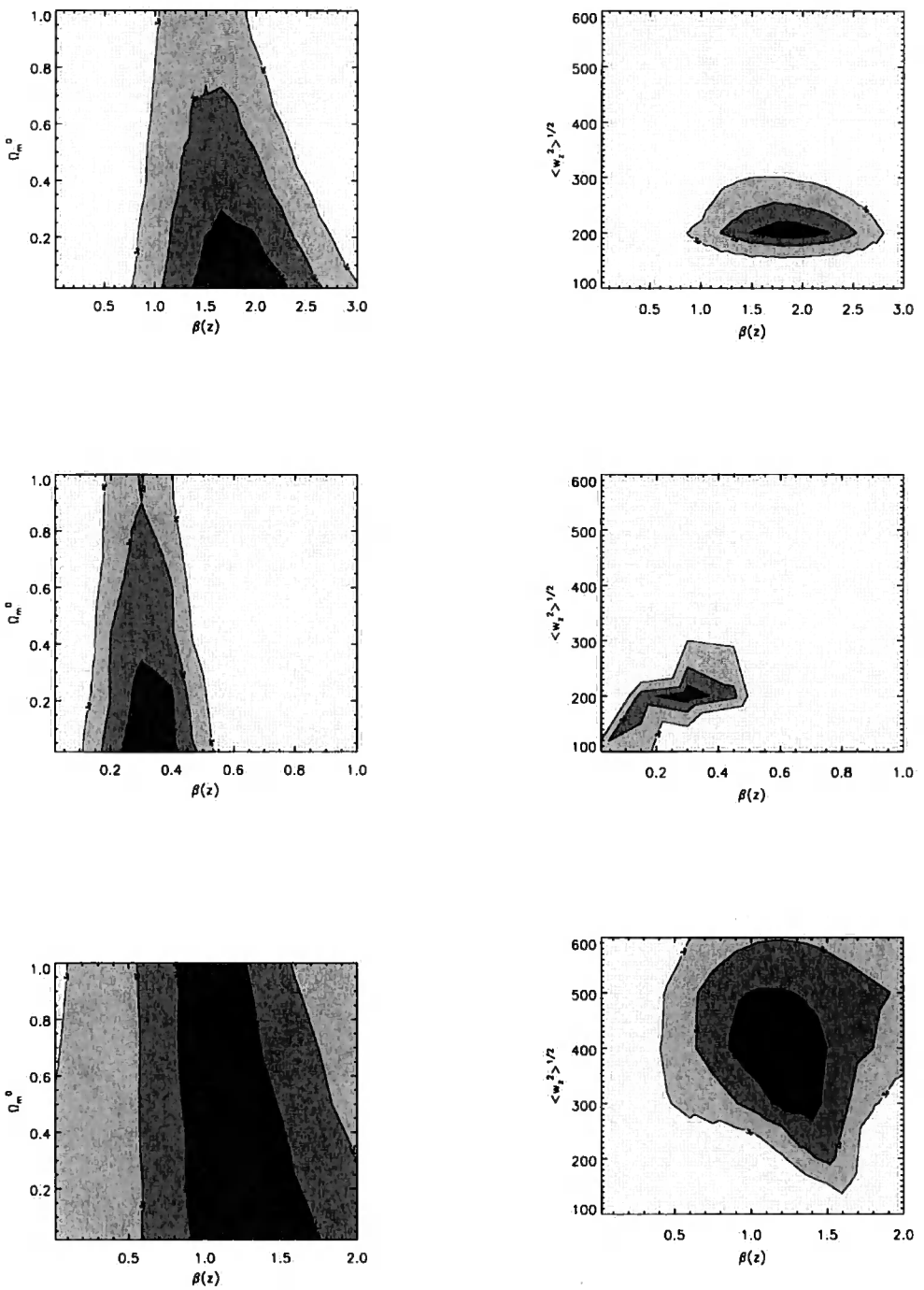

Figure 5.9: Likelihood contours of $\Omega_m^0 - \beta(z = 0.11)$ (left) and $< w_z^2 >^{1/2} - \beta(z = 0.11)$ (right) for the $n_{gal} = 4$, $18 \leq n_{gal} \leq 29$ and $45 \leq n_{gal} \leq 69$ group samples (from top to bottom). The best fit values are shown in Tables 5.4 and 5.5.

5.6.3 Results from modelling redshift-space distortions

In our analysis we have used three methods, which differ in their treatment of the galaxy velocity dispersion. For our first method, we use the average velocity dispersions of our group samples, as assigned by the 2PIGG team. We shall call these, fixed group velocity dispersions. It should be noted, that in the measurement of these $< w_z^2 >^{1/2}$ the 2PIGG team has included the redshift measurement error which will contribute $\sigma_{err} \sim 85 \mathrm{kms}^{-1}$ (Eke et al. 2004a) to their velocity dispersion measurements.

The second method is to fit the group velocity dispersion, i.e. choose that which gives the smallest χ^2 value to our $\Omega_m^0 - \beta$ estimates from $\xi_{cg}(\sigma, \pi)$. We shall call these χ^2 velocity dispersions of our samples. We do not expect the two group velocity dispersions (fixed and χ^2) to be the same because our fits to ξ_{cg} take into account both the finger−of−god effect and the dynamical flattening in the π direction. On the other hand, the 2PIGG velocity dispersion estimation ignores dynamical infall, at least before any calibration is applied from the mock catalogues.

The third and final method is to keep $\Omega_m^0 = 0.3$ constant, and instead fit for the group velocity dispersion. Thus, instead of fitting $\Omega_m^0 - \beta$ we fit for $< w_z^2 >^{1/2} - \beta$ at fixed Ω_m^0.

For all three methods, the assumed cosmology has $\Omega_m = 0.3$ and $\Omega_\Lambda = 0.7$. We also use the s_0 and γ values from the fits on the $\xi_{cg}(s)$ measurements, shown in Tables 5.2 and 5.3 for the data and the mocks, respectively. Nevertheless, as already noted, we let s_0 vary as a free parameter. As has been pointed out (Section 5.3), the fits on the $\xi_{cg}(s)$ measurements have been made on scales of $2 - 20 \mathrm{h}^{-1}\mathrm{Mpc}$. However, in our fitting procedure we use scales of $5 - 40 \mathrm{h}^{-1}\mathrm{Mpc}$. Since the errors increase at larger scales we have simply extrapolated our smaller scale fits into this region. The reason for moving further away from the group centres is that the infall model in equation 5.2 only applies on large linear scales. Our results, both for the group-galaxy velocity dispersions, $< w_z^2 >^{1/2}$, and the infall parameters, β, are shown in Tables 5.4 and 5.5. In Fig. 5.9 we show the $\Omega_m^0 - \beta(z = 0.11)$ and $< w_z^2 >^{1/2} - \beta(z = 0.11)$ contours (methods 2 and 3) for data group-galaxy samples with $n_{gal} = 4$, $18 \leq n_{gal} \leq 29$ and $45 \leq n_{gal} \leq 69$, respectively.

Table 5.4: Estimation of $< w_z^2 >^{1/2}$ for different galaxy group memberships.

	$< w_z^2 >^{1/2}$ (km/s)					
	data			mock		
	fixed	χ^2	$\Omega_m^0 = const$	fixed	χ^2	$\Omega_m^0 = const$
=1		250	200^{+10}_{-30}		240	200^{+90}_{-200}
2-3	160	280	200^{+10}_{-10}	165	280	250^{+60}_{-60}
=4	174	250	200^{+30}_{-10}	190	280	200^{+10}_{-90}
5-8	221	300	300^{+20}_{-40}	226	300	300^{+5}_{-25}
9-17	285	290	200^{+30}_{-10}	299	280	200^{+15}_{-10}
18-29	371	280	200^{+20}_{-15}	388	280	150^{+10}_{-150}
30-44	420	270	250^{+60}_{-250}	443	260	300^{+50}_{-300}
45-69	488	430	400^{+110}_{-130}	472	450	400^{+130}_{-130}
≥ 70	606	410	400^{+110}_{-130}	588	390	300^{+110}_{-280}

Fig. 5.8 shows our $\xi_{cg}(\sigma, \pi)$ model results for galaxy groups with $n_{gal} = 4$, $9 \leq n_{gal} \leq 17$ and $45 \leq n_{gal} \leq 69$ (dashed lines). The results from the fitted models (dashed lines) are consistent with those from the data (solid lines) in all cases.

5.6.4 Discussion of the results

Fig. 5.10 (top) shows a comparison of the $< w_z^2 >^{1/2}$ values using the three different methods, for the data. We see, that the fixed values (open circles) increase with increased group membership whereas the χ^2 velocity dispersions (filled circles) stay roughly constant for small and intermediate group-galaxy samples and rise for clusters. The reason for this discrepancy may be due to the different methods, as explained above. Our third method (keep Ω_m^0 constant, triangles) follows (roughly) the same pattern as the χ^2 fits. The same pattern is repeated for the mocks (Fig. 5.10, bottom). Finally, Fig. 5.11 shows a data-mock comparison using the χ^2 group velocity dispersions. The two results are in very good agreement and in both cases we notice the big jump that the velocity dispersion makes for the group samples

Table 5.5: Estimation of β for different galaxy group memberships.

	data			mock		
n_{gal}	$\beta(fixed)$	$\beta(\chi^2)$	$\Omega_m^0 = const$	$\beta(fixed)$	$\beta(\chi^2)$	$\Omega_m^0 = const$
=1		$4.00^{+1.60}_{-2.13}$	$1.50^{+2.70}_{-1.00}$		$6.50^{+1.50}_{-4.00}$	$4.25^{+0.65}_{-2.55}$
2-3	$4.80^{+0.40}_{-0.60}$	$2.60^{+0.35}_{-0.40}$	$2.75^{+0.25}_{-0.25}$	$6.50^{+2.51}_{-1.25}$	$3.80^{+1.60}_{-0.80}$	$4.25^{+1.55}_{-1.00}$
=4	$2.55^{+0.50}_{-0.40}$	$1.80^{+0.50}_{-0.41}$	$1.80^{+0.50}_{-0.30}$	$2.75^{+0.60}_{-0.62}$	$2.50^{+0.95}_{-0.90}$	$2.20^{+1.55}_{-0.40}$
5-8	$1.65^{+0.17}_{-0.25}$	$1.35^{+0.28}_{-0.35}$	$1.35^{+0.30}_{-0.35}$	$1.50^{+0.29}_{-0.20}$	$1.25^{+0.35}_{-0.20}$	$1.20^{+0.35}_{-0.15}$
9-17	$0.75^{+0.21}_{-0.24}$	$0.75^{+0.20}_{-0.23}$	$0.90^{+0.08}_{-0.17}$	$0.60^{+0.21}_{-0.12}$	$0.60^{+0.23}_{-0.17}$	$0.80^{+0.20}_{-0.10}$
18-29	$0.40^{+0.07}_{-0.14}$	$0.30^{+0.12}_{-0.07}$	$0.30^{+0.08}_{-0.10}$	$0.30^{+0.50}_{-0.30}$	$0.30^{+0.22}_{-0.28}$	$0.30^{+0.30}_{-0.30}$
30-44	$0.30^{+0.27}_{-0.30}$	$0.30^{+0.20}_{-0.30}$	$0.30^{+0.12}_{-0.30}$	$0.40^{+0.25}_{-0.28}$	$0.50^{+0.35}_{-0.23}$	$0.80^{+0.50}_{-0.30}$
45-69	$1.20^{+0.55}_{-0.48}$	$1.30^{+0.45}_{-0.50}$	$1.20^{+0.25}_{-0.35}$	$1.50^{+3.20}_{-1.20}$	$1.50^{+2.95}_{-1.20}$	$1.20^{+0.35}_{-0.45}$
≥ 70	$1.50^{+0.35}_{-0.52}$	$2.50^{+0.71}_{-1.10}$	$2.50^{+0.30}_{-0.80}$	$1.80^{+0.21}_{-0.45}$	$1.90^{+0.11}_{-0.43}$	$2.50^{+3.00}_{-0.90}$

with the two largest memberships.

Fig. 5.12 (top) shows a comparison of the β values using the three different methods for the data. We see that all three give consistent results. Small group-galaxies have a large infall parameter which decreases as we move to larger membership group-galaxy samples. This is in agreement with the lensing results presented in Chapter 3. Then, it rises up again for cluster-galaxies. It is unclear what causes the infall parameter to rise again. This could be due to statistics since our rich cluster samples are very small (Table 5.1). The increase of β means that the implied bias rises by the same factor ($\approx 8\times$). The same pattern is followed using the mock catalogues (Fig. 5.12, bottom). The only difference is that the factor is now slightly higher than in the data case. Of course, in the case of mocks, the minimum in β is expected, as the efficiency of galaxy formation is modelled to be lower at high and low halo masses. Finally, Fig. 5.13 shows a comparison between the data and the mocks using the $\chi^2 < w_z^2 >^{1/2}$. Once again, the agreement is very good.

As already mentioned the infall parameter, β, estimated in this Section is a bias indicator. Therefore, we would like to compare our Fig. 5.12 with the M/L results of Eke et al. 2004b and 2006. Both results show a similar behaviour, i.e. the

existence of a minimum value for β (or M/L) which rises for small groups and rich clusters. What we would like to check is the agreement concerning the position of this minimum, i.e. to check if the two analyses agree on which halo masses support the most efficient star-formation. This is the subject of the next Section.

5.7 Galaxy group luminosities

5.7.1 Calculation of group luminosities

In this Section we shall convert our average group memberships to the corresponding luminosities in order to compare our results with Eke et al. 2004b and 2006. First we calculate the observed luminosity for each galaxy, using the apparent magnitude, m ($= b_j$), given by the SDSS team, i.e.

$$M_{gal/lim} = b_j^{gal/lim} - 25 - 5logd_L - \frac{z + 6z^2}{1 + \frac{8}{9}z^{2.5}}, \tag{5.5}$$

where M_{gal} and M_{lim} is the absolute magnitude of the galaxy and limiting b_j absolute magnitude of the survey at the position of this galaxy, respectively. d_L is the luminosity distance, calculated by $d_L = \frac{cz}{H_0}$, which is a good approximation for our low redshift galaxies ($H_0 = 100\text{hkms}^{-1}\text{Mpc}^{-1}$). The last term is the k-correction (Norberg et al. 2002). Then the corresponding luminosities are:

$$\frac{L_{gal/lim/*}}{L_\odot} = 10^{-0.4(M_{gal/lim/*} - M_\odot)}, \tag{5.6}$$

where $L_\odot$, $M_\odot$ are the solar luminosity and absolute magnitude and M_* ($= -19.725$) and L_* are the characteristic galaxy absolute magnitude and luminosity, respectively. Then the observed luminosity of a group is just the sum of the group galaxy luminosities, i.e.

$$\frac{L_{group}}{L_\odot} = \sum_i^n \frac{L_{gal}(i)}{L_\odot}. \tag{5.7}$$

We then correct this to include the contribution from galaxies that have luminosities below the luminosity limit (L_{lim}), at the group redshift. This is done by dividing the observed group luminosity by the incomplete Γ function, $\frac{\Gamma(\alpha+2, \frac{L_{min}}{L_*})}{\Gamma(\alpha+2)}$, where α

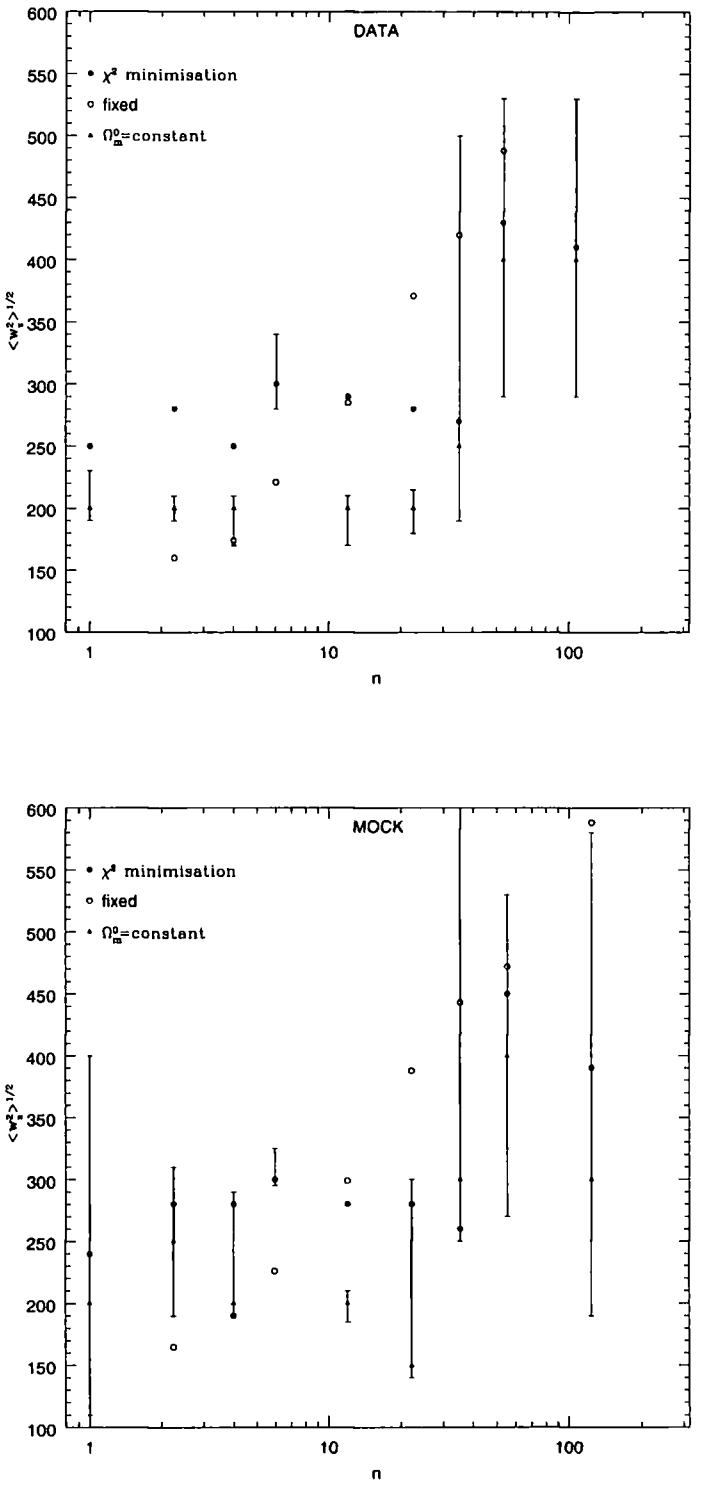

Figure 5.10: $< w_z^2 >^{1/2}$ vs membership for the data (top) and the mock (bottom) catalogues. Filled circles show the results when using χ^2 minimisation to estimate $< w_z^2 >^{1/2}$, open circles show the fixed values for $< w_z^2 >^{1/2}$ and triangles when we set $\Omega_m^0 = 0.3$ and let $< w_z^2 >^{1/2}$ vary.

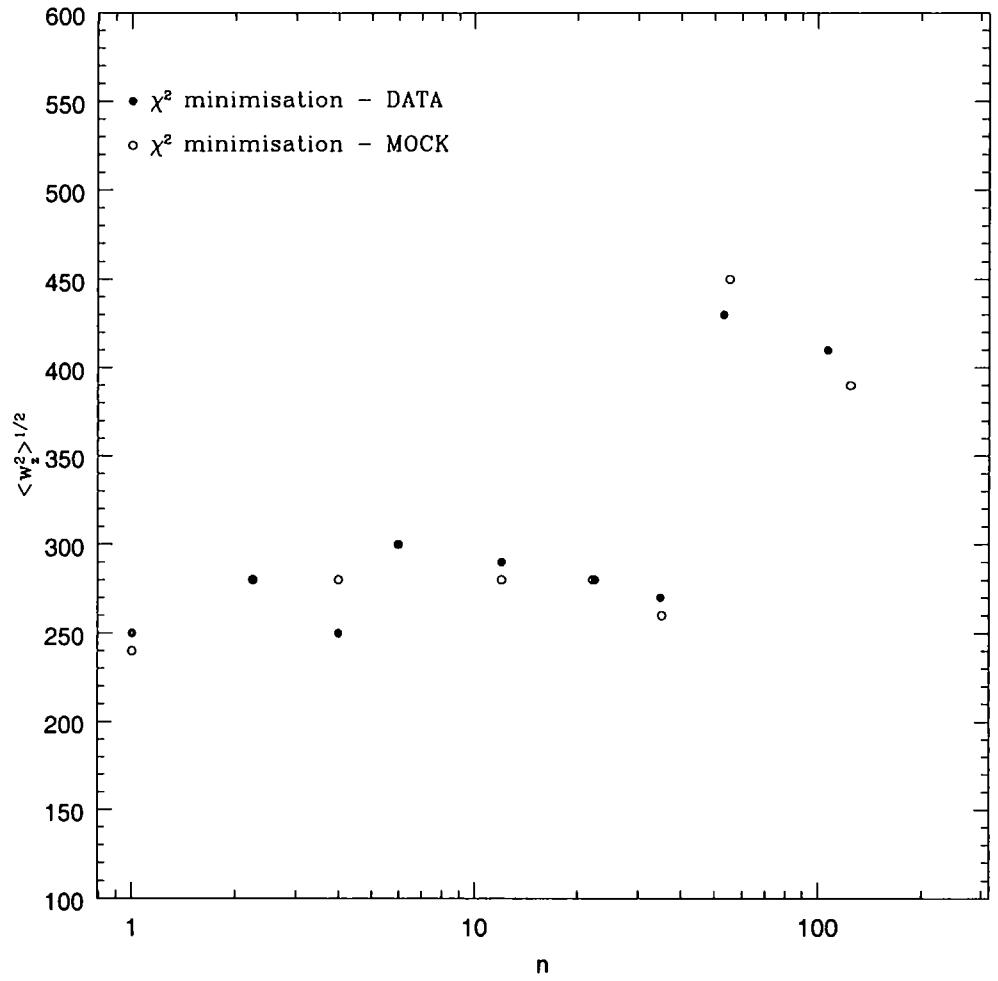

Figure 5.11: $< w_z^2 >^{1/2}$ vs membership, a comparison between the data (filled circles) and the mocks (open circles) using χ^2 minimisation to estimate $< w_z^2 >^{1/2}$. We notice the jump of the velocity dispersion for the group samples with the two largest memberships.

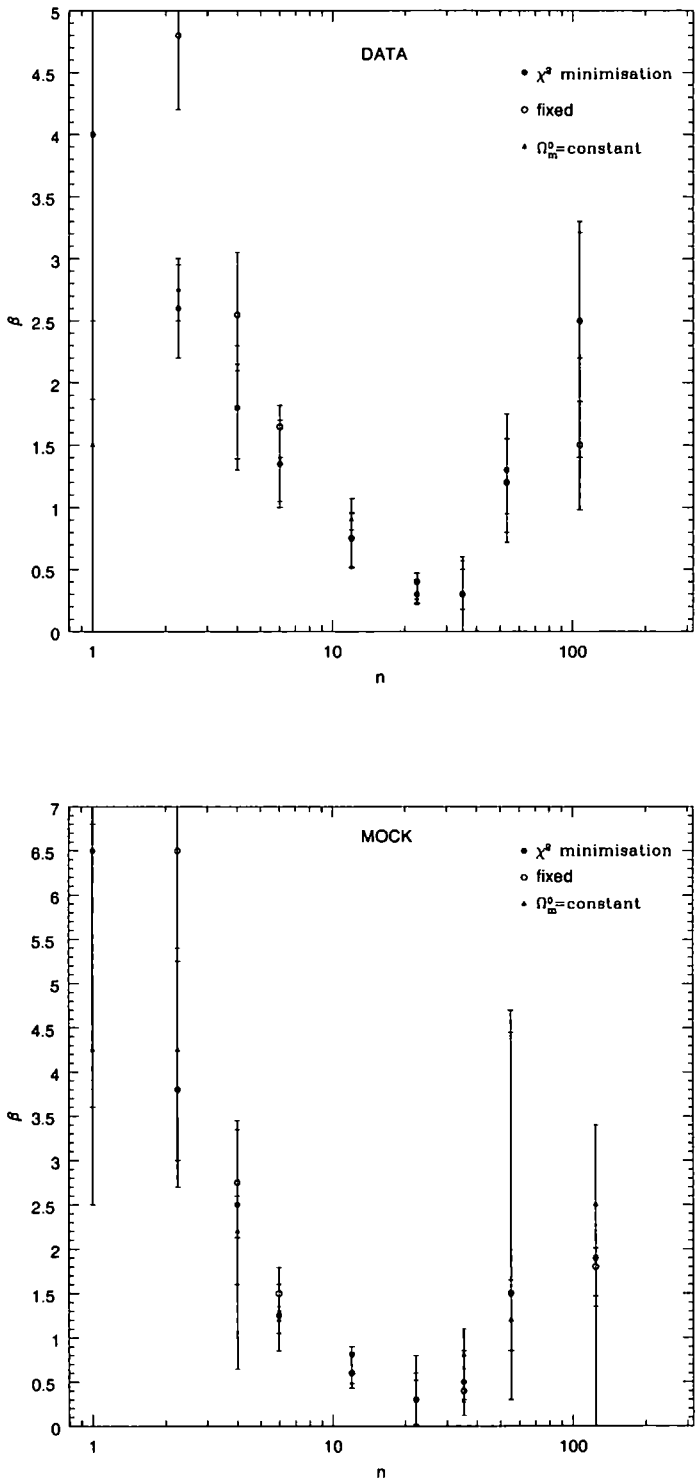

Figure 5.12: β vs membership for the data (top) and the mock (bottom) catalogues. Filled circles show the results when using χ^2 minimisation to estimate $< w_z^2 >^{1/2}$, open circles when we use the fixed values for $< w_z^2 >^{1/2}$ and triangles when we set $\Omega_m^0 = 0.3$ and let $< w_z^2 >^{1/2}$ vary.

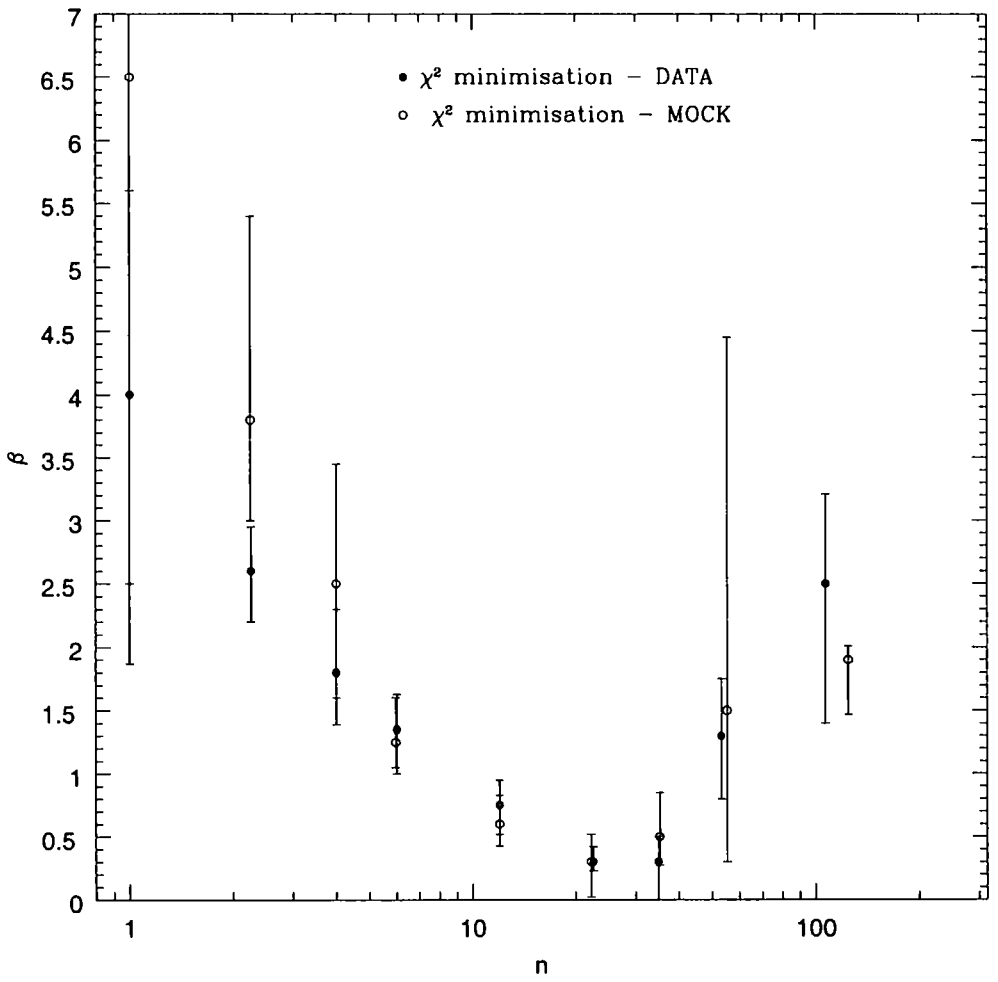

Figure 5.13: β vs membership, a comparison between the data (filled circles) and the mocks (open circles) using χ^2 minimisation to estimate $< w_z^2 >^{1/2}$.

(= −1.18, Eke et al. 2004b) is the power law index for the faint end slope (Schechter 1976).

5.7.2 Replacing the group membership with group luminosity

Fig. 5.14 shows the derived luminosities for all the groups for the data (left) and the mocks (right). Although, the ungrouped galaxies span a wide range of luminosities, especially in the case of the data, we notice that, as expected, bigger groups and clusters have bigger luminosities and their scatter is small. This can be better seen in Fig. 5.15 where we have calculated the average luminosity per group membership.

Using now the average luminosity for each group sample, as shown in Figures 5.15, we replace the membership, n, with its corresponding observed luminosity. The results are shown in Fig 5.16 for the data and the mocks. The β values shown in these Figures are those taken from the χ^2 velocity dispersions method described in the previous Section. The position of the minimum, which is what interests us, appears to be at lower luminosity for the mocks than for the data, although it may be claimed that the minimum is just flatter for the data. This difference is due to the fact that the mock catalogues contain less luminous intermediate groups and rich clusters than the data catalogues, as can be seen in Fig. 5.15. Nevertheless, we can say that the minimum appears at $\approx 10^{11}\mathrm{h}^{-2}\mathrm{L}_{\odot}$, i.e. about an order of magnitude higher than in Eke et al. results from M/L.

There are various reasons that may cause the difference between our results and those of Eke et al. Thus, in the next Section, in an attempt to better match the Eke et al. analysis, we shall re-sample our groups as a function of luminosity and estimate their M/L from velocity dispersions, in order to see if we can reproduce their results.

5.7.3 Sampling groups as a function of their luminosity

According to Eke et al. (2004b), group luminosity is the best way to rank groups in order of size especially for small groups where their luminosity can be better

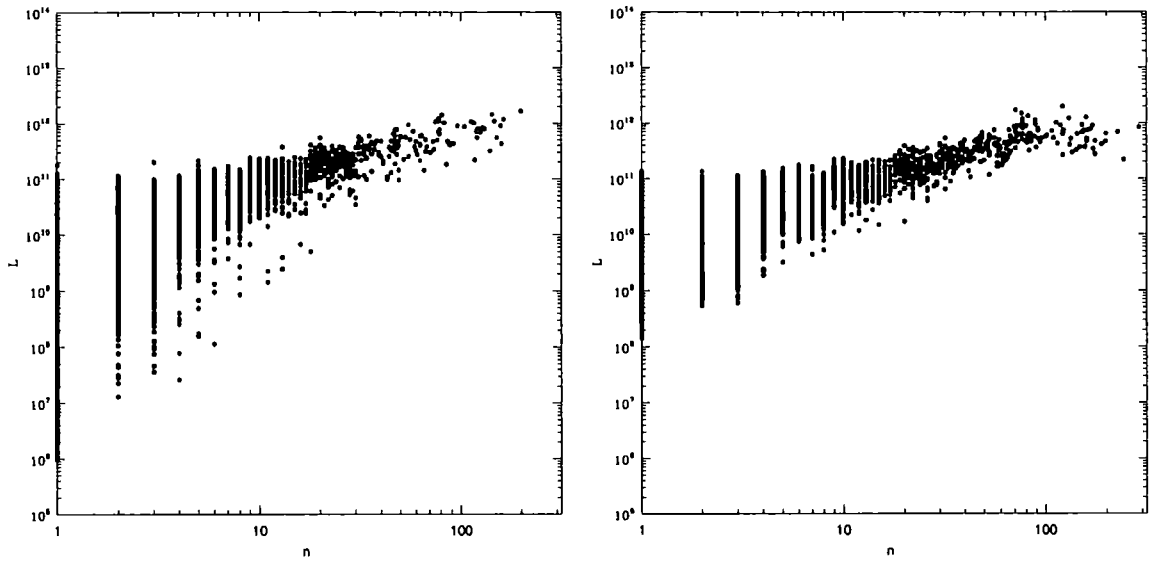

Figure 5.14: Luminosities, from the data (left) and mock (right) catalogues, for all the groups as well as for the galaxies that do not belong to groups (n=1)

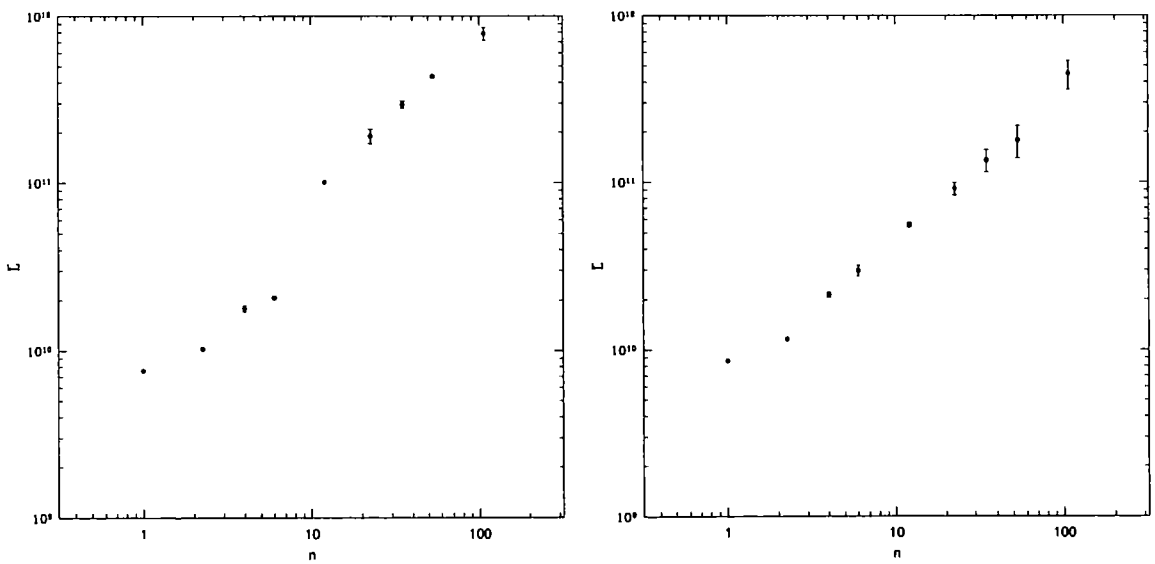

Figure 5.15: Average luminosities of our data (left) and mock (right) group samples.

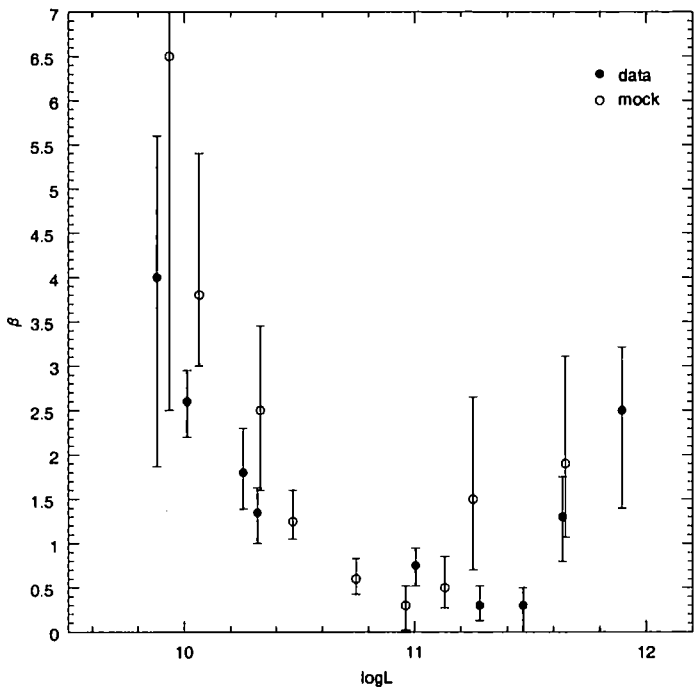

Figure 5.16: β values for different group luminosities, when we substitute the average memberships with the corresponding luminosities.

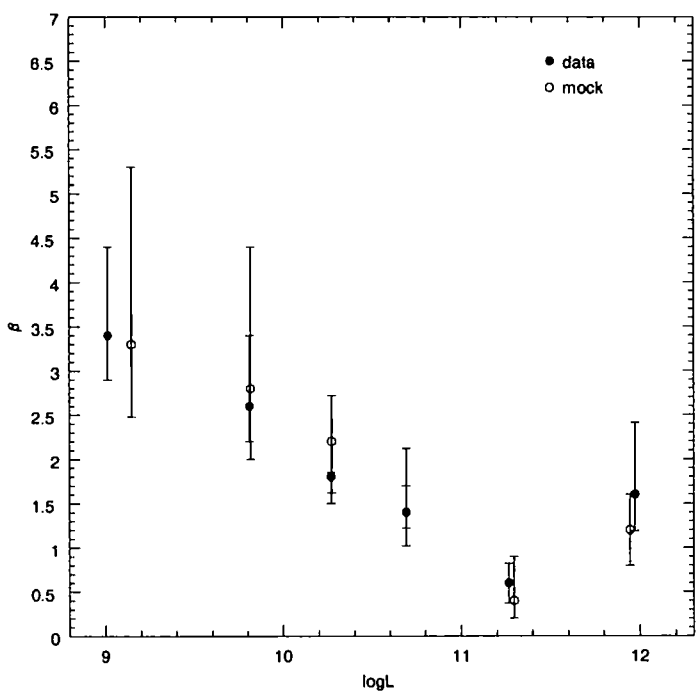

Figure 5.17: β values for different group luminosity samples, when we re-sample our groups according to their luminosities.

Table 5.6: Number of groups in the data and mock catalogues, when sampling them as a function of luminosity.

group luminosity ($h^{-2}L_{\odot}$)	data	mock
$L \leq 2 \times 10^9$	439	99
$2 \times 10^9 < L \leq 10^{10}$	2,939	2,311
$10^{10} < L \leq 3 \times 10^{10}$	7,421	6,313
$3 \times 10^{10} < L \leq 10^{11}$	4,332	3,991
$10^{11} < L \leq 6 \times 10^{11}$	745	681
$L > 6 \times 10^{11}$	28	45

Table 5.7: s_0 and γ values for the redshift-space cross-correlation functions, $\xi_{cg}(s)$, using the luminosity based analysis.

	$\xi_{cg}(s)$ fits			
	data		mock	
group luminosity ($h^{-2}L_{\odot}$)	s_0	γ	s_0	γ
$L \leq 2 \times 10^9$	2.9 ± 0.2	1.8 ± 0.1	3.3 ± 0.3	1.6 ± 0.1
$2 \times 10^9 < L \leq 10^{10}$	3.3 ± 0.1	1.9 ± 0.1	3.9 ± 0.1	1.7 ± 0.1
$10^{10} < L \leq 3 \times 10^{10}$	4.3 ± 0.1	1.5 ± 0.1	4.2 ± 0.1	1.5 ± 0.1
$3 \times 10^{10} < L \leq 10^{11}$	3.5 ± 0.2	1.7 ± 0.1	4.9 ± 0.2	1.5 ± 0.1
$10^{11} < L \leq 6 \times 10^{11}$	8.5 ± 0.2	1.5 ± 0.1	7.1 ± 0.2	1.7 ± 0.1
$L > 6 \times 10^{11}$	14.8 ± 0.8	1.5 ± 0.3	10.2 ± 0.4	1.8 ± 0.3

Table 5.8: Values of $< w_z^2 >^{1/2}$ when we divide our group samples according to their luminosity (χ^2 method).

	data		mock	
group luminosity ($h^{-2}L_\odot$)	*fixed*	χ^2	*fixed*	χ^2
$L \leq 2 \times 10^9$	102	140	130	235
$2 \times 10^9 < L \leq 10^{10}$	135	120	144	210
$10^{10} < L \leq 3 \times 10^{10}$	166	200	169	235
$3 \times 10^{10} < L \leq 10^{11}$	206	210	209	235
$10^{11} < L \leq 6 \times 10^{11}$	345	235	383	285
$L > 6 \times 10^{11}$	601	510	652	285

Table 5.9: Values of β when we divide our group samples according to their luminosity (χ^2 method).

	data	mock
group luminosity ($h^{-2}L_\odot$)	$\beta(\chi^2)$	$\beta(\chi^2)$
$L \leq 2 \times 10^9$	$3.40^{+1.00}_{-0.50}$	$3.30^{+2.00}_{-0.82}$
$2 \times 10^9 < L \leq 10^{10}$	$2.60^{+0.80}_{-0.40}$	$2.80^{+1.60}_{-0.80}$
$10^{10} < L \leq 3 \times 10^{10}$	$1.80^{+0.05}_{-0.30}$	$2.20^{+0.52}_{-0.58}$
$3 \times 10^{10} < L \leq 10^{11}$	$1.40^{+0.72}_{-0.38}$	$1.40^{+0.30}_{-0.18}$
$10^{11} < L \leq 6 \times 10^{11}$	$0.60^{+0.02}_{-0.13}$	$0.40^{+0.02}_{-0.02}$
$L > 6 \times 10^{11}$	$1.60^{+0.81}_{-0.41}$	$1.20^{+0.20}_{-0.12}$

determined than their mass (Eke et al. 2004b, Figs 3 and 4). Therefore, we rank our group samples, not by membership as we did in Section 5.2, but by luminosity. We use 6 luminosity bins as shown in Table 5.6. Then for these new group samples we measure the redshift-space cross-correlation function using the methods described in Section 5.3 (s_0 and γ values from the fits are shown in Table 5.7), the $\xi_{cg}(\sigma,\pi)$ cross-correlation function described in Section 5.6 and follow the fitting procedure described in Section 5.7 (χ^2 method), both for the data and the mock samples. We then obtain the values for the group-galaxy velocity dispersion, $< w_z^2 >^{1/2}$, and infall parameter, β, shown in Tables 5.8 and 5.9, respectively.

Fig. 5.17 shows our new β measurements. The agreement between the data and the mocks is still excellent and, as expected, we still find a minimum value for β. Nevertheless, the position of this minimum ($\approx 10^{11}\mathrm{h}^{-2}\mathrm{L}_{\odot}$) continues to be significantly higher than that found by Eke et al. (2006). In order to check the consistency of our results, in the next Section we shall calculate the M/L ratio of our group samples.

5.7.4 Mass-to-Light ratios

We now want to see how the halo mass-to-light ratios vary as a function of group luminosity. Thus, we calculate the masses of the groups, using the expression (Eke et al. 2004a)

$$M = A\frac{\sigma^2 r}{G}, \tag{5.8}$$

where σ is the group velocity dispersion (removing $85\mathrm{kms}^{-1}$ in quadrature for redshift errors, see previous Section), r is the rms projected galaxy separation of each group (Mpc/h), $A = 5.0$, as used by Eke et at. 2004a and G is the gravitational constant.

We first use for σ, the average fixed velocity dispersions for each group luminosity sample from Eke et al. (2004a), as shown in Table 5.8 and the average r for each group sample from the rms projected galaxy separation values (Mpc/h) given by the 2PIGG team. Then we repeat the estimates, replacing r by s_0 (Table 5.7) and the fixed velocity dispersion by the χ^2 fit, for σ (Table 5.8). The two estimates are shown

in Fig. 5.18 for the data (top) and the mock (bottom) catalogues, respectively. The triangles show Eke et al. results (Fig. 15 of Eke et al. 2006 for the data and Fig. 16 of Eke et al. 2004b for the mocks). As we see, data and mocks are in excellent agreement. The difference in the M/L ratios (open and filled circles) is because the s_0 values are higher than the r values. The most important feature of these Figures is the behaviour of the position of the minimum. Using the results from our analysis (s_0 and $< w_z^2 >^{1/2}$, open circles), in agreement with our previous results for β, the minimum appears at $L \simeq 2 \times 10^{11} h^{-2} L_\odot$ whereas using the fixed $< w_z^2 >^{1/2}$ and the r values from the 2PIGG team (filled circles) it appears at lower luminosities, i.e. $L \simeq 5 \times 10^{10} h^{-2} L_\odot$. This difference at the position of the minimum of the M/L ratio, is because the fixed values for $< w_z^2 >^{1/2}$ show a jump for the two most luminous group samples, resulting in larger masses for those whereas the values for $< w_z^2 >^{1/2}$ using the χ^2 minimisation remains roughly the same for all the group samples, as shown in Table 5.8. Therefore, the minimum using these fixed $< w_z^2 >^{1/2}$ values appears at our third most luminous group rather the second.

Although using the Eke et al. (2004a) velocity dispersion and group sizes has reduced the discrepancy in the position of the M/L minimum by a factor of ~ 3 a difference of a factor of 8 between the M/L and β minima still persists. Investigating this further we now use, instead of average mass and luminosity values for each group, their median values. The results are shown in Fig. 5.19 for the data (top) and the mock (bottom), respectively. We notice that there are differences between the two methods. The average values have slightly higher M/L values but most importantly the minimum in the M/L ratio, when we use the median values, appears at smaller luminosities. Actually now, comparing those two plots with Fig. 15 in Eke et al. 2006 for the data, and Fig. 16 in Eke et al. 2004b for the mocks we see that we reproduce all the features of the plots of the 2PIGG team. More specifically, M/L ratio increases by a factor of 5 when spanning luminosities from $10^{10} - 10^{12} h^{-2} L_\odot$ and shows a minimum at $\approx 5 \times 10^9 h^{-2} L_\odot$ in excellent agreement with the position of the minimum as found by the 2PIGG team.

5.7.5 Reasons for the difference in $\frac{M}{L}$ and β minima

Summarising the reasons for the difference in the position of the minima between $\beta(L)$ and $\frac{M}{L}(L)$, we note that there are already different minima shown by $\frac{M}{L}(L)$ depending on whether median or average $\frac{M}{L}(L)$ values are used. When the median $\frac{M}{L}(L)$ is used, the position of the minimum decreases by a factor of ~ 8 in L. These conclusions also apply when assuming the velocity dispersions of Eke et al. (2004a) instead of our χ^2 fitted values (3× lower). Thus, if the χ^2 fitted velocity dispersion and average M/L are used the position of the minimum of the M/L moves up in L and appears at the same luminosities as in β. Eke et al. (2004b) claim that the simulations suggest the use of the median in the velocity dispersion fits. If the simulations are correct then this would imply that the position of the β minimum in L is either due to other physical effects or that we shouldn't be using average values for β. The other physical effects include the suggestion that the $\frac{M}{L}$ and β results may apply to different scales around the cluster. There also remain questions as to whether it is fair to compare $\frac{M}{L}$ estimates with $\beta \sim \frac{1}{b} \sim \delta\rho_{mass}/\delta\rho_{galaxies}$.

5.8 Discussion + Conclusions

Using the 2PIGG galaxy group catalogue we have investigated the behaviour of the infall parameter β for group-galaxies of different membership, as well as their rms velocity dispersions via the redshift distortion of the group-galaxy cross-correlation functions.

We first separated our galaxy group set into subsamples, following approximately the Eke et al. 2004a membership classes. We also used mock catalogues, created by the 2PIGG team, and we applied the same membership classification to them, in order to compare our results from the data sets with those from the mock catalogues.

We cross-correlated these group samples with 2dFGRS galaxies, in order to measure the redshift-space, $\xi_{cg}(s)$, the semi-projected, $w_p(\sigma)/\sigma$ and the real-space, $\xi_{cg}(r)$, cross-correlation functions. For each of them, we fitted a power law, e.g. $\xi_{cg}(r) = (r/r_0)^{-\gamma}$. In agreement with previous studies, we noticed that the correlation amplitude increased, both for the data and the mocks, as we moved to

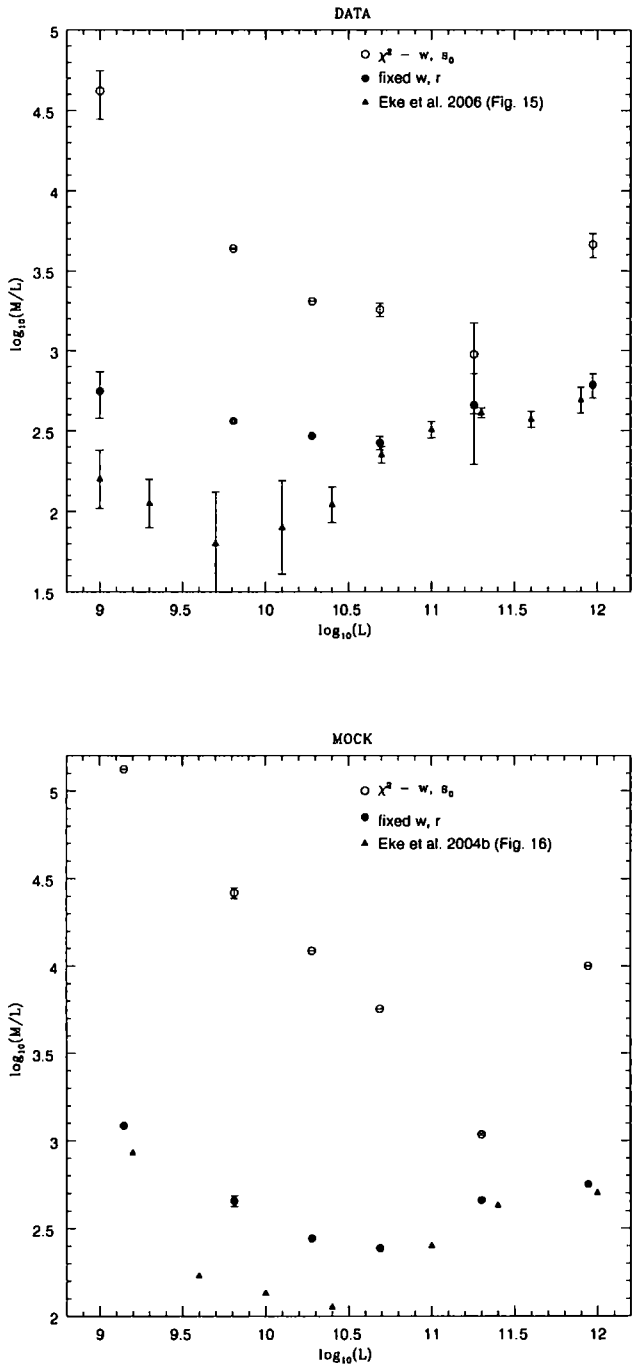

Figure 5.18: Average M/L ratio for each one of our data (top) and mock (bottom) group luminosity samples. Filled circles show the results when we use the fixed values for the velocity dispersion and the values for the rms projected galaxy separation, as given by the 2PIGG team. Open circles show the average M/L ratio using our χ^2 measurements for the velocity dispersion of each group and the s_0 values estimated from fits to the redshift-space cross-correlation function. Triangles show Eke et al. results (2006-top, 2004b-bottom).

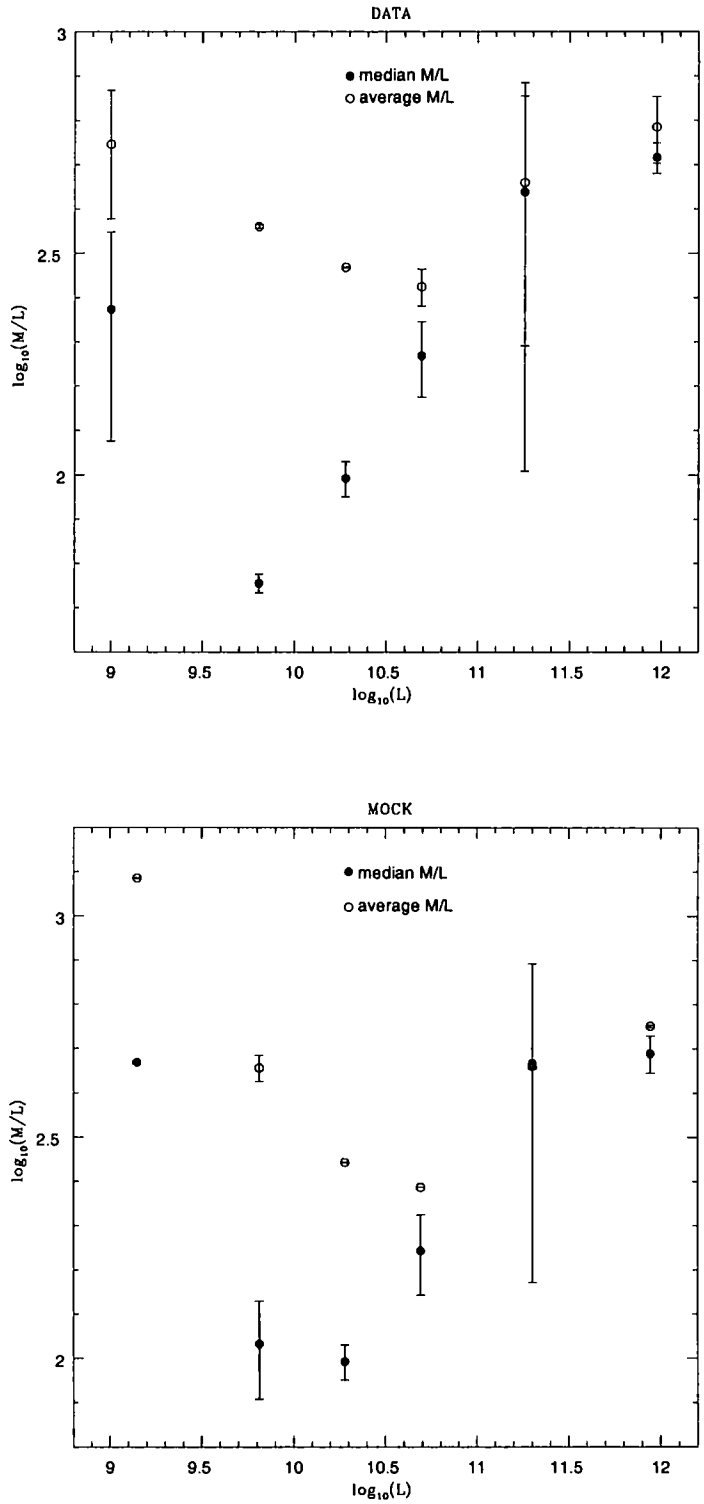

Figure 5.19: A comparison between the average (open circles) and the median (filled circles) values of the M/L ratio for each one of our data (top) and mock (bottom) group luminosity samples. The median values move the minimum of the ratio to 10× lower group luminosities.

richer groups. Also, the redshift-space cross-correlation amplitude and slope are statistically in agreement with those from the real-space cross-correlation function. Comparing the data and the mock for each of the cross-correlation functions, we noticed that, they are all in agreement, especially the results from the redshift-space function, which is the least noisy.

Next, we measured the $\xi_{cg}(\sigma, \pi)$ cross-correlation function and used its shape and the s_0 and γ from the $\xi_{cg}(s)$ fits to model the redshift-space distortions and measured the χ^2 group-galaxy rms velocity dispersion, $< w_z^2 >^{1/2}$, and the infall parameter, β. Our measurements showed that $< w_z^2 >^{1/2}$ remains roughly constant for small and intermediate group-galaxies and rises for clusters whereas the values of $< w_z^2 >^{1/2}$, estimated by the 2PIGG team increase with increased group membership. The β results for the data and the mocks are in very good agreement and show a minimum for the dynamical infall at intermediate group memberships.

Prompted by previous studies of group M/L ratios as a function of their luminosities, in the last Section we calculated the average luminosities for each of our group samples and replaced the group memberships with their corresponding luminosities. This revealed a discrepancy of more than an order of magnitude in the position of the minimum between β and M/L. In order to examine this discrepancy we re-sampled our groups using as a criterion their luminosity instead of their membership and calculated their M/L ratios. This analysis revealed that the reasons for the difference in the position of this minimum is due to the different velocity dispersion measurements between us and Eke et al. (2004b) and most importantly due to the use of median instead of average values.

Our overall conclusion is that bias estimates from dynamical infall broadly appear to support the minimum in star-formation efficiency at intermediate halo masses and also that there may be slight differences with mock catalogues. However, there is a systematic shift between the M/L and $\beta(\propto \frac{1}{b})$ minima. Judged by the mock results, the use of the median values rather than the average seems to give more accurate M/L results. Unfortunately, there is no option to use a median rather than an average β for the z-distortion results. There is also the possibility that the mock M/L with L has been mis-estimated by Eke et al. 2004b, since this involves

friends-of-friends routines applied to define halo masses and then independently to find group luminosities and the process of matching the two is not without its complications. More work is therefore needed on the DM mocks to check further the reasons for this difference in interpretation. However, it may be more likely that our larger scale estimates of β measure a different aspect of the galaxy mass-luminosity relation than the small scale σ measurements. Also there may remain issues about the validity of comparing the dynamical infall parameter $\beta(\sim \frac{1}{b} \sim \delta\rho_{mass}/\delta\rho_{galaxies})$ with the $\frac{M}{L}$ ratio from the velocity dispersions.

Finally, the results presented here seem to be in agreement with our previous QSO-galaxy group lensing results (Myers et al. 2003, Mountrichas & Shanks 2007). There we found that $n \geq 7$ groups showed large effective masses and galaxies also showed an effective anti-bias of $b \approx 0.2$ or $\beta \approx 2.5$. These $n \geq 7$ groups have luminosities which places them at $\sim 5 \times 10^{10} L_{\odot}$. In Fig. 5.17 they, thus, would appear to have a higher β than those at minimum, in agreement with the lensing conclusions. Moreover individual galaxies appear to have $\beta \sim 3$ or $b \sim 0.15$ again in agreement with the conclusion for the galaxy lensing results of Myers et al. 2005. The only surprise is that the mock catalogues show similar behaviour. This suggests that such large β variations might be expected even in standard galaxy formation models.

Chapter 6

Conclusions

6.1 Summary

Observational cosmology has made remarkable progress over the last few years. Surveys described and used in this thesis, such as the 2QZ, 2SLAQ, 2dFGRS and SDSS have provided us a large amount of data. The use of these datasets has made it possible to greatly improve the statistical significance of our measurements and put stronger constraints on cosmological parameters. It is also impressive that the results from these measurements are in such a good agreement with those from the CMB (WMAP, Spergel et al. 2007). This great success of observational evidence has led to the verification of theoretical predictions as well as bringing new challenges to theoretical models. The combination of these observational estimates brings us to the era of the so-called precision cosmology. Recent measurements appear to indicate that the universe is flat ($\Omega = 1.02 \pm 0.02$) and dominated by matter and dark energy ($\Omega_m = 0.27 \pm 0.04$, $\Omega_\Lambda = 0.73 \pm 0.04$), while the baryonic matter is only $\Omega_b = 0.044 \pm 0.004$ (Bennett et al. 2003b). Nevertheless, the great achievements of modern cosmology should not create the impression that there are not still open issues, like the formation and evolution of large-scale structure, the estimation of the Hubble constant and the exact composition of the universe.

The aim of this thesis was to analyze statistically the available large QSO, LRG, galaxy and cluster samples in order to estimate the QSO-galaxy lensing anti-correlation signal and measure the mass of foreground galaxies and clusters and to

estimate the QSO-LRG clustering amplitude, the QSO bias and their dependence on QSO luminosity. The high redshift QSO– low redshift galaxy results naturally led to our investigation of the behaviour of the group-galaxy infall parameter and their rms velocity dispersions for different group memberships. The aim here was to make dynamical estimates of the group masses to check the QSO lensing results.

6.2 Main results–conclusions

6.2.1 QSO lensing

Having described the QSO and galaxy samples in Chapter 2, in Chapter 3 we used a photometric SDSS QSO sample and cross-correlated it with galaxies ($g < 21$). Our results are in agreement with Myers et al. (2005), at least on scales larger than $1'$. The results of Scranton et al. (2005) showed a smaller anti-correlation signal but this is expected because of their fainter galaxy sample ($r < 21$). The same pattern is repeated in the case of QSO-galaxies in clusters cross-correlations, i.e the results are consistent with Myers et al. (2003) but at considerably higher S/N than for galaxies. Taking into consideration the low-redshift contamination in the $1.0 < z_p < 2.2$ photometric QSO sample ($\approx 2\%$ for $z_s < 0.3$ and $\approx 4\%$ for $z_s < 0.6$) as estimated by comparing the photometric sample with spectroscopic datasets; and comparing the autocorrelation results from $g < 21$ and $r < 21$ galaxies we modified the Myers et al. (2005) results and found that they are actually in very good agreement with those of Scranton et al. Therefore when we account for those two effects, we consider that the Scranton et al. SDSS results at faint magnitudes provide strong observational confirmation of the results of Myers et al. (2005).

At bright magnitudes the contamination correction lowers the Scranton et al. signal, at a marginally significant level, but still at an appropriate amplitude to match the anti-correlation signal at fainter magnitudes. The strong anti-correlation seen at QSO limit $g < 21$ suggests that the relevant slope for $g < 19$ QSO samples is close to the critical slope found at $19 < g < 20$, i.e. little positive correlation is expected in this magnitude range.

Since the Scranton et al. and Myers et al. results are in agreement, it is still an

open question why the latter require a strong anti-bias ($b \approx 0.1$) whereas the former suggest $b \approx 0.6 - 1$.

6.2.2 QSO-LRG clustering

In Chapter 4 we performed an analysis of the clustering of QSOs with LRGs. For this purpose we have used three spectroscopic QSO samples, i.e. 2QZ, 2SLAQ and SDSS and one spectroscopic (2SLAQ) LRG sample. Moreover we used two larger photometric LRG samples from 2SLAQ and AAOmega. First, we used the 2-point angular cross-correlation function, $w(\theta)$, and measured the QSO-LRG cross-correlation for different QSO luminosities. The results showed that there is little cross-correlation dependence on QSO luminosity.

Next, we measured the redshift-space cross-correlation function. For these measurements we also used Limber's formula to fit r_0 to 2-D photometric results. The fits for r_0 from 3-D $\xi(s)$ are in very good agreement with the fits to the 2-D $w(\theta)$ results. Both indicate that there is little QSO-LRG clustering dependence on QSO luminosity.

We also compared our QSO-LRG clustering results with 2SLAQ LRG-LRG (Ross et al. 2007) and 2QZ+2SLAQ QSO-QSO (da Ângela et al. 2008) clustering results. We noted that on small scales, the QSO-QSO and QSO-LRG results appear flatter. As confirmed later by the $w_p(\sigma)/\sigma$ measurements, this is due to the larger QSO redshift errors (broad-lines). On larger scales ($\geq 5\mathrm{h}^{-1}\mathrm{Mpc}$) the QSO-QSO correlation amplitude appears lower than the QSO-LRG and LRG-LRG amplitudes.

The results from the semi-projected cross-correlation function, $w_p(\sigma)/\sigma$, are in agreement with our $\xi(s)$ observations giving consistent r_0 and γ values. The comparison with 2SLAQ LRG-LRG (Ross et al. 2007) and 2QZ+2SLAQ QSO-QSO (da Ângela et al. 2008) confirms our results from redshift-space. The real-space cross-correlation function, also seems to agree with the $\xi(s)$ and $w_p(\sigma)/\sigma$, although it is noisier.

We then measured the $\xi(\sigma, \pi)$ cross-correlation function and used two different models to model the redshift-space distortions. The two models gave consistent results with each other and between the different samples. The redshift-space dis-

tortions yielded an average of $\beta_Q = 0.55 \pm 0.10$, $b_Q = 1.4 \pm 0.2$ at $z = 0.55$ which is slightly higher than $b_Q = 1.1 \pm 0.2$ at $z \simeq 0.6$ from da Ângela et al.

Following an amplitude analysis we measured the integrated cross-correlation function for each of our QSO-LRG samples. We noted no evidence for QSO-LRG clustering dependence on QSO luminosity. Using LRG bias, as estimated by previous studies, we then calculated the QSO bias, b_Q. In this case there were indications of luminosity dependence, in the sense that b_Q may reduce as we move to brighter QSO samples; this is in the opposite sense to what is expected in high peaks biasing models. Our amplitude analysis yielded a $b_Q = 1.5 \pm 0.1$ (at $M_{bj} \approx -23$) which is in very good agreement with our results from redshift-space distortions.

Finally, using the relation between bias and M_{DMH} suggested by Sheth et al. (2001), we calculated the corresponding masses of the QSO hosts. QSO halo masses were estimated to be $\sim 10^{13} \mathrm{h}^{-1} \mathrm{M}_{\odot}$ at $z \approx 0.55$. Our M_{DMH} estimates are higher than those from Croom et al. 2005 and da Ângela et al. 2008 (at $z = 1.4$) and may be explained by long-lived QSO population models.

The main result of this Chapter is that the QSO bias values are independent of QSO luminosity, at fixed redshift.

6.2.3 Cluster-galaxy clustering

In Chapter 5 we cross-correlated 2PIGG galaxy groups of different membership with 2dFGRS galaxies, in order to measure the redshift-space, $\xi_{cg}(s)$, the semi-projected, $w_p(\sigma)/\sigma$, and the real-space, $\xi_{cg}(r)$, cross-correlation functions. In each case, we fitted a power law, e.g. $\xi_{cg}(r) = (r/r_0)^{-\gamma}$. We also used mock catalogues, created by the 2PIGG team, and we applied the same membership classification to them. In agreement with previous studies, we noticed that the correlation amplitude increased, both for the data and the mocks, as we moved to richer groups. Also, the redshift-space cross-correlation amplitude and slope are statistically in agreement with those from the real-space cross-correlation function. Comparing the data and the mock for each of the cross-correlation functions, we noticed that, they are all in agreement, especially the results from the redshift-space function, which is the least noisy.

Next, we measured the $\xi_{cg}(\sigma,\pi)$ cross-correlation function and used its shape and the s_0 and γ from the $\xi_{cg}(s)$ fits to model the redshift-space distortions and measured the χ^2 group-galaxy rms velocity dispersion, $< w_z^2 >^{1/2}$, and the infall parameter, β. Our measurements showed that $< w_z^2 >^{1/2}$ remains roughly constant for small and intermediate group-galaxies and rises for clusters whereas the values of $< w_z^2 >^{1/2}$, estimated by the 2PIGG team increase with increased group membership. The β results for the data and the mocks are in very good agreement and show a minimum for the dynamical infall at intermediate group memberships.

Prompted by previous studies of group M/L ratios as a function of their luminosities (Eke et al. 2006), we then calculated the average luminosities for each of our group samples and replaced the group memberships with their corresponding luminosities. This revealed a discrepancy of more than an order of magnitude in the position of the minimum between β and M/L. In order to examine this discrepancy we re-sampled our groups using as a criterion their luminosity instead of their membership and calculated their M/L ratios. This analysis revealed that the reasons for the difference in the position of this minimum is due to the different velocity dispersion measurements between us and Eke et al. and most importantly due to the use of median instead of average values.

Our overall conclusion is that bias estimates from dynamical infall broadly appear to support the minimum in star-formation efficiency at intermediate halo masses and also that there may be slight differences with mock catalogues. However, there is a systematic shift between the M/L and $\beta(\propto \frac{1}{b})$ minima. Judged by the mock results, the use of the median values rather than the average seems to give more accurate M/L results. There is also the possibility that the mock M/L with L has been mis-estimated by Eke et al. 2004b, since this involves friends-of-friends routines applied to define halo masses and then independently to find group luminosities and the process of matching the two is not without its complications. More work is therefore needed on the DM mocks to check further the reasons for this difference in interpretation. However, it may be more likely that our larger scale estimates of β measure a different aspect of the galaxy mass-luminosity relation than the small scale σ measurements. Also there may remain issues about the validity of comparing

the dynamical infall parameter $\beta(\sim \frac{1}{b} \sim \delta\rho_{mass}/\delta\rho_{galaxies})$ with the $\frac{M}{L}$ ratio from the velocity dispersions.

Finally, these results seem to be in agreement with our previous QSO-galaxy group lensing results (Chapter 3). There we found that $n \geq 7$ groups showed large effective masses and galaxies also showed an effective anti-bias of $b \approx 0.2$ or $\beta \approx 2.5$. These $n \geq 7$ groups have luminosities which place them at $\sim 5 \times 10^{10} L_{\odot}$. In Fig. 5.17 they, thus, would appear to have a higher β than those at minimum, in agreement with the lensing conclusions. Moreover individual galaxies appear to have $\beta \sim 3$ or $b \sim 0.15$ again in agreement with the conclusion for the galaxy lensing results of Myers et al. 2005. The only surprise, at least to us as observers, is that the mock catalogues show similar behaviour. This suggests that such large β variations might be expected even in standard galaxy formation models.

6.3 Future prospects

This thesis demonstrates the importance of gravitational lensing and redshift-space distortions in the statistical analysis of large datasets of QSOs, LRGs, galaxies and clusters. Gravitational lensing is a useful tool to measure mass associated with galaxies and galaxy groups. Clustering measurements and the dynamical effects superimposed on them reveal to us the dynamics of the universe as well as the geometry and evolution of large-scale structure.

Large (spectroscopic) QSO samples, which will be available in the future, will provide us with QSOs at different redshifts and magnitudes. Thus, lensing measurements will become even more robust. In addition, large bright QSO samples will make it possible, perhaps, to significantly detect the positive QSO-galaxy and QSO-galaxy group cross-correlation signal expected in the steep part of the QSO count slope.

These QSO samples, as well as, LRG samples at higher redshifts will also provide us with enough data to study further the dependence of QSO bias on redshift and QSO luminosity. These, in turn, will improve our understanding on QSO evolution and feedback mechanisms. Furthermore, new and more accurate models for

the dynamical distortions in $\xi(\sigma, \pi)$ can be developed and provide us with better constraints on basic cosmological parameters, such as Ω_m and β.

Finally, new galaxy surveys and higher resolution N-body simulations of cosmological volumes as well as semi-analytical models of galaxy formation will help us construct even more precise mock catalogues and study the dynamics of galaxies and clusters on different scales.

Bibliography

[1] Alcock, C., Paczynski, B., 1979, Nature, 281, 358

[2] Ballinger, W. E., Peacock, J. A., Heavens, A. F., 1996, MNRAS, 282, 877

[3] Bardeen, J.M., Bond, J.R. Kaiser, N., Szalay, A. S., 1986, ApJ, 304, 45

[4] Bartelmann, M., 1996, A & A, 313, 697

[5] Beers, T. C., Flynn, K., Gebhardt, K., 1990, AJ, 100, 32B

[6] Bennett, C. L., 2003a, ApJS, 170, 377S

[7] Bennett, C. L., 2003b, ApJS, 148, 97B

[8] Borgani, S., Plionis, M., Kolokotronis, V., 1999, MNRAS, 305, 866

[9] Boyle, B. J., Shanks, T., Peterson, B. A., 1988, MNRAS, 235, 935

[10] Broadhurst, T., Lehar, J., 1995, ApJ, 450, L41

[11] Cannon, R., et al., 2006, MNRAS, 372, 425

[12] Carroll, S. M., 2001, LRR, 4, 1C

[13] Coil A.L., Hennawi J.F., Newman J.A., Cooper M.C., Davis M. 2007, ApJ, 654, 115

[14] Cole, S., Lacey, C. G., Baugh, C. M., Frenk, C. S., 2000, MNRAS, 319, 168

[15] Colin, P., Klypin, A.A., Kravstov, A.V. & Khokhlov, A.M. 1999, ApJ, 523, 32

[16] Croft, R. A. C., Dalton, G. B., Efstathiou, G., Sutherland, W. J., Maddox, S. J., 1997, MNRAS, 291, 305

[17] Croom, S. M., Shanks, T., 1996, MNRAS, 281, 893

[18] Croom, S. M., Shanks, T., 1999, MNRAS, 307, L17

[19] Croom, S. M., et al., 2001, MNRAS, 325, 483

[20] Croom, S. M., Boyle, B. J., Loaring, N. S., Miller, L., Outram, P. J., Shanks, T., Smith, R. J., 2002, MNRAS, 335, 456

[21] Croom, S. M., Smith, R. J., Boyle, B. J., Shanks, T., Miller, L., Outram, P.J., Loaring, N. S., 2004 MNRAS, 349, 1397

[22] Croom, S. M., et al., 2005, MNRAS, 356, 415

[23] Cunha, K., Smith, V. V., 2006ApJ, 651, 491C

[24] da Ângela, J., Outram, P. J., Shanks, T., Boyle, B. J., Croom, S. M., Loaring, N. S.; Miller, L., Smith, R. J. 2005, MNRAS, 360, 1040

[25] da Ângela, J., Outram, P. J., Shanks, T., 2005, MNRAS, 361, 879

[26] da Ângela, J. et al., 2008, MNRAS, 383, 565D

[27] da Ângela J., 2006, Ph.D. Thesis, Durham University

[28] Davis, M., Peebles, P. J. E., 1983, ApJ, 267, 465

[29] Efstathiou, G., 1988, Proceedings of the Third IRAS Conference, Queen Mary College, London, England, July 6-10, 1987. Lecture Notes in Physics, Vol. 297, edited by A. Lawrence. Springer-Verlag, Berlin, 1988., p.312

[30] Eisenstein, D. J., et al., 2001, AJ, 122, 2267

[31] Eisenstein, D. J., et al., 2005, ApJ, 633, 560

[32] Eke, V. R., et al., 2004a, MNRAS, 348, 866

[33] Eke, V. R., et al., 2004b, MNRAS, 355, 769

[34] Eke, V. R., Baugh, C. M., Cole, S., Frenk, C. S., Navarro, J. F., 2006, MNRAS, 370, 1147

[35] Gaztanaga, E, 2003, ApJ, 589, 82

[36] Geller, M. J., de Lapparent, V., Kurtz, M. J, 1984, ApJ, 287L, 55G

[37] Georgantopoulos, I., Shanks, T., 1994, MNRAS, 271, 773

[38] Giuricin, G., Samurovi, S., Girardi, M., Mezzetti, M., Marinoni, C., 2001, ApJ, 554, 857G

[39] Guimaraes, A.C.C., Myers, A.D., Shanks, T., 2005, MNRAS, 362, 657

[40] Gunn, J. E., 2006, AJ, 131, 2332G

[41] Hamilton, A. J. S., 1993, ApJ, 417, 19

[42] Hawkins, et al., 2003, MNRAS, 346, 78

[43] Hirata C. M., Seljak U., 2004, Phys. Rev. D, 70, 063526

[44] Hoyle, F., 2000, PhD Thesis, University of Durham

[45] Hoyle, F., Outram, P. J., Shanks, T., Boyle, B. J., Croom, S. M., Smith, R. J., 2002, MNRAS, 332, 311

[46] Jain, B., Scranton, R. & Sheth, R.K., 2003 MNRAS, 345, 62

[47] Jenkins, A., Frenk, C. S., Pearce, F. R., Thomas, P. A., Colberg, J. M., White, S. D. M., Couchman, H. M. P., Peacock, J. A., Efstathiou, G., Nelson, A. H., 1998, ApJ, 499, 20

[48] Kaiser, N., 1987, MNRAS, 227, 1

[49] Lacey, C., Cole, S., 1993, MNRAS, 262, 627

[50] Landy, S. D., Szalay, A. S., 1993, ApJ, 412, 64

[51] Lewis, I. J., et al. 2002, MNRAS, 333, 279L

[52] Limber, D. N. 1953, ApJ, 117, 134

[53] Loveday, J., Maddox, S. J., Efstathiou, G., Peterson, B. A., 1995, ApJ, 442, 45L

[54] Loveday, J., Peterson, B. A., Maddox, S. J., Efstathiou, G., 1996, ApJS, 107, 201

[55] Maoz, D., Rix, H. W., Gal-Yam, A., Gould, A., 1997, AJ, 486, 75

[56] Matsubara, T., Suto, Y., 1996, ApJL, 470 L1+

[57] Matsubara, T., Szalay, A. S., 2001, ApJL, 556, L67

[58] Mellier, Y., Meylan G., 2005, Gravitational Lensing Impact on Cosmology (S225), Edited by Yannick Mellier and Georges Meylan, pp. . ISBN 0521851963. Cambridge, UK: Cambridge University Press, 2005

[59] Mo, H. J., White, S. D. M., 1996, MNRAS, 282, 347

[60] Mountrichas, G., Shanks T., 2007, MNRAS, 380, 113M

[61] Mountrichas, G., Shanks T., 2007, submitted to MNRAS, astro-ph/0712.3255

[62] Mountrichas, G., Shanks T., Croom, S.M, Sawangwit, U., Schneider D. P., Myers A. D., Pimbblet K., Drinkwater M., 2008, submitted to MNRAS, astro-ph/0801.1816

[63] Myers, A. D., 2003, PhD Thesis, University of Durham

[64] Myers, A. D., Outram, P. J., Shanks, T., Boyle, B. J., Croom, S. M., Loaring, N. S., Miller, L., Smith, R. J., 2003, MNRAS, 342, 467

[65] Myers, A. D., Shanks, T., Boyle, B. J., Croom, S. M., Loaring, N. S., Miller, L. & Smith, R. J. 2005, MNRAS, 359, 741.

[66] Myers A.D., Brunner R.J., Richards G.T., Nichol R.C., Schneider D.P., Vanden Berk D.E., Scranton R., Gray A.G., Brinkmann J., 2006, ApJ, 638, 622

[67] Myers, A. D., Brunner, R. J., Richards, G. T., Nichol, R. C., Schneider, D. P., Bahcall, N. A., 2007, ApJ, 658, 99M

[68] Myers, A.D. et al., 2007, ApJ, 658, 85M

[69] Narayan, R., 1989ApJ, 339L, 53N

[70] Navarro, J. F., Frenk, C. S., White, S. D. M., 1995, ApJ, 275, 720

[71] Navarro, J. F., Frenk, C. S., White, S. D. M., 1996, ApJ, 462, 563N

[72] Navarro, J. F., Frenk, C. S., White, S. D. M., 1997, ApJ, 490, 493

[73] Nollenberg, J. G., Williams, L. L. R., 2005, ApJ, 634, 793

[74] Norberg, et. al., 2002, MNRAS, 336, 907

[75] Outram, P. J.; Hoyle, Fiona; Shanks, T., 2001, MNRAS, 321, 497

[76] Padilla, N. D., Merchan, M. E., Valotto, C. A., Lambas, D. G., Maia, M. A. G., 2001, ApJ, 554, 873P

[77] Padilla, N. D., et al., 2004, MNRAS, 352, 211P

[78] Padmanabhan, N., White, M., Eisenstein, D. J., 2006, American Astronomical Society Meeting 209, Vol. 38, p.1063

[79] Peacock, J. A., et al., 2001, Nature, 410, 169

[80] Peebles, P. J. E., 1973, ApJ, 185, 413P

[81] Peebles, P. J. E., 1979, MNRAS, 189, 89

[82] Peebles, P. J. E., 1980, The large scale structure in the Universe, Princeton Univeristy Press, ISBN 0-691-08240-5

[83] Peebles, P. J. E., 1984, ApJ, 284, 439

[84] Percical, W., et al., 2006AAS, 208, 6802P

[85] Phillipps, S., Fong, R., Fall, R. S., Ellis S. M., MacGillivray, H. T., 1978, MNRAS, 182, 673

[86] Porciani C., Magliocchetti M., Norberg P. 2004, MNRAS, 355, 1010

[87] Porciani, C., Norberg, P., 2006, MNRAS, 371, 1824

[88] Prescott, M. K. M., Impey, C. D., Cool R. J., Scoville, N.Z., 2006, ApJ, 644, 100

[89] Ratcliffe, A., Shanks, T., Broadbent, A., Parker, Q. A., Watson, F. G., Oates, A. P., Fong, R., Collins, C. A., 1996, MNRAS, 281L, 47R

[90] Ratcliffe, A., Shanks, T., Parker, Q. A., Fong, R., 1998, MNRAS, 296, 191

[91] Richards, G. T., et al., 2004, ApJS, 155, 257

[92] Richards, G. T., et al., 2005, MNRAS, 360, 839

[93] Robotham, A., Wallace, C., Phillipps, S., De Propris, R., 2006, ApJ, 652, 1077R

[94] Ross, N. P., et al., 2007, MNRAS, 381, 573

[95] Ross, N. P., Shanks, T., Cannon, R. D., Wake, D. A., Sharp, R. G., Croom, S. M., Peacock, John A., astro-ph/0704.3739, submitted to MNRAS

[96] Rubin, V. C., 1954, Proc. N.A.S., 40, 541

[97] Saunders, W., Rowan-Robinson, M., Lawrence, A., 1992, MNRAS, 258, 134

[98] Schechter, P., 1976, ApJ, 203, 297S

[99] Scranton, et al., 2005, ApJ, 633, 589

[100] Shanks, T., Boyle, B. J., 1994, MNRAS, 271, 753

[101] Shanks, T., 2007, MNRAS, 376, 173S

[102] Sharp, R.G. et al., 2006, SPIE, 6269E, 14S

[103] Sheth, R. K., Mo, H. J., Tormen, G., 2001, MNRAS, 323, 1

[104] Smith, R. J. Boyle, B. J., Shanks, T., Croom, S. M., Miller, L., Read, M., 1997, IAUS, 179, 348

[105] Spergel, D. N., et al., 2003, ApJS, 148, 175

[106] Spergel, D. N., et al., 2007, ApJS, 170, 377S

[107] Stevenson, P. R. F., Fong R., Shanks T., 1988, MNRAS, 234, 801

[108] Taylor, A. N., Ballinger, W. E., Heavens, A. F., Tadros, H., 2000, 2001, MNRAS, 327, 689T

[109] Tegmark, M., et al., 2006, PhRvD, 74l3507T

[110] Wake, D. A., et al., 2004, ApJL, 610, L85

[111] Weinstein, M. A. et al., 2004, ApJS, 155, 243

[112] Williams, L. L. R., Irwin, M., 1998, MNRAS, 298, 378

[113] Willmer, C. N. A., da Costa, L. N., Pellegrini, P. S., 1998, AJ, 115, 869

[114] Wu, X.P., 1994, A&A, 286, 748-752

[115] Yang, X., Mo, H.J., van den Bosch, F. C., Jing, Y. P., 2005a, MNRAS, 356, 1293

[116] Yang, X., Mo, H.J., van den Bosch, F. C., Jing, Y. P., 2005b, MNRAS, 357, 608

[117] Yang, X., Mo, H.J., van den Bosch, F. C., Jing, Y. P., 2005c, MNRAS, 362, 711

[118] Yang, X., Mo, H.J., van den Bosch, F. C., Weinmann, S. M., Cheng, L., Jing, Y. P., 2005d, MNRAS, 362, 711

[119] Zehavi, I. et al., 2005, ApJ, 630, 1